Jakub L. Nowak

Turbulence properties in coupled and decoupled stratocumulus-topped marine boundary layers

A doctoral dissertation
under the supervision of
Prof. Szymon P. Malinowski

UNIVERSITY
OF WARSAW

Institute of Geophysics
Faculty of Physics
University of Warsaw

Warsaw 2021

Acknowledgements

This work would have never been accomplished without the support I received from a great number of people. First, I would like to express my gratitude to the supervisor, Prof. Szymon Malinowski, for his invaluable advice and guidance provided throughout the period of my doctoral studies. Similarly, I am also deeply grateful to Dr. Holger Siebert who was my supervisor during one year research stay at the Leibniz Institute for Tropospheric Research (TROPOS) in Leipzig.

The research presented in this thesis is based on the unique field data collected within the ACORES experiment. Therefore, I owe thanks to all the scientists and technicians involved in this project. Apart from the leaders, Dr. Holger Siebert and Dr. Birgit Wehner, I would like to mention here those with whom I closely collaborated in instrument development, measurements, data analysis or interpretation: Dr. Wojciech Kumala, Dr. Silvia Henning, Kai Szodry and Janine Lückerath.

I would like to extend my sincere thanks to the colleagues in Warsaw and Leipzig, in particular fellow doctoral students Katarzyna, Justyna, Moein, Emmanuel, Łucja, Dominika, Matthias and Ulrike, for their words of comfort and encouragement in the difficult hours of my work. Moreover, I appreciate Dr. Marta Wacławczyk for her insightful comments on the early draft of the thesis.

My research was pushed forward thanks to the one year grant awarded by the German Academic Exchange Service (DAAD) for my visit to TROPOS. The ACORES experiment received funding from the German Research Foundation (DFG) and Polish National Science Center (NCN).

Most importantly, I am truly grateful to God who kindly offered me both talents and opportunities to undertake research into some aspects of the workings of nature.

Statement of Originality

The thesis I am submitting was composed by myself. The work presented herein is my own except where explicitly stated otherwise. I have clearly indicated the presence of all material I have quoted from other sources, including any diagrams, charts, tables or graphs. I have clearly indicated the presence of all paraphrased material with appropriate references. This work has not been submitted for any other degree or professional qualification before.

The data analyzed in this thesis were collected within the field experiment ACORES carried out by a team of scientists. Their names are covered in the list of authors of Siebert et al. (2021). My involvement in the experiment included: development of the UltraFast Thermometer (UFT) to be mounted on the helicopter-borne platform ACTOS (together with W. Kumala and S. Malinowski), its laboratory tests and preparation for airborne operation (with W. Kumala), participation in training and test flights, participation in the actual measurements in July 2017 – in particular maintaining the UFT.

Following the measurement period, there was a strong collaboration in data postprocessing. My involvement included: postprocessing of the high-rate temperature records, postprocessing of the navigation, wind and turbulence data (with H. Siebert and K. Szodry) – in particular the design and implementation of a simplified wind transformation (see sec. 3.2). Concerning other data utilized in this work, K. Szodry and H. Siebert were responsible for the postprocessing of the humidity, liquid water and reference temperature measurements while S. Henning, B. Wehner and J. Luckerath for the postprocessing of the aerosol measurements.

The analysis and interpretation presented in the thesis are my own work performed with the guidance and advice I have received from S. Malinowski and H. Siebert. Part of this work has been published in a research article: Nowak, J. L., Siebert, H., Szodry, K.-E., and Malinowski, S. P., "Coupled and decoupled stratocumulus-topped boundary layers: turbulence properties" in Atmospheric Chemistry and Physics (Nowak et al., 2021). I played a major role in that research which is reflected in the author contribution statement of the article:

> All the authors participated in the instrument preparation, measurements and data postprocessing within the ACORES project where H.S. was the principal investigator. J.L.N. designed the presented analysis with advice from S.P.M and H.S. The analysis was performed by J.L.N. with contributions from K.E.S. and with guidance of H.S. and S.P.M. J.L.N. wrote the manuscript with contributions from S.P.M. and H.S.

In the thesis, the material presented in that paper is expanded with additional topics and additional details. Because I am the author of the text of the paper, I do not quote this paper explicitly but specify at the beginning of each chapter which sections has been previously included in the paper. Apart from Nowak et al. (2021), all the other sources are explicitly quoted or appropriately referenced.

Abstract

Stratocumulus clouds are ubiquitous around the globe. On average, they cover around 20 % of the Earth's surface. Wide-spread presence, persistence and high albedo makes them important for the energy balance of the planet. Because only minor variations in coverage or optical thickness can impact the surface radiation budget, the feedback of stratocumulus clouds to global warming remains one of the major sources of uncertainty in model-based climate predictions.

Marine stratocumulus clouds typically occupy upper few hundred meters of the atmospheric boundary layer. Circulation and turbulence in such a stratocumulus-topped boundary layer (STBL) is driven primarily by the cloud top radiative cooling which can be supported by evaporative cooling, latent heat release, surface heating and wind shear. The transport of moisture from the ocean surface maintains the cloud against entrainment drying. The efficiency of vertical transport, hence the properties of stratocumulus cloud and its evolution, is dependent on the thermodynamic and dynamic structure of the STBL. When the STBL grows in depth, the drivers of the circulation weaken or the subcloud layer stabilizes, then the mixing of air volumes across the entire STBL depth may become impossible to sustain. The boundary layer decouples, i.e. the stratocumulus cloud is disconnected from the moisture supply from the surface.

Within the present study, the stratification, turbulence and aerosol properties in coupled and decoupled marine STBLs are compared using high resolution in situ measurements performed by the helicopter-borne platform ACTOS in the region of the Eastern North Atlantic. Particular attention is given to small-scale turbulence.

The thermodynamically well-mixed (i.e. coupled) STBL was characterized by a comparable latent heat flux at the surface and in the cloud top region, and substantially smaller sensible heat flux in the entire depth. Turbulence kinetic energy (TKE) was efficiently generated by buoyancy in the cloud and at the surface, and dissipated with comparable rate across the entire depth. Structure functions and power spectra of velocity fluctuations in the inertial range were reasonably consistent with the predictions of Kolmogorov theory. The turbulence was close to isotropic.

In the decoupled STBL, decoupling was most obvious in humidity profiles. Heat fluxes and buoyant TKE production at the surface were similar to the coupled case. Around the transition level, latent heat flux decreased to zero and TKE was consumed by weak static stability. In the cloud top region, heat fluxes almost vanished and buoyancy production was significantly smaller than for the coupled case. TKE dissipation rate inside the decoupled STBL varied between its sublayers. Structure functions and power spectra in the inertial range deviated from Kolmogorov scaling. This was more pronounced in the cloud and subcloud layer in comparison to the surface mixed layer. The turbulence was more anisotropic than in the coupled STBL, with horizontal fluctuations dominating. The degree of anisotropy was largest in the cloud and subcloud layer of the decoupled STBL.

Integral length scales, of the order of 100 m in both cases, indicate turbulent eddies smaller than the depth of the coupled STBL or of the sublayers of the decoupled STBL. It is hypothesized that turbulence produced in the cloud or close to the surface is redistributed across the entire coupled STBL but rather only inside the sublayers where it was generated in the case of the decoupled STBL. Scattered cumulus convection, developed below the stratocumulus base, may play an important role in the transport between those sublayers.

In both cases, the size distribution of aerosol particles did not change significantly with height, except for the influence of activation inside the cloud. Three principal modes were identified in the aerosol size distributions: Aitken, accumulation and larger accumulation. The sources of the observed aerosol particles were likely sea spray emission and long-range transport of continental aerosol combined with the entrainment into the STBL. The total concentration of aerosol particles and the concentration of cloud condensation nuclei were constant below the coupled stratocumulus. In the decoupled STBL, the concentrations in the subcloud layer were smaller than in the surface mixed layer.

Most of the results concerning the coupled case are consistent with the previous studies of stratocumulus dynamics. The observations of TKE production, heat fluxes and turbulent fluctuations in the decoupled STBL fit well into the range of conditions reported in the literature. The important novelty of this work are the results on small-scale turbulence because the parameters like local dissipation rate, intertial range scaling, anisotropy and length scales were not addressed in the context of STBL coupling before.

Streszczenie

Chmury stratocumulus są wszechobecne na całym świecie. Pokrywają średnio około 20 % powierzchni Ziemi. Ich powszechne występowanie, trwałość i wysokie albedo czynią je istotnymi dla bilansu energetycznego całej planety. Ponieważ tylko niewielkie różnice w pokrywie lub grubości optycznej mogą wpływać na bilans radiacyjny powierzchni, odpowiedź tych chmur na globalne ocieplenie pozostaje jednym z głównych źródeł niepewności w prognozach klimatu.

Morskie chmury stratocumulus zwykle zajmują górne kilkaset metrów warstwy granicznej atmosfery. Cyrkulacja i turbulencja w warstwie granicznej zwieńczonej stratocumulusem (WGZS) są napędzane przede wszystkim przez chłodzenie radiacyjne na wierzchołku chmury, które może być dodatkowo wspomagane przez chłodzenie związane z parowaniem kropelek, uwalnianie ciepła utajonego, ogrzewanie przy powierzchni oraz ścinanie wiatru. Transport wilgoci z powierzchni oceanu utrzymuje chmurę, przeciwdziałając jej wyparowaniu pod wpływem wciągania suchego powietrza sponad warstwy granicznej. Wydajność transportu pionowego, a więc również właściwości chmury stratocumulus i jej ewolucja, zależy od termodynamicznej i dynamicznej struktury WGZS. Gdy WGZS rośnie, cyrkulacja słabnie lub warstwa podchmurowa ulega stabilizacji, wówczas mieszanie powietrza w całej głębokości WGZS może stać się niemożliwe do utrzymania. Warstwa graniczna ulega rozsprzężeniu, tzn. chmura stratocumulus zostaje odłączona od dopływu wilgoci z powierzchni.

W ramach niniejszej pracy porównano właściwości stratyfikacji, turbulencji i aerozoli pomiędzy sprzężoną a rozsprzężoną morską WGZS, wykorzystując w tym celu pomiary in situ o wysokiej rozdzielczości wykonane w rejonie północno-wchodniego Atlantyku przy pomocy platformy ACTOS na śmigłowcu. Szczególną uwagę zwrócono na własności drobnoskalowej turbulencji.

Dobrze wymieszana sprzężona WGZS charakteryzowała się porównywalnym strumieniem ciepła utajonego na powierzchni i w górnej części chmury oraz znacznie mniejszym strumieniem ciepła jawnego w całej głębokości. Energia kinetyczna turbulencji (EKT) była wydajnie generowana dzięki efektom wypornościowym w chmu-

rze i na powierzchni, natomiast dyssypowana w porównywalnym stopniu w całej głębokości. Funkcje struktury i widma mocy dla fluktuacji prędkości były w zakresie inercyjnym zgodne z przewidywaniami teorii Kołmogorowa. Turbulencja była bliska izotropii.

W rozsprzężonej WGZS jej rozsprzężenie było najbardziej widoczne w profilach wilgotności. Na powierzchni, strumienie ciepła i produkcja EKT przez wypór były podobne do przypadku sprzężonego. W okolicach warstwy przejściowej, strumień ciepła utajonego spadał do zera, a EKT była pochłaniana z uwagi na stabilność. W rejonie wierzchołka chmury strumienie ciepła niemal zanikały, a produkcja EKT przez wypór była znacznie mniejsza w porównaniu do przypadku sprzężonego. Tempo dyssypacji EKT wewnątrz rozsprzężonej WGZS różniło się pomiędzy jej podwarstwami. Funkcje struktury i widma mocy odbiegały w zakresie inercyjnym od skalowania przewidywanego przez teorię Kołmogorowa. Ten fakt był bardziej widoczny wewnątrz chmury i w warstwie podchmurowej w porównaniu z warstwą powierzchniową. Turbulencja była bardziej anizotropowa niż w sprzężonej WGZS, z dominującymi fluktuacjami w kierunku poziomym. Stopień anizotropii był największy w warstwie chmurowej i podchmurowej.

Skale całkowe rzędu 100 m w obu przypadkach wskazują, że wiry turbulencyjne są mniejsze niż głębokość sprzężonej WGZS czy też głębokość podwarstw rozsprzężonej WGZS. Postawiono hipotezę, że turbulencja wytworzona w chmurze lub w pobliżu powierzchni jest rozprowadzana w całej sprzężonej WGZS, natomiast w przypadku rozsprzężonej WGZS tylko wewnątrz podwarstwy, w której została wygenerowana. Istotną rolę w transporcie między tymi podwarstwami mogą odgrywać chmury cumulus, tworzące się poniżej podstawy stratocumulusa.

W obu przypadkach rozkład wielkości cząsteczek aerozolu nie zmieniał się znacząco z wysokością, z wyjątkiem wpływu aktywacji wewnątrz chmur. Zidentyfikowano trzy główne mody: Aitkena, akumulacyjny i akumulacyjny większy. Źródłami obserwowanych aerozoli była prawdopodobnie emisja z powierzchni oceanu oraz transport aerozolu kontynentalnego połączony z wciąganiem powietrza do warstwy granicznej. Całkowite stężenie cząsteczek aerozolu i stężenie jąder kondensacji były stałe poniżej sprzężonego stratocumulusa. W rozsprzężonej WGZS stężenia w warstwie podchmurowej były mniejsze niż w warstwie powierzchniowej.

Większość wyników dotyczących przypadku sprzężonego jest zgodna z wcześniejszymi badaniami dynamiki chmur stratocumulus. Pomiary produkcji EKT, strumieni ciepła i fluktuacji turbulencyjnych w rozsprzężonej WGZS mieszczą się w

szerokim spektrum możliwych warunków opisywanych w literaturze. Istotną nowością tej pracy są wyniki dotyczące drobnoskalowej turbulencji, ponieważ parametry takie jak lokalne tempo dyssypacji EKT, skalowanie zakresu inercyjnego, anizotropia i skale długości nie były wcześniej badane w kontekście stopnia sprzężenia WGZS.

Contents

Chapter 1

Introduction

In the introduction, I discuss the definition, occurrence and importance of stratocumulus clouds. The structure and main physical processes operating in a stratocumulus-topped boundary layer (STBL) are described with a focus on turbulence. The phenomenon of STBL decoupling is explained, followed by the discussion of the mechanisms leading to decoupling as well as its consequences for the evolution of the STBL. Next, I review the previous studies concerning turbulence properties in decoupled STBLs. Finally, the area of the measurements analyzed in this study – the Eastern North Atlantic (ENA) – is introduced with respect to typical cloud and boundary layer properties.

It is assumed that the reader is familiar with the basic knowledge in the fields of turbulence, atmospheric boundary layer and atmospheric thermodynamics. These topics are extensively covered in a number of classical textbooks, e.g. Stull (1988); Pope (2000); Markowski and Richardson (2010). The content of this chapter is based on the range of research articles treating specifically about stratocumulus clouds and STBLs.

1.1 Stratocumulus clouds

1.1.1 Characteristics

According to the traditional classification, stratocumulus is a genus of clouds occurring in the low levels of the atmosphere. The name, originating from Latin, refers to its appearance, with *stratus* meaning "cover, spreading" and *cumulus* meaning "heap, pile, accumulation". World Meteorological Organization (WMO) defines stratocumulus in its International Cloud Atlas (World Meteorological Organization):

> Grey or whitish, or both grey and whitish, patch, sheet or layer of cloud that almost always has dark parts, composed of tessellations, rounded masses, rolls, etc., which are non-fibrous (except for virga) and which may or may not be merged; most of the regularly arranged small elements have an apparent width of more than 5°.

Within the cloud observation coding, stratocumulus genus corresponds to the labels C_L4, C_L5 and C_L8, depending on the origin and additional features. In this work, two configurations involving the mature developed stratocumuli are primarily considered: stratocumulus non-cumulogenitus (C_L5) and stratocumulus together with cumulus where the base of stratocumulus is located at a different height than the base of cumulus (C_L8). Those clouds are illustrated in the sketches given in the WMO cloud atlas (Fig. 1.1).

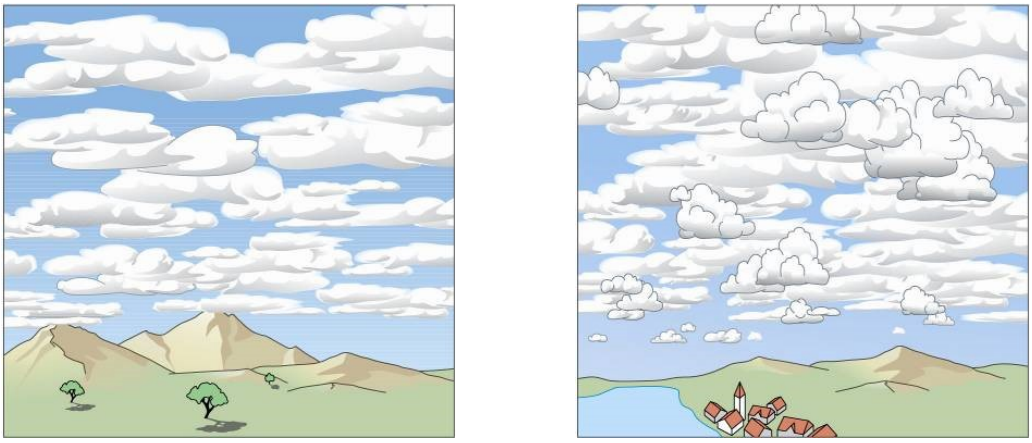

(i) C_L5: Stratocumulus non-cumulogenitus (ii) C_L8: Cumulus and Stratocumulus

Figure 1.1: Sketch illustrations for the cloud observation codes involving stratocumulus. From International Cloud Atlas (World Meteorological Organization).

The layered form of stratocumulus clouds is often maintained thanks to a capping temperature inversion providing strong static stability. Although horizontally flat from large-scale perspective, their upper surface often exhibits quite a complex structure when smaller scales, below ∼100 m, are considered (see photograph in Fig. 1.2). The characteristic feature, discerning stratocumulus from other stratiform cloud genera, is their dynamics driven to a large extent by the convective instability resulting from cloud-top radiative and evaporative cooling.

Figure 1.2: Photograph of a typical stratocumulus cloud over the ENA taken from the helicopter during one of the flights of the ACORES field campaign. Mount Pico is visible on the right side.

1.1.2 Relevance

Low-level stratocumulus clouds cover around 20 % of the Earth's surface in annual mean, more than any other cloud type (Wood, 2012). Incoming solar radiation is mostly reflected at the cloud top while the effect of a cloud on outgoing longwave radiation is minor comparing to a cloud-free situation. Thus, the strong negative net radiative forcing contributes to the cooling of the underlying atmosphere and surface.

Wide-spread presence, persistence and high albedo make marine stratocumulus important for the energy balance of the planet (Hartmann et al., 1992). Minor variations in coverage and optical thickness impact the radiation budget, therefore low-level cloud feedbacks remain the major sources of uncertainty in model-based climate predictions (Boucher et al., 2013; Schneider et al., 2019). Only relatively small differences in their coverage, albedo or thickness can potentially offset or strongly amplify the anthropogenic global warming caused by the increased concentration of greenhouse gases.

1.1.3 Climatology

The occurrence of stratocumulus clouds around the globe is strongly linked to the general circulation of the atmosphere. Typically, they occupy the upper few hun-

dred meters of the atmospheric boundary layer in the conditions of large-scale subsidence, strong lower-tropospheric stability and moisture supply from the surface (Wood, 2012). Such conditions are usually present in the subsiding parts of the Hadley circulation, in particular over the subtropical oceans with upwelling of cold deep water (Fig. 1.3). Over the subtropical eastern oceans, the stratocumulus annual mean cover can reach even more than 60 %. The so-called semi-permanent subtropical marine stratocumulus sheets feature the pattern which is roughly latitudinally symmetric about the tropical convergence zone, although in the Southern Hemisphere those sheets tend to be a bit larger.

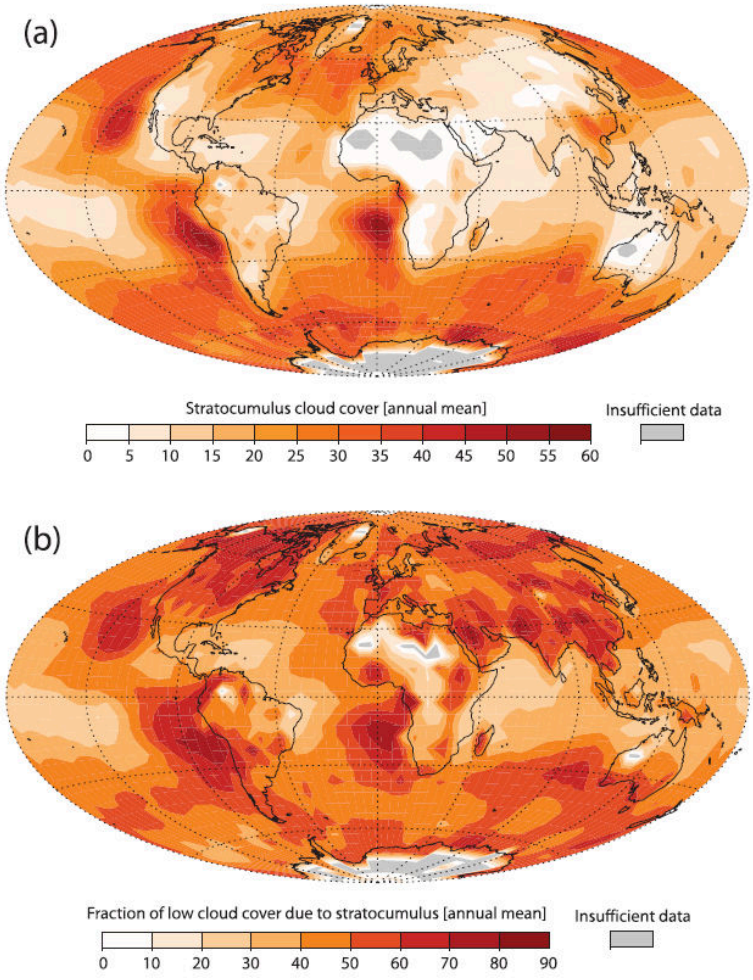

Figure 1.3: Climatology of stratocumulus clouds: (a) annual mean coverage, (b) fraction of annual mean low-cloud cover due to stratocumulus. From Wood (2012).

Other typical locations of frequent stratocumulus formation include midlatitude oceans, in particular in the post-cold-frontal air masses related to midlatitude baro-

clinic systems. Moreover, stratocumulus often occurs in polar regions and in cold-air outbreaks over the oceans (Fig. 1.4). Broadly speaking, stratocumulus clouds are climatologically important over the vast majority of the Earth's surface. Even in the places where they seem to be relatively scarce, they contribute significantly to the total low cloud cover.

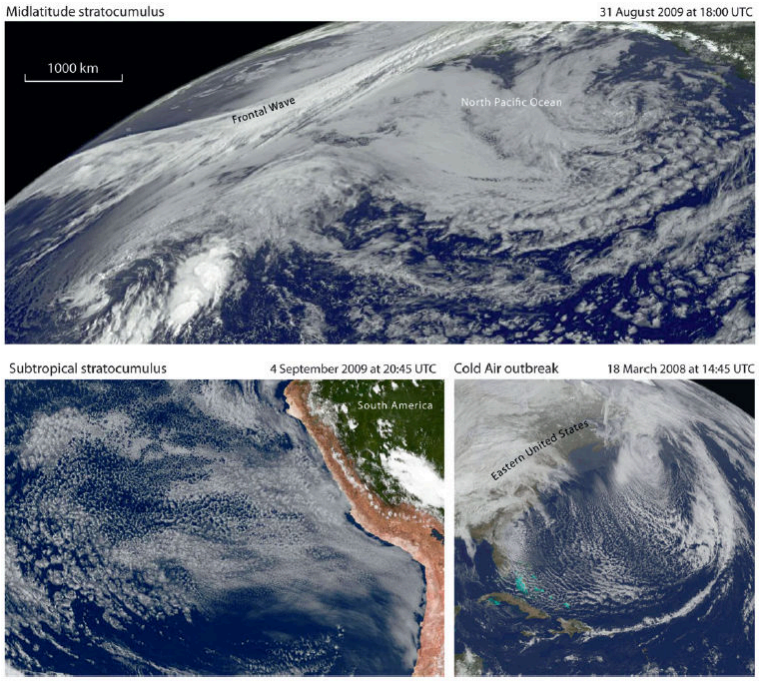

Figure 1.4: Satellite imagery from the Geostationary Operational Environmental Satellites (GOES) showing stratocumulus clouds in midlatitudes, subtropics, and associated with a cold-air outbreak. From Wood (2012).

1.2 Stratocumulus-topped boundary layer

1.2.1 Main driving processes

The primary mechanism driving the circulation inside an STBL is longwave radiative cooling at the cloud top which produces convective instability. An additional source of turbulence is provided by buoyancy due to surface heat fluxes, wind shear, latent heat release in updrafts, evaporation in downdrafts and evaporative cooling associated with the entrainment of dry, warm air from the free troposphere (FT) (Lilly, 1968; Stevens, 2002; Gerber et al., 2016; Mellado, 2017).

Circulation and turbulence facilitate horizontally homogeneous cloud structure and maintain the cloud by connecting the cloud layer with the surface source of moisture. Turbulence also contributes to maintain or enhance the temperature inversion right above the cloud top where the gradient can reach 10-20 K over the vertical distance of a few meters only. The key processes important for the STBL state and evolution are shown schematically in the sketch (Fig. 1.5) from Wood (2012).

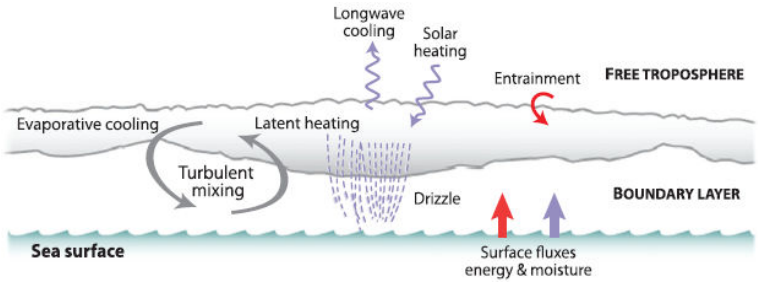

Figure 1.5: Schematic of the key processes in an STBL. From Wood (2012).

1.2.2 Stratification

The properties of an STBL are dependent on the level in which the stratocumulus is coupled with the sea surface fluxes, in particular of latent and sensible heat (Bretherton et al., 1995; Bretherton and Wyant, 1997; Ghate et al., 2015; Zheng et al., 2018b). Moderately shallow STBLs (about 500-1000 m) are often well mixed (Stull, 1988; Markowski and Richardson, 2010; Wood, 2012) and exhibit the largest fractional cloud coverage. Their typical vertical structure features: temperature T decreasing with dry adiabatic lapse rate Γ_d below the cloud and moist adiabatic Γ_m inside the cloud, strong capping temperature inversion at the top, near-constant concentration of moist-conserved variables such as total water mass fraction $q_t = q_v + q_l$ (where q_v denotes specific humidity and q_l liquid water mass fraction) and liquid water potential temperature θ_l from the surface up to the inversion base.

In addition, the well-mixed character of an STBL is indicated by the lifting condensation level (LCL) consistent with the cloud base height (CB). Horizontal winds u_e, v_e (eastward and northward) are generally nearly constant with height z, except for close to the surface, but there is often strong wind shear across the inversion manifested in the gradient of wind magnitude U or wind direction dd. The example vertical profiles in well-mixed STBLs are given in Fig. 1.6 and Fig. 1.7.

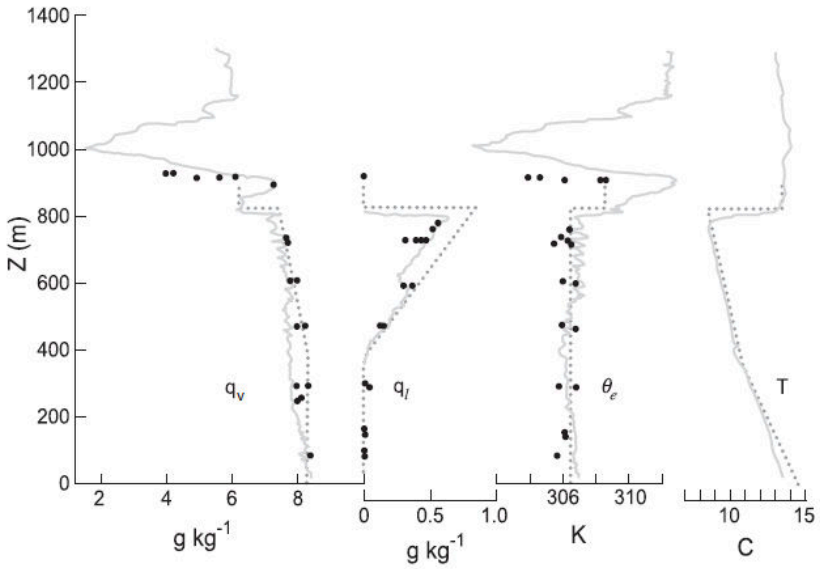

Figure 1.6: Vertical profiles of water vapor q_v and liquid water q_l mass fractions, equivalent potential temperature θ_e and temperature T for a summertime shallow and quite well-mixed STBL observed over the North Sea. Dots denote mean values from horizontal legs. Dotted lines show the profiles expected for a well-mixed layer. From Wood (2012) who adapted from Nicholls (1984).

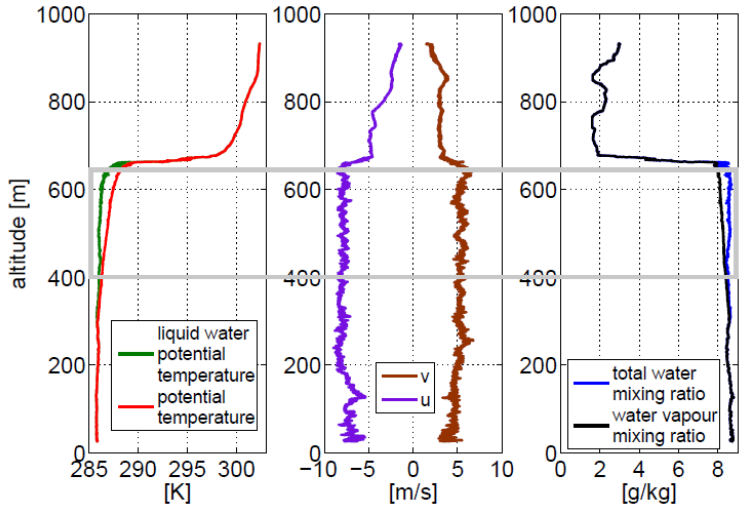

Figure 1.7: Vertical profiles of liquid water potential temperature, potential temperature, eastward u and northward v horizontal wind components, total water and water vapor mixing ratios for a shallow and quite well-mixed STBL observed over the northeastern Pacific in the research flight TO10 of the Physics of the Stratocumulus Top (POST) field campaign. From Malinowski et al. (2013), their original notation.

A particularly important part of an STBL is the cloud top region where the entrainment and mixing of warm dry air from the FT occurs. The range of heights between the cloud top and the upper limit of the influence of mixing from the boundary layer is described as the entrainment interface layer (EIL). Entrainment and mixing affect the whole cloud structure and are crucial for the STBL evolution. The structure of the EIL and the properties of the entrainment process have been investigated in many observational studies (Lenschow et al., 2000; Faloona et al., 2005; Gerber et al., 2005; Haman et al., 2007; Katzwinkel et al., 2012; Carman et al., 2012; Malinowski et al., 2013; Gerber et al., 2013; Jen-La Plante et al., 2016) as well as numerical simulations (Stevens, 2002; Moeng et al., 2005; Yamaguchi and Randall, 2008; Kurowski et al., 2009; de Lozar and Mellado, 2015, 2017; Mellado, 2017). Therefore, these topics are not in the focus of the present work which addresses rather the structure of an STBL below the cloud top region.

1.2.3 Turbulence

The state of an STBL is profoundly influenced by the turbulence operating inside. The amount of energy contained in turbulent motions affects the entrainment of the air from the FT and the intensity of mixing inside the boundary layer. On the other hand, turbulent fluxes of heat, moisture, momentum and other constituents define the mean properties and the evolution of a stratocumulus cloud. The intensity of turbulence is regulated by different mechanisms producing, consuming or dissipating turbulence kinetic energy (TKE).

Essential for the analysis of turbulence is the decomposition of any variable:

$$x(t) = \langle x(t) \rangle + x'(t) \tag{1.1}$$

into a large-scale slowly varying mean $\langle x(t) \rangle$ and small scale turbulent fluctuations $x'(t)$ in the procedure called Reynolds averaging or Reynolds decomposition (e.g. Stull, 1988).

1.2.3.1 TKE and turbulent variances

Turbulence kinetic energy is generated primarily by cloud top cooling (radiative or evaporative), surface warming, latent heat release and wind shear (Malinowski et al., 2013; Gerber et al., 2016; Kopec et al., 2016), where the exact contributions of those effects depend on specific conditions (see sec. 1.2.3.3). Because the efficient

operation of such processes is typically confined to specific locations (e.g. cloud top or surface layer), the intensity of turbulent fluctuations of wind velocity, temperature or humidity may vary with height.

The variance of vertical wind fluctuations $\langle w'^2 \rangle$ usually maximizes away from the top and bottom STBL boundaries, but predominantly in its upper portion where positive buoyancy is induced by latent heat release. For example, this is visible in the measurements and simulations of the first research flight (RF01) of the second Dynamics and Chemistry of Marine Stratocumulus (DYCOMS-II) field study (Fig. 1.8). The maximum of $\langle w'^2 \rangle$ indicates the level where updrafts and downdrafts are the strongest. Typically, the downdrafts originating at the cloud top are stronger and smaller in area than the updrafts because cloud top cooling is the dominant driver of convection in STBLs. However, the opposite effect can be observed close to the surface when surface heat flux is significant or in cumulus-coupled STBLs (see sec. 1.3). The relative strength of those updrafts and downdrafts is manifested by the sign of the third moment of vertical velocity fluctuations $\langle w'^3 \rangle$ (Fig. 1.8). In general, the motions in an STBL are stronger at night when the net radiative driving at the cloud top is stronger.

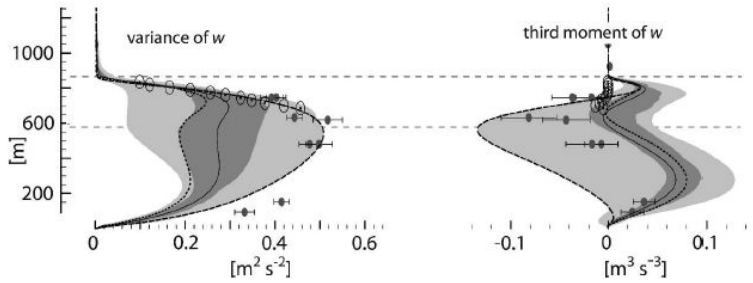

Figure 1.8: Vertical profiles of vertical velocity variance (left) and third moment (right) for the DYCOMS-II RF01. Markers indicate estimates as derived from the in situ (solid dot with bar) and radar (circle-dot) observations. The in situ data shows the mean and standard deviations about the mean for 2.5 min (15 km) sub-legs of 30 min legs. The light shading spans the distribution of the results for different models and is delimited by the maximum and minimum value within the ensemble. The dark shading denotes the central half of the distribution as delimited by the first and third quartile. The solid line is the ensemble mean. The dashed lines are two selected models from the ensemble. Horizontal dashed lines delimit the cloud area. From Stevens et al. (2005).

In a well-mixed STBL or well-mixed sublayers of a decoupled STBL, it was found that the profile of $\langle w'^2 \rangle$ often follows convective scaling, i.e. it can be non-dimensionalized to obtain a universal function with the use of the reference convective velocity scale w_*. This scale is defined as the integral of the buoyancy flux (e.g. Wood, 2012, Eq. (4)):

$$w_*^3 = 2.5 \int_0^h \frac{g}{\theta_v} \langle w' \theta_v' \rangle dz, \tag{1.2}$$

where h is the layer depth, g is gravitational acceleration, θ_v is virtual potential temperature. Typical values of w_* in STBLs are 0.25-1.25 $\mathrm{m\,s^{-1}}$ (e.g Nicholls and Leighton, 1986; De Roode and Duynkerke, 1997; Faloona et al., 2005). Certain studies reported that the form of this universal function can be the same as found for dry convective boundary layers (Lenschow et al., 1980) when taken upside-down because the primary source of convection is located at the top instead of the bottom of the boundary layer (Nicholls and Leighton, 1986; Duynkerke et al., 1995; Tjernström and Rogers, 1996; De Roode and Duynkerke, 1997). Although the location of the maximum $\langle w'^2 \rangle$ is predicted well by the similarity curve, Nicholls and Leighton (1986) as well as De Roode and Duynkerke (1997) pointed out that the exact value is rather underestimated. Those authors discussed that such an effect can be related to the small density difference across the inversion which allows for the deformation of the interface in response to local vertical motions. This stays in contrast to the rigid lid boundary at the surface in the case of a dry convective boundary layer. Fig. 1.9 shows an example of the profiles of $\langle w'^2 \rangle$ measured in different research flights which collapse to a single curve when normalized by w_*^2.

In contrast to the vertical, turbulent eddies are not limited in the horizontal direction by the depth of the boundary layer. Usually, the variance of horizontal longitudinal wind fluctuations $\langle u'^2 \rangle$ features local maxima close to the cloud top and close to the surface (e.g. Duynkerke et al., 1995, Fig. 14a). At those locations, turbulent eddies diverge in the horizontal direction and there might be significant wind shear. Due to the absence of clear geometrical constraints and the diversity in wind shear magnitude, no universal scaling of $\langle u'^2 \rangle$ was found in STBLs.

As the consequence of the usual form of the profiles of $\langle u'^2 \rangle$ and $\langle w'^2 \rangle$, TKE stays relatively constant throughout the height, with the local maxima close to the cloud top and the surface (Stevens et al., 2005; Kopec et al., 2016). The example of a TKE profile from the latter publication is given in Fig. 1.10.

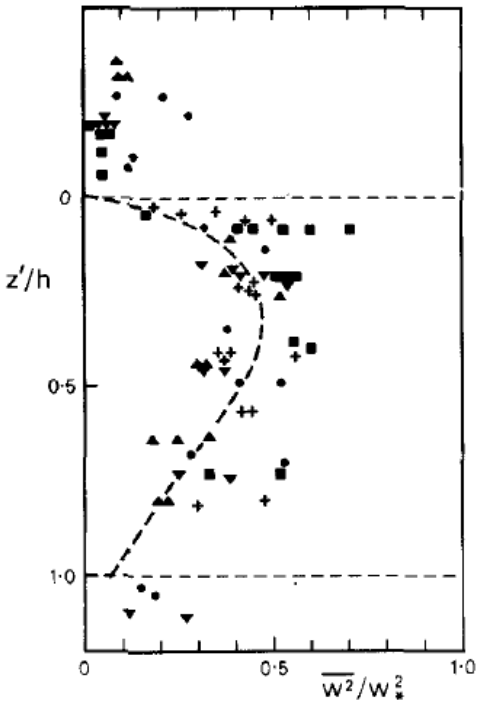

Figure 1.9: Scaled vertical velocity variance in a stratocumulus layer. Different symbols denote different measurement flights. The dashed line is the universal function from Lenschow et al. (1980). From Nicholls and Leighton (1986).

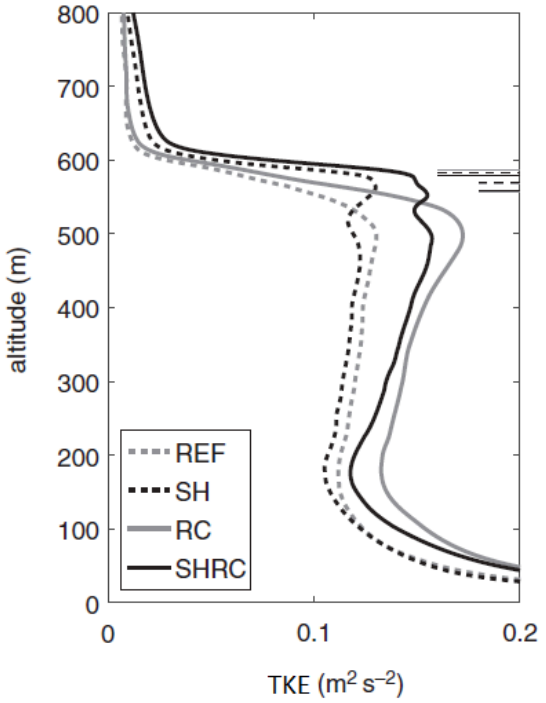

Figure 1.10: Turbulence kinetic energy (TKE) from the simulations of the POST TO13: black lines – with shear, grey – without shear, dashed – without radiative cooling, solid – with radiative cooling. From Kopec et al. (2016).

1.2.3.2 Turbulent fluxes

Turbulent fluxes are crucial to facilitate the vertical transport across an STBL as well as to maintain a stratocumulus cloud or drive its evolution. The vertical transport, in particular of heat and moisture, is closely related to the degree of dynamic coupling.

In general, vertical flux is required to be a linear function of height if a layer is supposed to remain well-mixed (e.g. Stull, 1988). Total heat flux is customarily partitioned into sensible heat flux Q_s related to the differences in temperature of air volumes and latent heat flux Q_l related to the differences in moisture content which can be converted into heat in the process of condensation:

$$Q_s = \rho c_p \langle w'\theta' \rangle , \qquad Q_l = \rho L_v \langle w' q_v' \rangle \tag{1.3}$$

where ρ is air density, θ potential temperature, L_v latent heat of vaporization for water and c_p specific heat of dry air at constant pressure.

Q_s and Q_l evaluated at the surface quantify the transfer of heat and moisture, respectively, between the ocean and the atmosphere. In marine boundary layers, Q_l is typically much larger than Q_s. For instance, Ghate et al. (2015) reported the mean surface sensible heat flux of 9.4 and 7.9 $\mathrm{W\,m^{-2}}$ while the mean surface latent heat flux of 103 and 72 $\mathrm{W\,m^{-2}}$ for the two measurement stations located in the southeastern Pacific and northeastern Atlantic, respectively (c.f. sec. 1.4.3).

Q_l is proportional to the vertical flux of water vapor $\langle w'q_v' \rangle$. Specific humidity is not itself a conserved quantity due to possible phase transitions. Instead, conserved in moist processes is q_t which includes the contribution of q_l. Total water flux $\langle w'q_t' \rangle$ can either decrease or increase with height because the water sink due to entrainment can be comparable to the water source due to surface evaporation. The flux can be partitioned into several terms:

$$\langle w'q_t' \rangle = \langle w'q_v' \rangle + \langle w'q_l' \rangle + \widetilde{w_T q_l}. \tag{1.4}$$

The turbulent flux of liquid water $\langle w'q_l' \rangle$ can contribute significantly in the cloud (Nicholls, 1984; Duynkerke et al., 1995). Gravitational settling of rain and cloud droplets is denoted by $\widetilde{w_T q_l}$ where w_T stands for the settling velocity dependent on size and tilde refers to the average across the same area as for turbulent fluxes which is however not exactly a Reynolds average in its usual sense (c.f. Nicholls, 1984). In a thick stratocumulus, precipitation and cloud droplet sedimentation can reach the magnitude comparable with other terms (Nicholls, 1984; Duynkerke et al., 1995; De Roode and Duynkerke, 1997). Measuring all the terms of the above water budget simultaneously poses a challenge for experimental projects. Moreover, most of the vertical transport of moisture is realized by the eddies of large horizontal scales which require a very long measurement path to ensure an acceptable sampling error (Lenschow and Stankov, 1986; Lenschow et al., 1994).

1.2.3.3 TKE budget

The intensity of turbulence and its temporal evolution in an atmospheric boundary layer under the assumption of horizontal homogeneity can be well described by the TKE budget equation (e.g. Stull, 1988, Eq. 5.1b):

$$\frac{\partial}{\partial t}TKE = \underbrace{\frac{g}{\langle \theta_v \rangle}\langle w'\theta_v' \rangle}_{B} \underbrace{-\langle u'w' \rangle \frac{\partial \langle u \rangle}{\partial z} - \langle v'w' \rangle \frac{\partial \langle v \rangle}{\partial z}}_{S} \underbrace{-\frac{\partial \langle w' \mathrm{TKE} \rangle}{\partial z}}_{Tr} \underbrace{-\frac{1}{\langle \rho \rangle}\frac{\partial \langle w'P' \rangle}{\partial z}}_{Pr} - \epsilon \tag{1.5}$$

where B is buoyancy production/consumption, S is shear production, Tr is turbulent transport, Pr is pressure correlation term, ϵ is TKE dissipation rate, P is pressure and v is lateral wind velocity.

In a typical STBL, the dominant terms which provide a crude approximate balance are B, ϵ and Tr. The strength of shear production depends on the mean wind profile. S can be significant if there is a considerable wind gradient across the cloud top and capping inversion. Otherwise, S is limited to surface friction and local shear induced by the plumes diverging below the stable interface at the top. Such a case of a shallow well-mixed nocturnal STBL with rather restrained wind shear is represented by the observations of the DYCOMS-II RF01. Those conditions were simulated by Mellado et al. (2018). Fig. 1.11 presents the profiles of the leading terms in the TKE budget equation from their simulations.

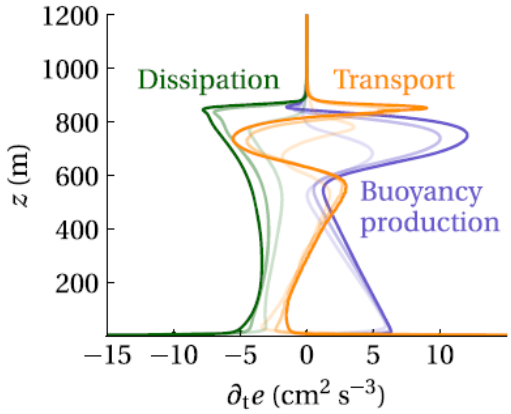

Figure 1.11: Leading terms of the TKE budget in the simulations of the DYCOMS-II RF01. Darker colors indicate higher Reynolds number of the simulation. From Mellado et al. (2018).

Usually, buoyancy is the primary source of turbulence inside an STBL. B is maximum in the cloud layer (Nicholls and Leighton, 1986; Duynkerke et al., 1995). Significant buoyancy is induced particularly by the radiative or evaporative cooling at the cloud top (Gerber et al., 2016) and further enhanced by the in-cloud latent heat release (Lilly, 1968; Moeng et al., 1992; Bretherton and Wyant, 1997). The exact position of B maximum results from the vertical distribution of longwave cooling and the proportions between the strength of cloud top cooling and latent warming (Duynkerke et al., 1995; Dodson and Small Griswold, 2021). Often, there is an abrupt increase in B above the cloud base. Moreover, B can be also significant close to the surface from where convective plumes might originate, depending on the

surface temperature and heat fluxes. B is frequently slightly negative right below the cloud base which indicates TKE consumption. Under such conditions, TKE needs to be transported to this place so that the STBL remains well-mixed. If not compensated by efficient transport (see positive Tr at this location in Fig. 1.11), the strong negative buoyancy can lead to boundary layer decoupling (Turton and Nicholls, 1987; Bretherton and Wyant, 1997; Stevens, 2000).

Buoyancy in a marine STBL is strongly related to moisture transport and distribution. For instance, under the condition of the same potential temperature, the air volumes from the surface, which are humid thanks to evaporation (related to latent heat flux), can be more buoyant than the air volumes from the cloud top, which are dried due to the mixing with the FT and precipitation. The difference in buoyancy becomes even stronger if one considers diabatic effects, such as radiative and evaporative cooling at the cloud top, latent heating in the cloud or convective heating at the surface (related to sensible heat flux). The differences in buoyancy drive the circulation which mixes the boundary layer.

Turbulent transport mostly acts to remove a portion of the TKE from the locations where it is efficiently produced (e.g. in the cloud, at the surface) and supply it to the locations of consumption or limited production (Fig. 1.11). Mean dissipation rate is typically of similar order across the STBL with local maxima at the surface and at the cloud top.

The magnitudes of the relevant contributions to the TKE budget were analyzed by Kopec et al. (2016) who simulated the STBL as observed in the POST flight TO13. This case is not considered a "classical" STBL, in particular with respect to thermodynamic stratification. Namely, the FT was relatively humid and the gradient of q_t across the cloud top was relatively weak. This prevents buoyancy reversal which occurs when the mixtures of cloudy and free-tropospheric air can become negatively buoyant due to evaporative cooling. Their TKE budget analysis (Fig. 1.12) highlighted the role of wind shear and cloud top radiative cooling for turbulence generation. As expected, B was significant close to the surface and the cloud base. However, the region of efficient production did not span throughout the whole cloud. On the other hand, shear contributed substantially to the TKE production at the cloud top and at the surface. Tr reduced the TKE in the bottom half of the STBL and supplied the TKE in the middle of the cloud. Pr was smaller in relation to the other terms analyzed.

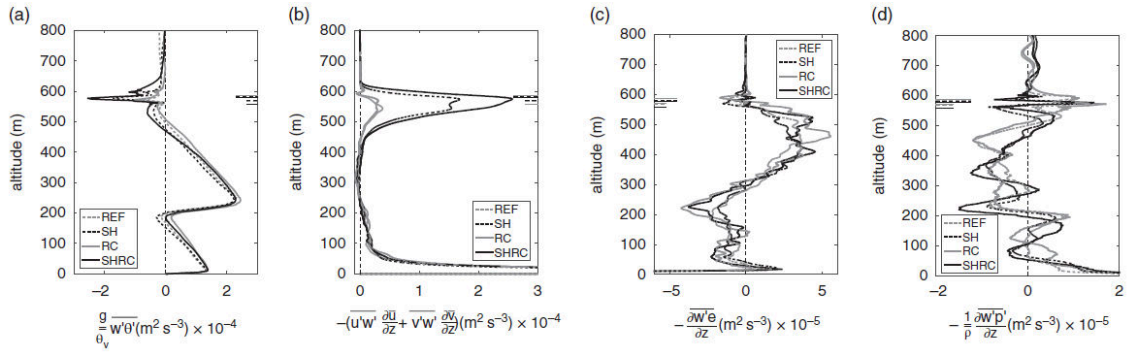

Figure 1.12: TKE budget analysis for the simulations of the POST flight TO13: (a) buoyancy production/consumption, (b) shear production (c) turbulent transport, (d) pressure correlation. Line styles denote different model runs as in Fig. 1.10. From Kopec et al. (2016), their original notation.

1.2.4 Aerosols

The spatial distribution of aerosol particles is dependent on the general stratification of the atmosphere. On the other hand, the microphysical and optical properties of stratocumulus are influenced by the particle number concentration N_p, particle number size distribution (PNSD) and particle composition because they serve as cloud condensation nuclei (CCN). Under some circumstances, clouds additionally play an important role in the process of new particle formation (Wehner et al., 2010, 2015; Williamson et al., 2019) which might, in turn, modify CCN concentration N_{CCN} and consequently cloud droplet number concentration N_d.

Over remote oceans, where stratocumulus clouds habitually reside (see sec. 1.1.3), anthropogenic emissions of aerosols are quite limited. Therefore, particle generation at the ocean surface, long-range transport and new particle formation are significant factors that determine the chemical composition, morphology and vertical distribution of boundary layer aerosols (China et al., 2015; Dzepina et al., 2015; Schum et al., 2018; Zheng et al., 2018a; Wang et al., 2020; Zheng et al., 2020a). The properties and distribution of aerosol particles are closely related to the structure of the marine boundary layer, either cloudy or cloudless, and the history of its evolution – for instance the degree of dynamic coupling between multiple levels (see also sec. 1.3.5).

1.3 STBL decoupling

1.3.1 Mechanism

From the point of view of density, the STBL stratification is constantly destabilized by buoyancy generation or consumption (cloud top radiative cooling, latent heat release, surface buoyancy flux) which are localized at specific levels. In order to maintain the well-mixed state, the circulation and turbulence need to redistribute the buoyancy so that density changes at the same rate everywhere. This often involves negative B in the subcloud layer (c.f. sec. 1.2.3.3). However, B cannot take whichever value due to the constraints imposed by the TKE budget. When the required B turns too negative, the well-mixed regime cannot be sustained.

For example, when an STBL grows in depth above ∼1 km through the entrainment from the FT, the longwave cooling at the cloud top might become too weak to generate the circulation capable of mixing the positively buoyant volumes across the full STBL depth. The circulation ceases to sustain the mixing and the STBL becomes decoupled, i.e. the cloud is disconnected from the moisture supply from the surface. Then, the STBL separates into sublayers which can become dynamically independent and vary in mean thermodynamic properties.

The decoupled state can be achieved due to the operation of various physical mechanisms. They can be conceptually categorized into the following order:

- reducing the intensity of radiatively driven circulation in relation to the boundary layer depth
  - *deepening-warming*: the entrainment of warm and dry free-tropospheric air which abruptly deepens the STBL (Bretherton and Wyant, 1997),
  - *diurnal insolation*: the absorption of solar radiation which heats the cloud layer and partially offsets the effect of longwave cooling during daytime (Nicholls, 1984; Turton and Nicholls, 1987; Caldwell et al., 2005),
- stabilizing the subcloud layer by low-level cooling
  - *warm air advection*: the transit of the STBL onto colder waters (Stevens et al., 1998; Zheng and Li, 2019; Zheng et al., 2020b),
  - *precipitation evaporation*: the consumption of latent heat which results in the cooling of the subcloud layer (Caldwell et al., 2005; Dodson and Small Griswold, 2021).

1.3.1.1 Deepening-warming

The explanation of this mechanism was provided by Bretherton and Wyant (1997). It is relevant for STBLs over eastern subtropical oceans being advected by the trade winds towards the equator over progressively warmer waters. As the sea surface temperature (SST) rises, the convection intensifies due to the increasing buoyancy flux which, in turn, enhances the entrainment of warm and dry free-tropospheric air into the boundary layer. Simultaneously, the surface relative humidity decreases and the surface latent heat flux increases. The LCLs corresponding to updrafts and downdrafts separate. The stratocumulus cloud layer (SCL) becomes drier than the surface mixed layer (SML).

As the separation of the LCLs continues, updrafts give rise to small cumulus clouds. The cumulus convection penetrates the SCL and further enhances the entrainment which facilitates a positive feedback loop. The STBL rapidly deepens while the diabatic cooling at the cloud top stays nearly constant. In terms of the cloud layer energy balance, the equilibrium between the diabatic cooling and the entrainment warming is broken by the increased entrainment. At some point, radiative driving is not sufficient to maintain the well-mixed state for the entire depth. The sublayers of the STBL are then only intermittently coupled by the penetrative cumulus convection.

Strong Q_l forces the buoyancy flux in the cloud to be much larger than in the subcloud layer. Although vertically averaged B changes only slightly in time, in-cloud B increases but sub-cloud B becomes increasingly negative (c.f. sec. 1.3.4.3). Assuming an STBL with any negative buoyancy flux below the cloud base can be considered decoupled, Bretherton and Wyant (1997) developed a "minimal decoupling criterion". They found the process of deepening-warming is driven primarily by the increasing fraction of surface Q_l to the radiative flux divergence across the STBL (flux ratio). In order to satisfy the criterion, the flux ratio needs to exceed the threshold which is proportional to the fraction of the STBL filled by the cloud and to the entrainment efficiency. For typical subtropical STBLs, it implies $Q_l >$ 50-100 W m^{-2}, depending on specific conditions. Other factors, such as drizzle evaporation, solar insolation or sensible heat flux, do contribute to the process but with less importance.

1.3.1.2 Diurnal insolation

Marine STBLs are often subject to a strong diurnal cycle driven primarily by the changes of solar insolation and its absorption in the upper portion of a stratocumulus cloud. In contrast to clouds originating from convective plumes rising from a heated surface, marine stratocumuli exhibit maximum sky coverage, cloud thickness and liquid water path (LWP) in the early morning instead of the afternoon. Shortwave warming partially offsets longwave cooling, therefore suppresses convective circulation during the day. For relatively deep boundary layers (above ∼1 km), it is quite common to experience reversible daytime decoupling (Turton and Nicholls, 1987). Due to the absorption of solar radiation at the cloud top, the effect of longwave cooling is too weak to generate the circulation strong enough to effectively supply moisture from the surface. Nevertheless, the dynamic coupling between the cloud and the surface can be restored after sunset.

Because the process is controlled by the amount of energy absorbed by the cloud from solar radiation, Turton and Nicholls (1987) suggested that the occurrence of diurnal decoupling depends on season and latitude. For instance, in midlatitudes, it is far more probable in summer while in subtropics it can be observed throughout the year. The diurnal variations in cloud cover and thickness are particularly pronounced in the regions of subtropical oceans where the gradual transition from stratocumulus to trade wind cumulus takes place (c.f. sec. 1.3.1.5). The variations in cloud cover and thickness related to reversible diurnal decoupling may significantly affect the surface energy balance by altering radiation fluxes in the atmosphere. Therefore, this phenomenon is also of interest from the point of view of global and regional climatology.

Caldwell et al. (2005) studied the diurnal cycle with the focus on buoyancy flux and its contribution towards the TKE budget. They found that, in accordance with the changes in the cloud structure including thickness and LWP, B inside the cloud is maximum during nighttime and minimum during daytime (Fig. 1.13). Negative B below the cloud base starts building up around sunrise and persists throughout the morning and the rest of the day. The deviation of cloud base height from the surface LCL appears at the same time as the onset of negative B. In general, the STBL remains decoupled during daylight but restores a considerably well-mixed state at night.

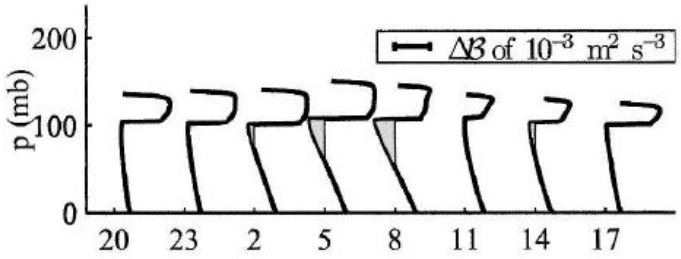

Figure 1.13: Diurnal variations in the profile of buoyancy production/consumption obtained with a mixed-layer model fed with observations. Negative values are indicated with grey shading. From Caldwell et al. (2005).

The changes in net cloud top radiative cooling often trigger complex feedbacks in the dynamics of an STBL. For instance, increased cooling leads to stronger circulation, increased entrainment into the STBL, decreased relative humidity, and increased surface latent heat flux. Such feedbacks operate also in response to the diurnally changing forcing from the cloud top, however with a specific timescale. Zheng et al. (2018b) found that the timescale for the response of latent heat flux to the diurnal changes in cloud top radiative cooling is around 4 hours. They underline that the common emergence of cumulus clouds below stratocumulus, symptomatic for a decoupled STBL, is not merely a part of the diurnal cycle, but the lifetime of the cumulus-coupled stratocumulus can be as long as several tens of hours. The decoupling can then be considered as a rather permanent state. The strength of cumulus convection is modulated by the diurnal cycle but those clouds do not dissipate completely at night. In cumulus-coupled STBLs, the operation of the radiation–turbulence–entrainment–flux feedback connecting the cloud top with the surface is suppressed Zheng et al. (2018b). For instance, surface Q_l in coupled STBLs is usually of the same order as cloud top radiative cooling but in decoupled STBLs with cumulus, there is negligible influence of cloud top cooling on surface moisture and Q_l, at least on the diurnal timescale. In the latter case, Q_l is often significantly larger than cloud top radiative cooling. Stronger surface forcing further reduces the importance of cloud top processes for driving convective circulation. It may finally lead to the dissipation of stratocumulus and the transition into shallow cumulus convection regime.

1.3.1.3 Warm air advection

Low-level warm air advection in the atmosphere corresponds to an STBL moving over the progressively colder ocean surface. Surface cooling contributes to stabilizing the subcloud portion of the boundary layer. This promotes decoupling because much stronger driving from cloud top would be required to generate the circulation capable of mixing throughout the entire depth against the stable stratification. In contrast to the previously described mechanisms, cumulus convection is prohibited due to the stability and negative surface heat fluxes (Zheng and Li, 2019). The weakened circulation and turbulence reduce the cloud top entrainment which, in turn, extends the lifetime of the decoupled stratocumulus until it runs out of moisture due to limited delivery. The dissipation may last several tens of hours. The decoupling due to warm air advection is often observed in the warm sectors of midlatitude cyclones over cold oceans (Zheng and Li, 2019).

In principle, the deepening-warming mechanism (sec. 1.3.1.1) can be considered a strong cold air advection because an STBL moves over gradually higher SSTs. Zheng et al. (2020b) argued that STBL advection and related decoupling should be treated within a uniform framework which spans the wide spectrum of possible advection events: from an extreme cold air advection to an extreme warm air advection. The former is typical for the trade winds in subtropics, the latter for cyclones at higher latitudes. The cold air advection is associated with intensified turbulence and mixing while the warm air advection with stable stratification and turbulence suppression. Interestingly, both can lead to boundary layer decoupling (Fig. 1.14), yet in a different time span. The cold air advection can induce decoupling on shorter time scales. However, it needs to be sufficiently strong in order to trigger rapid deepening-warming. According to Zheng et al. (2020b), the rate of change for SST should exceed 5 K per day. In general, an STBL becomes more decoupled for stronger advection events (relevant for both extremes) but the sensitivity is weaker for shallow boundary layers which require less mixing intensity to remain coupled.

1.3.1.4 Precipitation evaporation

Stratocumulus clouds often precipitate in the form of drizzle which in large part evaporates before reaching the surface (Wood, 2012). Evaporation is connected with latent heat consumption, hence with cooling, which is localized in the subcloud portion of an STBL. This cooling contributes to the stabilization of the STBL.

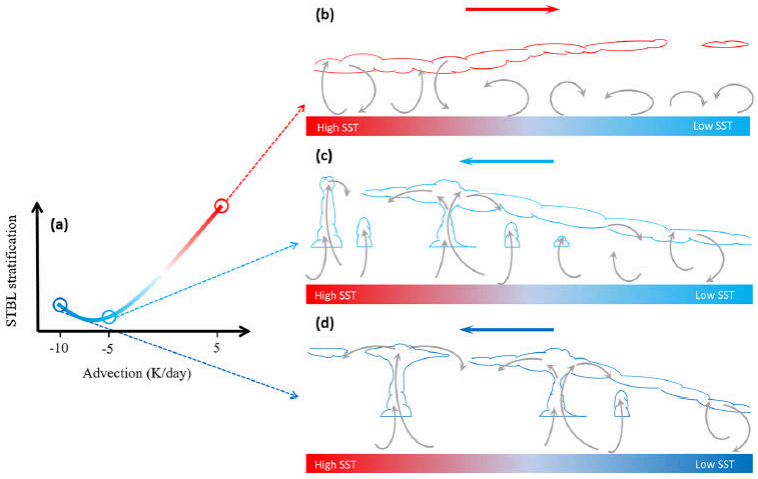

Figure 1.14: Schematic illustrating the response of STBL coupling state to low-level temperature advections. From Zheng et al. (2020b).

The effect of evaporating precipitation on the stratification can be conceptually considered as the transfer of energy from the subcloud layer (where precipitation evaporates consuming latent heat) to the cloud layer (where water vapor condensates releasing latent heat). The stable stratification suppresses circulation, turbulence and mixing. As in the case of warm air advection, stronger driving would be required to perform work against stability. Because cloud top radiative cooling stays rather constant instead, the boundary layer decouples.

Precipitation evaporation was observed by Caldwell et al. (2005) to work in cooperation with solar insolation in driving the diurnal cycle (sec. 1.3.1.2). Although drizzle is only a relatively small term in the STBL moisture budget, it substantially reduces the subcloud buoyancy flux. Because stratocumulus clouds precipitate more heavily late in the night and early in the morning (owing to maximum cloud thickness and LWP), drizzle evaporation may induce weak decoupling during the early morning hours. The decoupled structure is then maintained throughout the day by shortwave absorption. Indeed, Caldwell et al. (2005) found negative B below the cloud already around 8:00 local time (Fig. 1.13) which is earlier than expected for the effect of shortwave heating alone.

Dodson and Small Griswold (2021) stressed out that the actual effects of precipitation on the STBL coupling state may be subtle and should be considered carefully. For instance, the profile of evaporative cooling might play a role. If the most of precipitation water is contained in relatively small droplets, they evaporate high above

the surface. Then, cooling is to a large extent confined in the upper part of the subcloud layer. Under such conditions, evaporation contributes to the destabilization and mixing of the subcloud layer but towards the stabilization of the cloud layer.

1.3.1.5 Stratocumulus to cumulus transition

Stratocumulus decoupling is a factor which strongly influences further evolution of the cloud pattern and the boundary layer structure. It constitutes an intermediate stage of transition from overcast stratocumulus into shallow cumulus convection over subtropical oceans as the air masses are advected by the trade winds towards the equator (Albrecht et al., 1995; Bretherton and Pincus, 1995; Bretherton et al., 1995; Bretherton and Wyant, 1997; De Roode and Duynkerke, 1997). The successful representation and prediction of such a transition between the two boundary layer regimes pose a challenge for atmospheric general circulation models (Xiao et al., 2011, 2012), in large part due to the limited understanding of the interactions of various processes involved which hinders robust parameterizations.

Xiao et al. (2011) indicated that the transition is controlled mostly by the surface fluxes and the properties of the FT. Decoupled STBLs are far more likely to destruct and evolve into shallow trade wind cumulus regime, in particular when there is a possibility of strong buoyancy reversal in the course of mixing at the cloud top. Due to the decoupling, the effect of entrainment drying is trapped in the cloud layer instead of being redistributed down to the surface as in a coupled STBL. This makes the cloud top entrainment instability (CTEI) mechanism (Deardorff, 1980; Randall, 1980) more efficient in destroying a decoupled cloud.

1.3.2 Cloud structure

Decoupled stratocumulus layers tend to reside at higher altitudes above sea level and to be deeper than coupled ones (Dong et al., 2015). In accordance, their LWP is larger, similarly to effective droplet radius r_e (Dong et al., 2015). On the other hand, STBL decoupling often results in the breaks in stratocumulus deck due to the limited moisture supply and weaker circulation homogenizing the cloud structure. The reduced cloud cover can lead to stronger surface forcing, increased intensity of cumulus convection and decreased frequency of stratocumulus as well as its enhanced mesoscale variability. Decoupled stratocumulus clouds with cumulus underneath (C_L8) exhibit positive skewness of LWP statistics. This property was exploited

by Zheng et al. (2018c) to design a method of detecting decoupling in subtropical marine clouds from satellite products. The dynamics of a shallow overcast well-mixed STBL and a deep decoupled STBL with broken clouds are compared in the insightful schematic (Fig. 1.15) by Wood (2012).

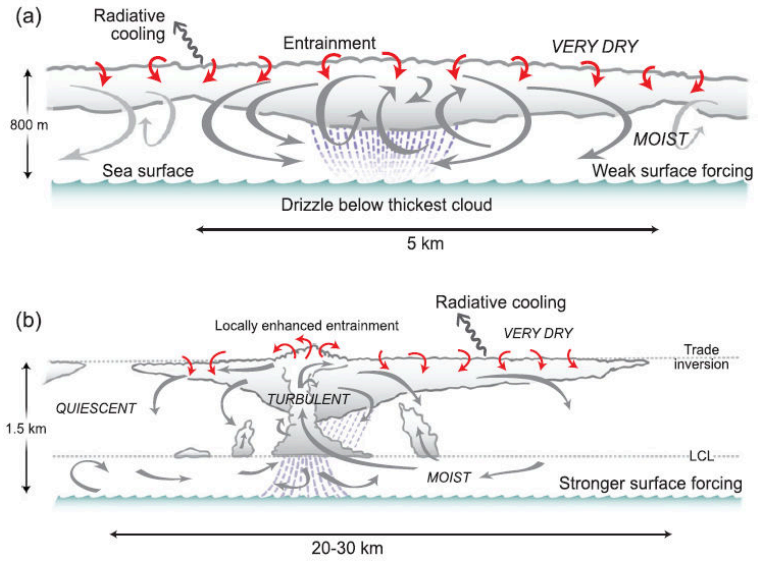

Figure 1.15: The structure of marine stratocumulus in (a) a shallow, well-mixed and (b) deep, cumulus-coupled boundary layer. Gray arrows indicate the primary motions on the scale of the boundary layer, while smaller red arrows indicate the small-scale entrainment mixing at the inversion. From Wood (2012).

The primary process regulating the cloud structure and boundary layer dynamics is cloud top radiative cooling. It was found to stay remarkably similar independent of the STBL depth or its coupling state (Zheng et al., 2018b). Therefore, relatively shallow STBLs are almost always well-mixed while relatively deep STBLs are almost always decoupled. However, for STBLs of medium depth, the coupling state depends on the strength of cloud top radiative cooling and other processes.

Precipitating decoupled clouds were found to have larger total cloud fraction and reflectivity than similarly precipitating coupled clouds (Goren et al., 2018). This can be related to the open cell mesoscale convection pattern which is frequent for coupled stratocumuli that precipitate heavily. The mechanism driving the transition from closed to open cell convection does not work as efficiently in decoupled STBLs because intensive downdrafts are often decelerated by a stable transition layer (TSL). This prevents them from reaching the surface and generating strong gust fronts which play an important role in inducing overruning mixing and cloud layer collapse.

1.3.3 Stratification

When an STBL becomes decoupled, several distinct sublayers can be distinguished inside. The radiatively driven stratocumulus layer (SCL) and the subcloud layer (SBL) in the upper part may be still mixed by negatively buoyant eddies generated at the cloud top and positive buoyancy due to latent heat release. The surface mixed layer (SML) at the bottom may be mixed by positive buoyancy or shear generated close to the surface. A stable or conditionally unstable intermediate transition layer (TSL) emerges in between.

Conserved variables (θ_l, θ_e, q_t) are not necessarily constant with height but may feature pronounced gradients in the transition zone. However, they are often still maintained relatively constant inside the SCL and inside the SML separately (subject to the internal dynamics of those sublayers). The sublayers of a decoupled STBL are marked next to the example profiles in Fig. 1.16.

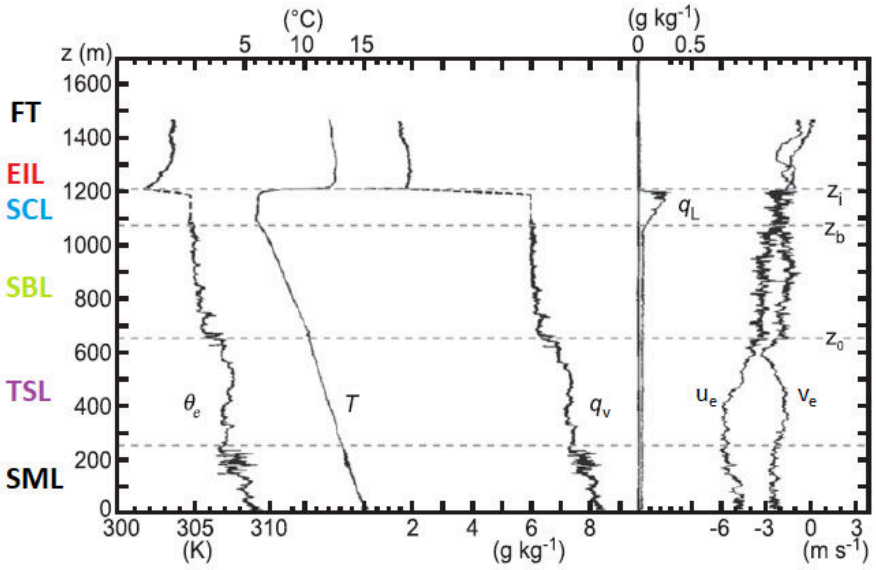

Figure 1.16: Stratification of a summertime decoupled STBL over the North Sea. Vertical profiles of equivalent potential temperature θ_e, temperature T, water vapor q_v and liquid water q_l mass fraction, eastward u_e and northward v_e wind components. Labels on the left denote the sublayers. Adapted from Nicholls and Leighton (1986).

The properties of the transition and the details of the stratification in decoupled STBLs vary between specific cases. For instance, Nicholls (1984) observed no independent TSL and SBL. In their study, the bottom of the deep SCL was practically adjacent to the top of the SML. Nevertheless, despite the lack of clear indications of

decoupling in the thermodynamic profiles, they diagnosed it based on the analysis of the turbulent fluxes (c.f. sec. 1.3.4.2) by comparing them with the fluxes which would be needed to maintain the well-mixed conditions in the entire STBL.

On the other hand, Nicholls and Leighton (1986) reported a shallow SCL mixed with a relatively deep SBL (Fig. 1.16). The TSL extended over the height range of a few hundred meters. It was clearly distinguishable by the gradients of θ_e and q_v at its top and bottom. Interestingly, the flow inside the TSL was characterized as nearly laminar and wind shear was noticed.

The nontrivial structure of decoupling was also described by Tjernström and Rogers (1996). Their first observational case featured the TSL depth between 2 and 300 m, while the second from a few tens to 100 m. In the former, a double-layer structure of the TSL was noticed, with a wind jet in the middle. In both, the top of the SML (the bottom of the TSL) was indicated by the gradients in conserved variables, in contrast to the boundary between the TSL and the SCL. The turbulence associated with the cloud was confined in the SCL, i.e. there was no SBL dynamically mixed with the SCL.

Lambert et al. (1999), who focused on the properties of the SML, complained that the top of the SML was not indicated by any strong vertical gradient in potential temperature or moisture in their individual profiles because that difference was of the same order as the typical turbulent fluctuations in the SML. This is the reason why they developed a method for diagnosing decoupling based on the profile of the TKE dissipation rate (see sec. 1.3.4.3). Nonetheless, they demonstrated the gradients are indeed visible in the profiles averaged with respect to normalized height over many individual penetrations (Fig. 1.17). It can be seen that potential temperature is well mixed from the surface up to the top of the SML while it is stably stratified above. Humidity slightly decreases with altitude in the SML. Similarly, horizontal wind speed and direction were constant in the SML but changes could be spotted in the upper portion of the STBL. The same conclusions were reached by Durand and Bourcy (2001).

In a decoupled STBL, the LCL associated with the conditions in the SML differs substantially from the actual observed stratocumulus base. This LCL is located mostly above the top of the SML (Lambert et al., 1999). The TSL is often stable to dry convection but unstable to moist convection (Tjernström and Rogers, 1996; Lambert et al., 1999). Conditional instability allows for cumulus updrafts to penetrate through and intermittently restore the coupling between the moisture source

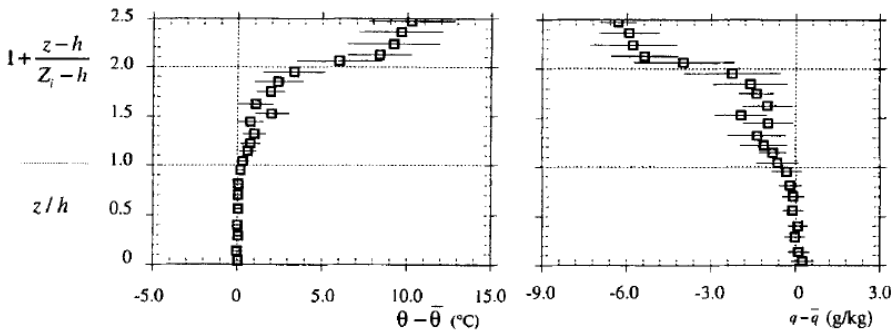

Figure 1.17: Stratification of an autumn decoupled STBL over the ENA during the SEMAPHORE field project. Vertical profiles of potential temperature (left) and specific humidity (right) relative to the SML mean, averaged with respect to height which was normalized to the SML depth h and the inversion height Z_i. Horizontal bars give RMS values among the samples. From Lambert et al. (1999), their original notation.

at the ocean surface and the stratocumulus cloud (Bretherton and Wyant, 1997; De Roode and Duynkerke, 1997).

Objective criteria developed to diagnose decoupling in experimental data usually exploit the properties of the STBL stratification described above (see sec. 4.1). Those criteria are often based on the basic thermodynamic quantities: the difference in moist-conserved variables between the lowermost and the uppermost portion of the STBL or on the difference between the LCL calculated for surface conditions and the actual CB (Wood and Bretherton, 2004; Jones et al., 2011; Ghate et al., 2015). On the other hand, modeling studies followed a more dynamically oriented diagnostic criterion: the ratio of negative and positive portions of the buoyancy flux (c.f. sec. 1.3.4.2) integrated over the STBL depth (Turton and Nicholls, 1987; Bretherton and Wyant, 1997; Stevens, 2000).

1.3.4 Turbulence

The properties of turbulence are closely linked to the degree of boundary layer coupling, because turbulence, together with circulation, contributes to the mixing of air volumes across the STBL depth. However, the interplay between turbulence and stratification is rather complex. Therefore, decoupling can often manifest subtly in various turbulent parameters. Although the concept of circulation and turbulence being insufficiently strong in order to maintain the mixing throughout the entire depth plays a central role in the conventional rationale of decoupling, rather

few works attempted to quantitatively characterize turbulence, in particular with regard to small scales (integral length scale and below). The major reason is the technical difficulty in measuring turbulent fluctuations of wind velocity, temperature or humidity with adequate spatial resolution and accuracy.

1.3.4.1 TKE and turbulent variances

The observations performed in decoupled STBLs (Nicholls, 1984; Nicholls and Leighton, 1986; Tjernström and Rogers, 1996; De Roode and Duynkerke, 1997) indicate that $\langle w'^2 \rangle$ in the upper mixed layer (SCL and SBL) follows relatively well the convective similarity profile (exploiting w_*) when taken upside-down (see explanation in sec. 1.2.3.1). The maximum in $\langle w'^2 \rangle$ is typically located in the upper portion of the cloud while its minima at the very cloud top and around the transition level (see Figs. 1.18 and 1.19).

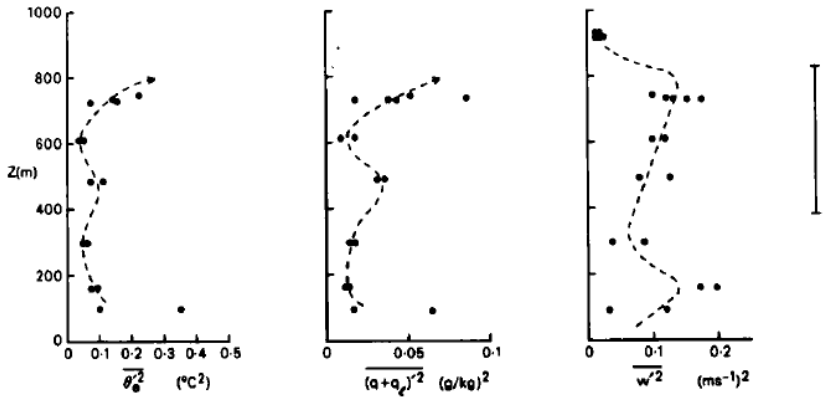

Figure 1.18: Variances of equivalent potential temperature (left), total water mass fraction (center) and vertical velocity (right) measured in a decoupled STBL. The extent of the cloud layer is indicated by the vertical bar. The dashed curves are fitted by eye. From Nicholls (1984), their original notation.

De Roode and Duynkerke (1997) found that also the profile measured in the SML can be approximated with the dry convective scaling (Fig. 1.19). They used the agreement of their observations with the similarity relationships to argue about the relative importance of TKE generation by buoyancy at the cloud top versus that at the surface. Local maximum of $\langle w'^2 \rangle$ in the middle of the SML was also observed by Nicholls (1984) (Fig. 1.18). On the other hand, Tjernström and Rogers (1996) reported a nearly linear decrease of $\langle w'^2 \rangle$ with height inside the SML (their Fig. 9) which is expected for a near-neutral mixed layer.

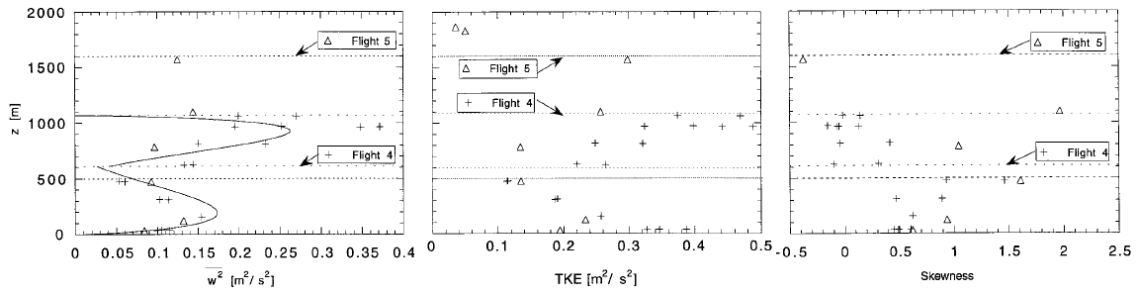

Figure 1.19: Vertical velocity variance (left), turbulence kinetic energy (center) and vertical velocity skewness (right) derived from the horizontal aircraft legs - an example from the ASTEX experiment. Flight 4 was performed in the considerably decoupled STBL with cumulus convection. Dotted lines indicate cloud base and cloud top. Solid curve corresponds to convective scaling in the form given by Lenschow et al. (1980). From De Roode and Duynkerke (1997).

Vertical velocity skewness was found to be negative in the SCL and the SBL while positive in the SML (Figs. 1.19 and 1.20), consistently with the location of principal processes driving the convection (Nicholls and Leighton, 1986; De Roode and Duynkerke, 1997; Lambert et al., 1999; Dodson and Small Griswold, 2021). The strongest negative skewness is typically observed in the middle of the cloud while the strongest positive skewness in the middle of the SML. The sign of the vertical velocity skewness was used by De Roode and Duynkerke (1997) as an indicator of the relative strength of radiative cooling at the cloud top, latent heat release inside the cloud and thermal instability at the surface for driving the circulation. For instance, nearly zero skewness in the cloud indicated that convection due to the release of latent heat was as strong as due to the cloud top radiative cooling.

The variance of horizontal wind fluctuations was measured by Tjernström and Rogers (1996) to decrease with height in the SML in a nearly linear manner. On the other hand, they noticed an increase inside the SCL, with the maximum $\langle u'^2 \rangle$ right below the cloud top. In addition, those authors suggested the profile of $\langle u'^2 \rangle$ in the SCL scales similarly to a dry convective boundary layer when the measurement results are considered upside-down.

The behavior of TKE was documented only by several studies and their conclusions differ. De Roode and Duynkerke (1997) noted a pronounced minimum at the transition level and two local maxima: in the cloud and in the SML, with the former being considerably stronger (Fig. 1.19). In contrast, Dodson and Small Griswold (2021) argued that TKE systematically larger in the SBL in relation to the

SCL distinguishes decoupled STBLs from coupled ones. They suggested that coupled STBLs tend to have two maxima in TKE inside the SCL, one near the cloud base and one near the cloud top, but for decoupled STBLs a single peak in the cloud is more common. On the other hand, Tjernström and Rogers (1996) showed TKE profiles which are approximately constant with height inside the SCL.

The variances of the turbulent fluctuations of temperature and humidity are significant at the locations where mixing between air volumes of contrasting properties takes place: close to the surface, close to the cloud top and in the TSL (Fig. 1.18). Under homogeneous conditions in the middle of the SML and in the middle of the SCL, the variances were observed to be rather weak (e.g. Nicholls, 1984). Lambert et al. (1999) employed ogive analysis to show that large-scale motions ($\gtrsim 1$ km) are responsible for the most of moisture variance. Besides, they examined the profiles of temperature and humidity skewness in the SML (Fig. 1.20) and suggested that the extent of the layers dominated by the entrainment into the SML and by the action of the surface fluxes are indicated by negative and positive humidity skewness, respectively.

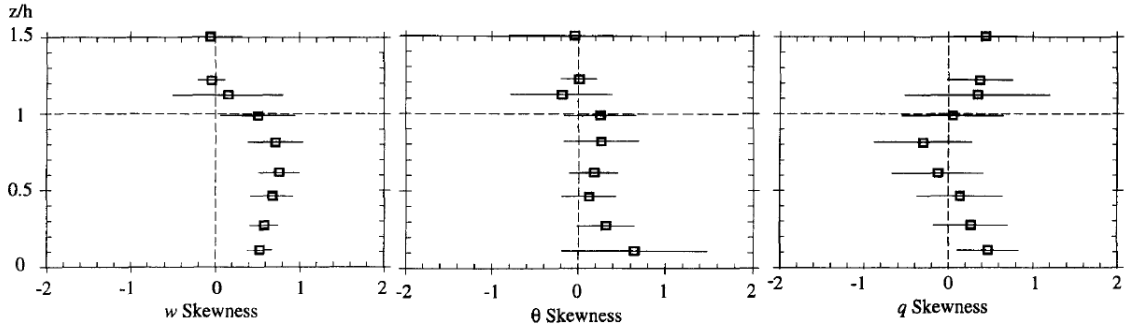

Figure 1.20: Normalized profiles of vertical velocity (left), potential temperature (center) and specific humidity (right) skewness in an SML. Horizontal bars indicate RMS values among the samples. From Lambert and Durand (1999).

1.3.4.2 Turbulent fluxes

The profiles of turbulent fluxes in a decoupled STBL reflect the fact that the upper (SCL and SBL) and the lower (SML) parts separately can be considered well-mixed but they are rather independent of each other. As pointed out by Nicholls (1984): "the measured flux profiles of conservative quantities would not have maintained constant values with height given the observed radiative cooling and gravitational

settling rate profiles". Consistently, the flux profiles are often locally linear with height but of different tendency in the SML in comparison to the SCL and the SBL (see Fig. 1.21).

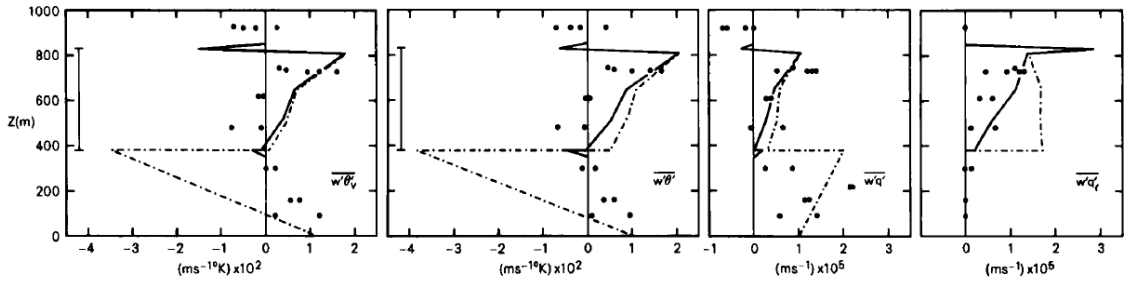

Figure 1.21: Turbulent fluxes of (left to right) virtual potential temperature, potential temperature, specific humidity and liquid water mass fraction in a decoupled STBL: measured (dots) and modeled with a mixed layer scheme where the mixed layer extends from the cloud top down to the cloud base (solid) or down to the surface (dashed). The extent of the cloud layer is indicated by the vertical bar. From Nicholls (1984), their original notation.

Typically, the fluxes decrease with altitude from the surface up to the top of the SML and are small or zero throughout the TSL. Sensible and latent heat fluxes increase again in the SBL and the SCL to reach significant values at the cloud top (Nicholls, 1984; Tjernström and Rogers, 1996; De Roode and Duynkerke, 1997; Lambert et al., 1999; Dodson and Small Griswold, 2021).

Latent heat flux at the surface is largely dependent on the sea surface temperature and air relative humidity. It was shown to be a factor which substantially controls the evolution of a decoupled STBL and its possible transition from stratocumulus to shallow cumulus convection (Bretherton et al., 1995; Bretherton and Wyant, 1997).

The decrease of Q_s and Q_l in the SML was measured to be nearly linear with height (e.g. Tjernström and Rogers, 1996). However, Lambert et al. (1999) found that moisture flux tends to be rather constant with height, followed by a significant gradient at the SML top when large scales contributing to the transport are properly resolved. On the other hand, Q_s decreases linearly in their study and exhibits negative values in the upper portion of the SML (Fig. 1.22).

In the SCL, heat fluxes were found by Tjernström and Rogers (1996) to increase with height as long as the cloud is adiabatic and the turbulence is driven predominantly by buoyancy rather than by wind shear.

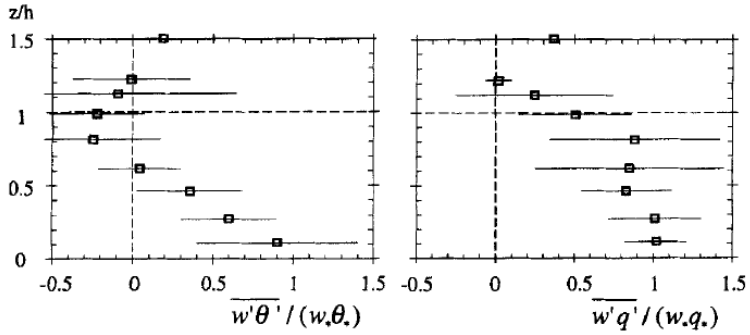

Figure 1.22: Profiles of sensible (left) and latent (right) heat fluxes in an SML normalized with the use of convective velocity, temperature and humidity scales. Horizontal bars indicate the RMS values among the samples. From Lambert and Durand (1999), their original notation.

Similarly to coupled STBLs, Q_l is usually an order of magnitude larger than Q_s (Durand and Bourcy, 2001). In the study of Nicholls (1984), total water flux was of similar magnitude at the surface and at the cloud top. Such balance maintains the boundary layer in a steady state. De Roode and Duynkerke (1997) argued that the turbulent fluxes of water vapor and liquid water are well balanced by the drizzle rate throughout the height which results in a rather minor total water flux (c.f. Eq. (1.4)).

1.3.4.3 TKE budget

In general, the profile of B in a decoupled STBL follows the form similar to a coupled case (see sec. 1.2.3.3). Buoyancy production occurs in the cloud and close to the surface, often with comparable efficiency (Fig. 1.21 left panel, Fig. 1.23). There is an extended region of buoyancy consumption, i.e. negative B, in the TSL (Nicholls, 1984; Nicholls and Leighton, 1986; De Roode and Duynkerke, 1997; Lambert et al., 1999; Durand and Bourcy, 2001). Interestingly, De Roode and Duynkerke (1997) reported very large B at the cloud top in the decoupled STBL shortly before the stratocumulus into cumulus transition.

Lambert et al. (1999) and Durand and Bourcy (2001) examined buoyancy flux together with the relative contributions of temperature $\langle w'\theta' \rangle$ and moisture $\langle w'q_b' \rangle$ terms representing sensible and latent heat, respectively (Fig. 1.24 left panel):

$$\langle w'\theta_v' \rangle \approx \langle w'\theta' \rangle + \underbrace{0.61\langle\theta\rangle\langle w'q_v'\rangle}_{\langle w'q_b'\rangle}. \tag{1.6}$$

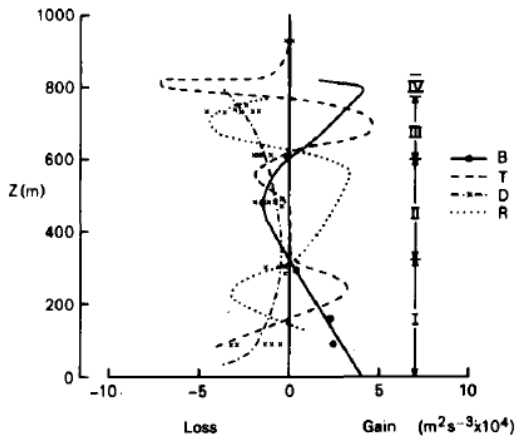

Figure 1.23: Buoyancy B, transport T, dissipation D terms and the remaining residual R of the TKE budget equation in a decoupled STBL. From Nicholls (1984), their original notation.

They found those contributions are of the same order, however of the same sign in the lower part of the SML but of the opposite sign in the upper SML. In turn, B vanishes at the SML top and the entrainment into the SML is rather weak.

Turbulent transport transfers TKE upwards from the efficient source at the surface (Fig. 1.24 central panel). Nicholls (1984) as well as Lambert et al. (1999) found there is a maximum of TKE flux in the middle of the SML which results in TKE loss by transport in the lower half and TKE gain in the upper half of the SML. In the SCL, turbulent transport transfers TKE from the source at the cloud top down into the cloud middle (Fig. 1.23). At the transition, B, Tr and ϵ are rather small, implying that turbulence needs to be maintained by pressure correlation term or it decays leaving a laminar TSL.

TKE dissipation rate in a decoupled STBL often exhibits a local minimum at the transition level (Nicholls, 1984; Lambert and Durand, 1999). This fact was even employed by Lambert and Durand (1999) to detect decoupling. Apart from this minimum, ϵ profile can be considered similar to the coupled case, with maximum at the cloud top and close to the surface (see sec. 1.2.3.3). In the SML, Lambert et al. (1999) found nearly linear decrease of ϵ with height (Fig. 1.24 right panel). In the lower part, $B > \epsilon$, in the upper, $B < \epsilon$, consistently with the upward TKE transport.

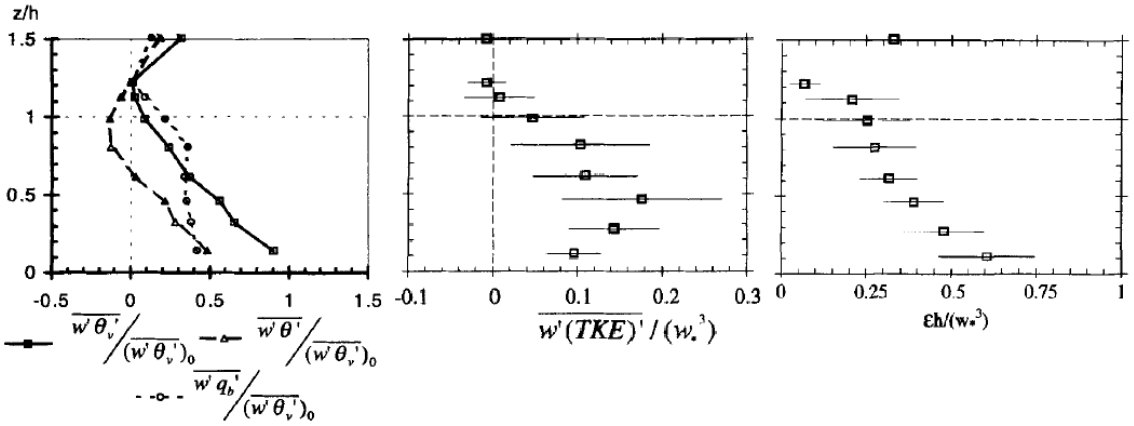

Figure 1.24: Profiles of buoyancy flux (left, squares), TKE flux (center) and TKE dissipation rate (right) inside an SML normalized with the use of surface buoyancy flux and convective velocity scale. In the left panel, the contributions to buoyancy of sensible (triangles) and latent (circles) heat terms are indicated. In the two graphs on the right, horizontal bars indicate the RMS values among the samples. From Lambert and Durand (1999), their original notation.

1.3.5 Aerosols

Decoupling can modify the properties of vertical transport in an STBL, including the transport of surface-generated aerosols towards the cloud base and the aerosols processed by the cloud towards the surface (Zheng and Li, 2019). Consequently, some variability in aerosol properties is expected between coupled and decoupled STBLs or between the sublayers of a decoupled STBL. Indeed, statistical analysis by Dong et al. (2015) demonstrated that decoupled STBLs in the Azores region exhibit lower N_d and lower surface N_{CCN} in relation to the coupled ones. In addition, the coupled STBLs have a stronger positive correlation between surface N_{CCN} and N_d as well as a stronger negative correlation between surface N_{CCN} and r_e.

The cloud droplets and residual particles collected by Wang et al. (2016) in the decoupled stratocumuli over the northeastern Pacific contained significantly lower air-equivalent mass concentration of dissolved non-water substances in comparison to those in the coupled clouds. This fact can be explained by the inhibition of the vertical transport of surface-generated particles (sea salt or ship exhausts).

The same study reported that the composition of residual particles in the coupled clouds features a higher mass fraction of sulfates (typical for precursor emissions from the ocean and ships) and a lower mass fraction of organics, nitrate and ammonium (characteristic for long-range high-altitude transport from distant continental

sources and subsequent downward mixing) than in the decoupled clouds. Such composition makes the particles in the decoupled clouds less hygroscopic.

Cloud water presented higher air-equivalent concentrations of most measured species in the coupled clouds. Only the substances related to the influence of distant continental air masses were more abundant in the decoupled ones. In terms of mass fractions, droplets from the decoupled clouds had a larger contribution of most elements with the exception of those originating from sea salt (Cl, Na, Mg, K).

1.4 Boundary layer in the Eastern North Atlantic

The Eastern North Atlantic is known for the frequent occurrence of stratocumulus clouds (see sec. 1.1.3). The structure of clouds and marine boundary layer have been investigated extensively in a number of field experiments, in particular in the course of the Clouds, Aerosol, and Precipitation in the Marine Boundary Layer (CAP-MBL) campaign (Wood et al., 2015) which involved an almost two-year-long continuous deployment of the Atmospheric Radiation Measurement (ARM) Mobile Facility (Mather and Voyles, 2013) equipped with a wide range of ground-based instruments. The comprehensive statistical analysis of the cloud and boundary layer properties was provided by Rémillard et al. (2012) and Ghate et al. (2015). Similarly to the previous experiments, the measurements analyzed in the present study were collected in the vicinity of the Graciosa island in the archipelago of Azores (39°N, 28°W). The island is relatively small and located in a distance, upwind from the others. Therefore, this location is considered undisturbed by local pollution and representative for the broad area of the ENA.

1.4.1 Synoptic conditions

The area under consideration is influenced by a wide range of synoptic-scale meteorological conditions. Graciosa is located near the boundary of subtropics and midlatitudes. Therefore, the impacts of both subtropical trade wind system and midlatitude cyclones are relevant (Wood et al., 2015). Surface pressure patterns exhibit seasonal variability which is more pronounced over the ENA than for other semi-permanent subtropical stratocumulus sheets, e.g. in the southeastern or northeastern Pacific.

In the winter season, the influence of the Icelandic low and the Azores high results in a strong meridional pressure gradient. Graciosa lies in the southern portion of midlatitude cyclone tracks, faces southwesterly winds and may experience intense precipitation associated with frontal systems.

In the summer period, the Icelandic low weakens and the Azores high intensifies which results in frequent fair weather conditions and reduced high cloud cover. Winds blow from the directions of NE to SW, depending on the exact location of the center of the high pressure system (Fig. 1.25).

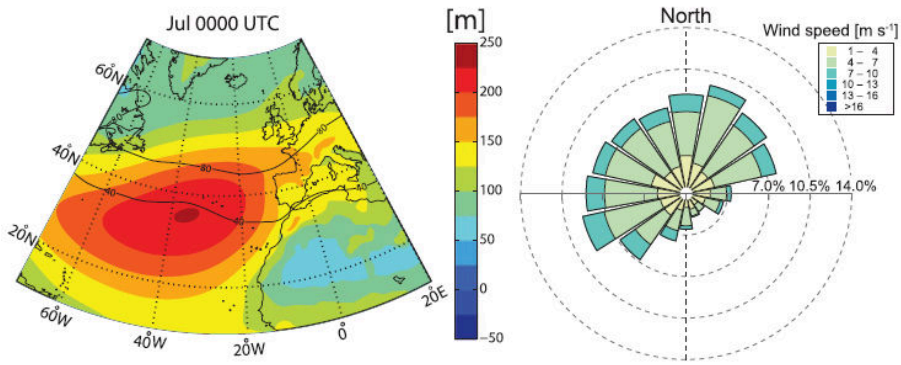

Figure 1.25: (left) Mean 1000 hPa geopotential height (color) for July from the ECMWF ERA-Interim reanalysis. Overlaid are black contours of the standard deviation of the 500 hPa geopotential heights. (right) Surface wind rose for Graciosa in July. From Wood et al. (2015).

1.4.2 Cloud structure

Following pressure patterns, the clouds over the ENA are also subject to seasonal cycle (Rémillard et al., 2012). Overall cloud cover is high, changing from around 60-70 % in summer and early fall to around 80 % in winter and spring (Fig. 1.26). Low clouds are dominant throughout the year (40-60 % cover), in particular in summer and fall which is consistent with the strongest phase of the persistent high pressure system favoring lower tropospheric stability and moisture trapping. Low clouds are accompanied by a range of middle and high level clouds as well as deep convection and frontal systems, especially in winter.

The low clouds category include cumulus (20 % cover, weak annual variability), cumulus under stratocumulus (10-30 %, with maximum in summer and fall) and single layer stratocumulus (0-10 %, with maximum in summer and fall).

Precipitation is noticed pretty often (30-40 % of time, on average half of the cloudy cases). Usually, it does not reach the ground (virga). Intense rainfall is associated to deep cloud systems appearing in fall and winter. Stratocumulus clouds often precipitate (70 %), in particular during the night. Drizzling clouds are deeper and have higher LWP in comparison to non-drizzling ones.

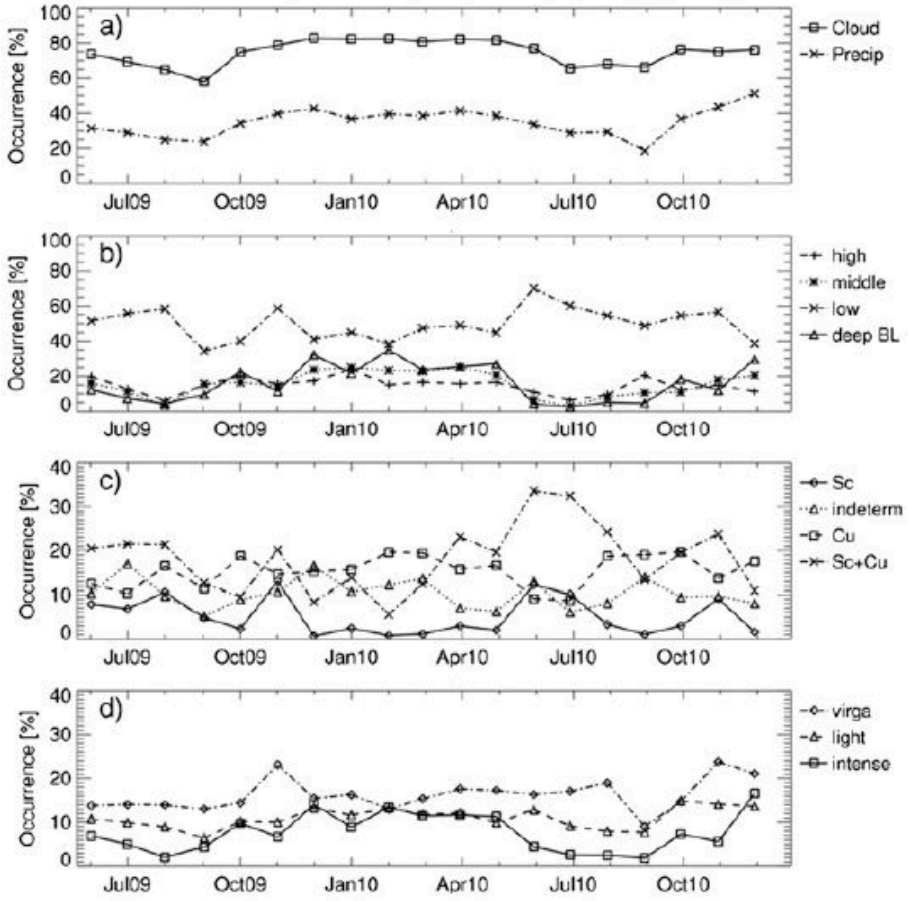

Figure 1.26: Monthly statistics of (a) cloud and liquid precipitation coverage, (b) four main cloud types, (c) low-level clouds, and (d) liquid precipitation types at the ARM ENA observatory. From Rémillard et al. (2012).

1.4.3 Stratification

The presence of a capping temperature inversion and the occurrence of boundary layer decoupling are very frequent. Rémillard et al. (2012) identified temperature inversions in 95 % and transition layers in 92 % of the radiosoundings launched from Graciosa during the CAP-MBL (Fig. 1.27). The depth of the inversion layer was

mostly below 200 m. Significant variations were noted in the inversion strength, expressed by the temperature and moisture differences across the inversion layer. Coupled STBLs were always relatively shallow (below 1 km). Decoupled STBLs contained either one (C_L5) or two (C_L8) cloud layers.

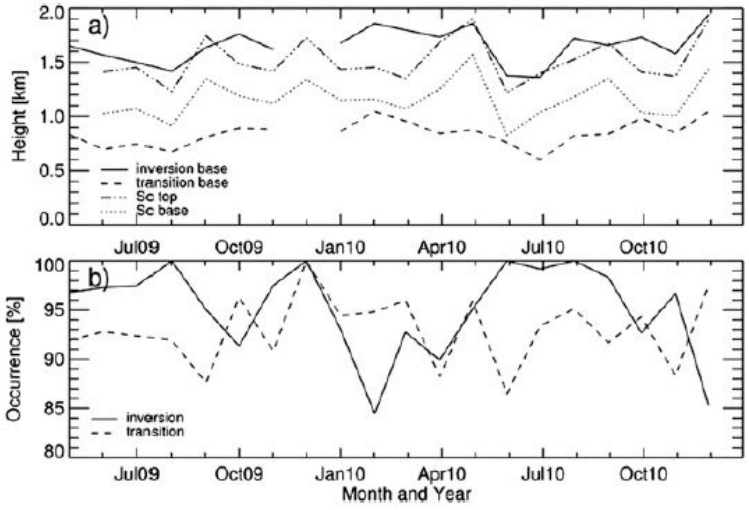

Figure 1.27: Monthly statistics of (a) the transition and inversion layers base height and the stratocumulus clouds boundaries and (b) the occurrences of the inversion and transition layers, as a fraction of the number of soundings per month. From Rémillard et al. (2012).

The distributions of the cloud base heights for cumuli and stratocumuli (Fig. 1.28, left panel) indicate that those cloud types occupy different levels in the atmosphere, consistently with the common C_L8 cloud pattern. The double peak for stratocumulus can be explained by its seasonal cycle. Stratocumulus clouds tend to form at lower heights in summer while a bit higher in spring and fall. The top of the stratocumuli coincides with the inversion base. The base of cumuli coincides with the transition level, however there is greater variability related to their intermittent character (Fig. 1.28, right panel).

Ghate et al. (2015) focused their analysis on STBLs only. They found decoupling in 41 % of the soundings. Although their criterion to diagnose decoupling was based on the difference of virtual potential temperature between the cloud base and the surface $\theta_v^{CB} - \theta_v^{SFC}$, decoupling was also often signaled by the vertical gradient of q_v below the cloud layer. On average, coupled STBLs were characterized as weakly unstable from the surface up to the cloud top. Decoupled STBLs featured a higher cloud base and cloud top. Their stratification was unstable from the surface up

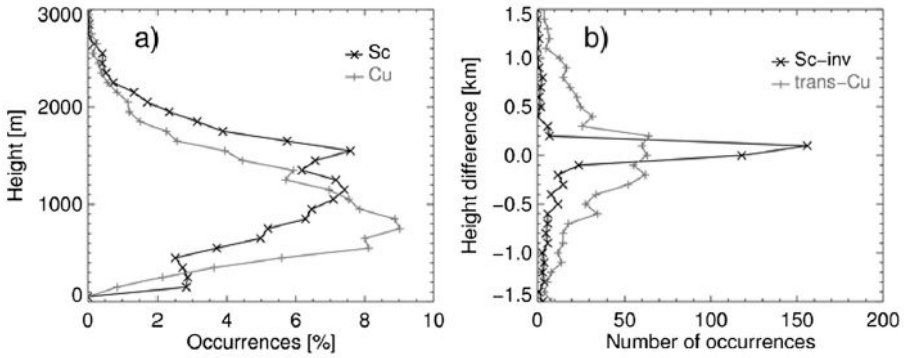

Figure 1.28: (a) Distributions of the cloud base heights for stratocumulus (black line) and cumulus (gray line) clouds. (b) Distributions of the distance between the transition layer and the cumulus base (gray line) and between the stratocumulus top and the inversion base (black line). From Rémillard et al. (2012).

to the LCL calculated for surface conditions, neutral from that LCL to the cloud base, and weakly stable above. Decoupled STBLs were found to be warmer (in terms of potential temperature) and moister, with calmer winds in comparison to coupled ones. Interestingly, there was no statistically significant difference observed in the surface sensible and latent heat fluxes between coupled and decoupled STBLs. Selected statistics characterizing the STBLs over the ENA are listed in Table 1.1.

Table 1.1: Selected statistics of the STBL over the ENA from Ghate et al. (2015).

Parameter	**All soundings**		**Coupled**		**Decoupled**	
	Mean	Std	Mean	Std	Mean	Std
$\theta_v^{CB} - \theta_v^{SFC}$ [K]	1.06	1.46	0.12	0.19	2.20	1.61
Cloud top [m]	1283	365	1000	319	1486	296
Cloud base [m]	1029	404	754	336	1217	348
Cloud thickness [m]	254	173	245	144	268	185
LCL [m]	710	274	752	320	657	225
LWP [$\mathrm{g\,m^{-3}}$]	163	281	81	53	132	171
Q_s [$\mathrm{W\,m^{-2}}$]	7.9	8.9	13.6	14.6	5.9	6.8
Q_l [$\mathrm{W\,m^{-2}}$]	72	46	90	62	65	38
Inversion depth [m]	189	107	159	114	165	95
Inversion $\Delta\theta$ [K]	6.52	2.66	7.01	2.43	5.84	2.37
Inversion Δq_v [$\mathrm{g\,kg^{-1}}$]	-3.69	2.21	-3.64	2.08	-3.80	2.19
Inversion ΔU [$\mathrm{m\,s^{-1}}$]	0.62	1.85	0.15	1.43	-0.03	1.58

1.4.4 Aerosols

Aerosol particles arrive at the ENA from various origins. The advection ranges from clean marine air masses to considerably polluted continental ones from distant locations in North America. Zheng et al. (2018a) classified the air masses advected to Graciosa into four clusters: from North America, from northern Europe, from the Arctic and recirculating around the Azores high. The last pattern was found to dominate over the others in the summertime.

The same study inferred the statistics of aerosol size distribution (Fig. 1.29) and process rates (Fig. 1.30) in a marine boundary layer based on 3-year long continuous measurements at the ARM ENA site. In general, three major modes were distinguished, differing in particle diameter D_p, average number concentrations, seasonal variations, sources and removal processes:

- Aitken mode (At): $D_p \lesssim 100$ nm, $N_p = 330$ cm^{-3}
  The dominant source is the entrainment of long-range-transported or newly-formed particles from the FT. The major sinks are inter-modal coagulation, the condensational growth into accumulation mode and the scavenging of interstitial particles by cloud droplets. The overall number concentration is higher in spring and summer, lower in fall and winter, possibly due to the more efficient new particle formation in the FT occurring in spring and summer.

- accumulation mode (Ac): $100 \lesssim D_p \lesssim 300$ nm, $N_p = 114$ cm^{-3}
  The major sources are the entrainment from the FT, the condensational growth of Aitken mode and sea spray aerosol (SSA) emission. Their efficiency is subject to strong seasonal changes. The dominant sink is the in-cloud coalescence scavenging. The mode exhibits higher N_p in spring and winter, lower in summer. Such a pattern is consistent with the fact that anthropogenic emissions are responsible for the vast part of the entrained FT particles.

- larger accumulation mode (LA): $D_p \gtrsim 300$ nm, $N_p = 14$ cm^{-3}
  The dominant source of the particles in this mode is SSA emission. Because it is highly dependent on mean wind speed, the number concentration peaks in winter while it is significantly smaller in summer. The sinks are the in-cloud coalescence scavenging and the dilution of air volumes by the entrainment from the FT.

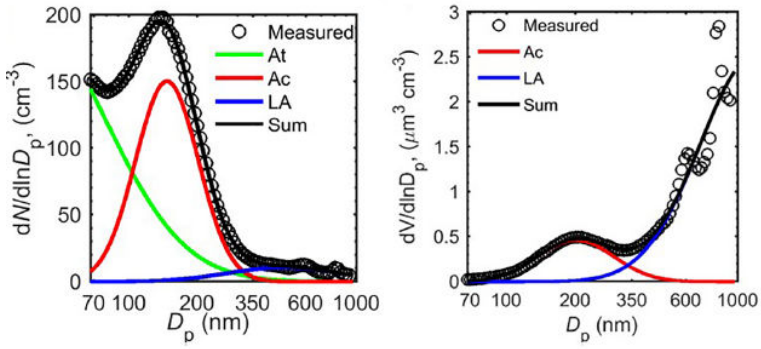

Figure 1.29: Number (left) and volume (right) aerosol particle size distribution measured at the ARM ENA site with fitted lognormal modes: Aitken (At), accumulation (Ac) and larger accumulation (LA). From Zheng et al. (2018a).

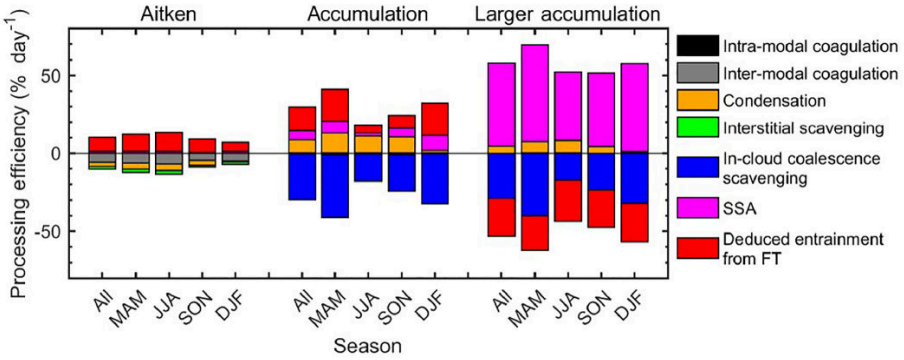

Figure 1.30: Processing efficiency of the major source and sink processes for the three aerosol modes in the marine boundary layer over the ENA in different seasons. From Zheng et al. (2018a).

Thanks to their sufficient size, most of the particles of the accumulation and larger accumulation modes can serve as CCNs. Importantly, the accumulation mode has far higher N_p which implies that the entrainment from the FT is the principal source of CCNs in the marine boundary layer over the ENA. Such CCNs are provided either by the direct entrainment of accumulation mode particles or by the entrainment of Aitken mode particles and their subsequent growth.

Chapter 2

Measurements: the ACORES campaign

The observations analyzed in the present study were collected in the course of the Azores stratoCumulus measurements Of Radiation, turbulEnce and aeroSols (ACORES) field campaign which took place in July 2017 in the ENA around the island of Graciosa in the Azores archipelago. The comprehensive description of the project, including motivation, weather conditions, instrumentation, observation strategy and selected research highlights, is provided in Siebert et al. (2021). Sec. 2.1, 2.2, 2.4 constitute the summary of the relevant points of that overview publication which I coauthored. Sec. 2.5, which explains data selection, was partly included in Nowak et al. (2021).

2.1 General motivation and objectives

The primary objectives of the ACORES project were to investigate the vertical distribution of aerosol particles as well as the microphysical, radiative and turbulence properties of stratocumulus clouds in the region of the ENA. The exchange between the FT and the marine boundary layer in terms of mass, momentum, energy and aerosol particles was studied experimentally. The interaction between the STBL and the FT occurs in the EIL, often only a few tens of meters thick. Therefore, the properties of the EIL are crucial for the exchange processes and the review article of Wood (2012) called for high resolution and collocated measurements of this layer:

> The nature of the EIL, particularly the strength of the gradients in buoyancy and horizontal winds, determines cloud-top entrainment

> (Wang and Albrecht, 1994; Gerber et al., 2005; De Roode and Wang, 2007). High temporal resolution and collocated measurements of liquid water, temperature, inactive tracers, humidity and turbulence, preferably from a slow-moving or stationary platform [e.g., the ACTOS helicopter platform; Siebert et al. (2006b)], will be required to fully characterize and understand the EIL and how it affects entrainment.

Moreover, the research topics of the ACORES campaign included the stratification of the boundary layer and the FT in terms of thermodynamics and turbulence under cloudy and cloudless conditions as well as the influence of decoupling on the vertical transport of various constituents through the boundary layer. In addition to aerosol stratification, the observations targeted related processes such as new-particle formation, the influence of aerosol long-range transport and aerosol–cloud interactions.

2.2 Observation strategy

High-resolution and closely collocated in situ and remote sensing airborne measurements of thermodynamics, turbulence, radiation, aerosols, cloud liquid water, cloud microphysics and cloud geometry were performed with the two instrumental platforms which were combined and flown as an external cargo under a helicopter: (i) the Airborne Cloud Turbulence Observation System (ACTOS) (Siebert et al., 2006a), maintained by the Leibniz Institute for Tropospheric Research (TROPOS), and (ii) the Spectral Modular Airborne Radiation measurement sysTem HELIcopter-borne Observations of Spectral Radiation (SMART-HELIOS) (Henrich et al., 2010; Werner et al., 2013, 2014), maintained by the Leipzig Institute for Meteorology, Leipzig University (LIM).

The helicopter, deployed together with the two platforms at the airport of Graciosa, performed vertically resolved profiling of the lower atmosphere from the ground up to 3 km which allowed to cover the whole boundary layer and the lower part of the FT. Each flight was about 2 hours long, hence represented quite a limited area and time period. The helicopter-borne observations were complemented with the two continuously running ground-based stations: (i) representative for the FT – on the slope of Mount Pico at the nearby Pico island – Observatório da Montanha do Pico (OMP) (Kleissl et al., 2007); (ii) representative for the surface – next to

the Graciosa airport – Atmospheric Radiation Measurement Eastern North Atlantic observatory (ARM ENA) (Wood et al., 2015). The measurement area together with the airborne platforms and the ground-based stations is illustrated in Fig. 2.1.

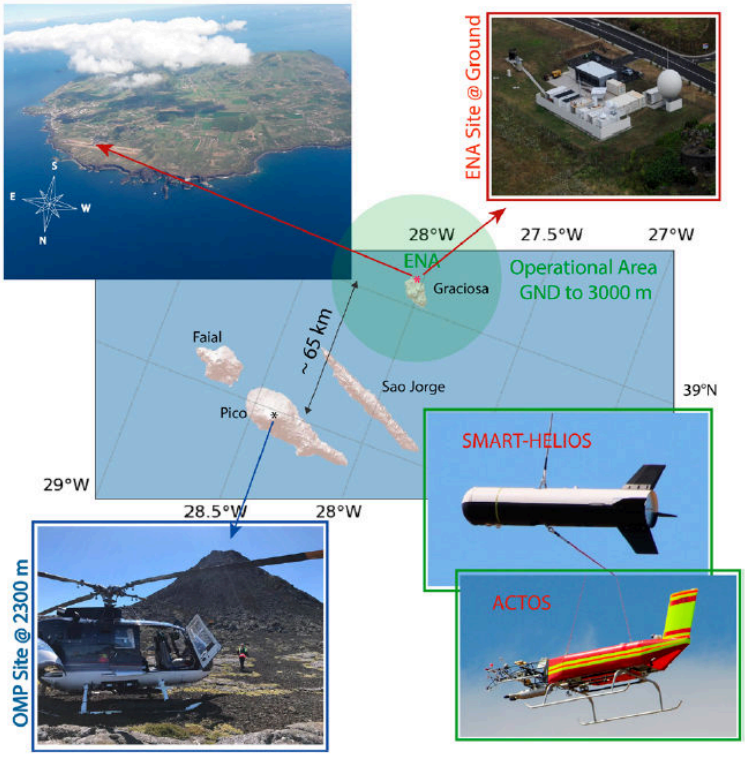

Figure 2.1: Airborne platforms and ground-based measurement stations involved in the ACORES campaign: the helicopter-borne instrumental payloads ACTOS and SMART-HELIOS, the continuously running stations ARM ENA and OMP. From Siebert et al. (2021).

The observation strategy together with the mean conditions in the STBL and the main investigated processes is shown schematically in Fig. 2.2. Both instrumental payloads were carried by the helicopter BO-105 as two separate external cargos on one long tether. SMART-HELIOS was mounted 20 m below the helicopter and ACTOS another 150 m underneath. The main concept of this configuration is for SMART-HELIOS to fly over the cloud to measure radiation and sample cloud properties with remote sensing, while for ACTOS to fly inside the cloud to measure dynamic, thermodynamic, turbulence and microphysical parameters. Such a configuration results in an almost perfect spatial collocation of in situ measurements (ACTOS) and remote sensing (SMART-HELIOS) whereas the helicopter can safely operate within the regime of visible flight rules.

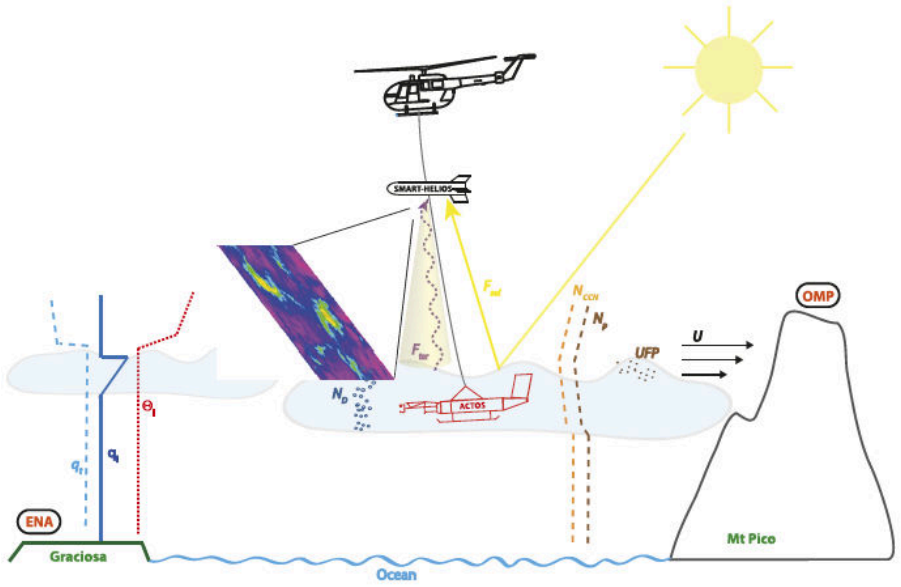

Figure 2.2: Schematic of the sampling strategy during the ACORES together with the main processes in the STBL. Typical mean profiles are shown for total water mass fraction q_t, liquid water mass fraction q_l, liquid water potential temperature θ_l, horizontal wind speed U, aerosol particle concentration N_p, CCN concentration N_{CCN}. Solar F_{sol} and terrestrial F_{ter} irradiances as well as cloud droplet concentration N_d are also indicated. Ultrafine particles (UFP) were often reported around the cloud top. From Siebert et al. (2021).

The unique sensor package on ACTOS allows for high spatial resolution in situ measurements thanks to the high sampling rates of the individual instruments and the relatively low typical true air speed of the helicopter (20 m/s) in comparison to a fast-flying research aircraft. In addition, low true air speed allows to minimize technical issues usually disturbing airborne measurements e.g. related to particle inlets or sensor wetting (Wendisch and Brenguier, 2013).

Helicopter flights during ACORES were typically performed over the ocean inside the 10 by 10 km square adjacent to the northern coast of Graciosa (red box in Figs. 2.6 and 2.9). Specific flight paths and maneuvers depended on a local cloud situation. Within the flight time of two hours, the usual pattern involved: a vertical profile up to roughly 2000 m a.s.l., a few 10 km long horizontal legs at selected levels to derive covariances and several dolphin-like steep porpoise dives around the cloud top and the EIL.

2.3 Instrumentation

The complete instrumentation of ACTOS, SMART-HELIOS, ARM ENA and OMP is listed in Siebert et al. (2021) in their Tables 1, 2 and 3. In the current study, I used the selected data recorded by the instruments onboard ACTOS and the selected supporting measurements performed at the ARM ENA station. The measurements onboard ACTOS which are relevant for this work include:

- horizontal wind vector (u_e, v_e) in the Earth-fixed system and longitudinal–vertical wind velocity components (u, w) in the platform-fixed system (derivation explained in sec. 3.2) provided by the combination of the ultrasonic anemometer-thermometer Solent HS, Gill Instruments Ltd. (Siebert and Teichmann, 2000), and a high-accuracy motion package (inertial navigation system and GPS);

- temperature T and its small scale fluctuations provided by the cold wire Ultra-Fast Thermometer (UFT) developed at University of Warsaw (Haman et al., 1997; Kumala et al., 2013; Nowak et al., 2018) combined with the precise calibrated slow-response PT100 to obtain fast precise stable signals by complementary filtering (Wendisch and Brenguier, 2013, ch. 2);

- virtual temperature T_v based on the speed of sound measured by the ultrasonic anemometer-thermometer Solent HS, Gill Instruments Ltd. (Siebert and Muschinski, 2001);

- specific humidity q_v provided by the open-path infrared absorption hygrometer LI-7500, LI-COR Environmental Inc. (Lampert et al., 2018);

- liquid water mass fraction q_l determined with the Particle Volume Meter airborne version (PVM-100A), Gerber Scientific Inc. (Gerber et al., 1994; Wendisch et al., 2002);

- number concentration N_p of aerosol particles ($D_p > 6$ nm) measured by the Condensation Particle Counter (CPC) 3762A, TSI Inc.;

- aerosol PNSD provided by the combination of the custom-built Scanning Mobility Particle Sizer (SMPS) developed at TROPOS (Wehner et al., 2010), measuring 6 nm $< D_p <$ 250 nm and the Optical Particle Counter (OPC), Grimm Aerosol Technik Ainring GmbH, measuring 250 nm $< D_p <$ 2.5 µm;

- CCN number concentration N_{CCN} at 0.2 % supersaturation provided by the lightweight mini CCN Counter (miniCCNC) (Roberts and Nenes, 2005).

The instruments listed above or their particle inlets are marked in the photograph of the ACTOS platform in Fig. 2.3.

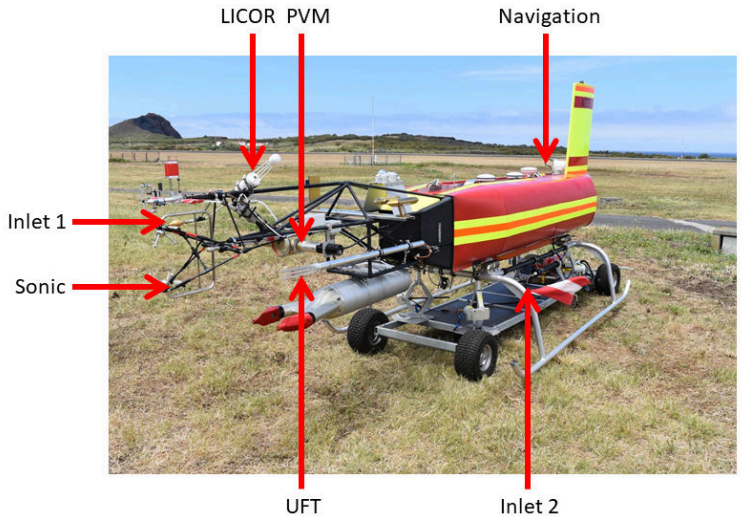

Figure 2.3: Selected instruments and particle inlets onboard the ACTOS platform.

The measurements performed at the ARM ENA utilized in this work include:

- routine balloon radiosoundings products (Keeler et al., 2013);
- daily products of cloud base height as well as range and overlap corrected backscatter coefficient β from the ceilometer (Morris and Ermold, 2013).

Those data were acquired through the ARM Data Discovery website.

2.4 Synoptic conditions

In the period of the ACORES campaign, between 2 and 22 July 2017, a range of synoptic conditions around the Azores archipelago was observed. They were related to the location and strength of the Azores high pressure system as well as occasional front passages. The high was relatively strong which is typical for summer and its center was located west or north from Graciosa.

Siebert et al. (2021) distinguished three periods of prevailing synoptic conditions affecting the atmospheric boundary layer:

> The first synoptic period (**2-11 July**) was characterized by the lowest atmospheric boundary layer temperatures of the entire campaign, associated with relative dry air. This air mass prevailed due to a weak northerly flow and stable conditions at the northeasterly edge of the Azores high pressure system. In this period, cloud cover was low and dominated by thin shallow convection with little amount of precipitation. On 3, 6, and 7 July, frontal systems passed the station leading to a temporal westerly flow associated with an increase in air temperature, humidity and precipitation.
>
> The second period (**12-19 July**) was affected by a weakening and shift of the Azores high pressure system. The center was located further west while a tail of weak high pressure stretched in northeastward direction over the archipelago. During this time an increase of air temperature and humidity within the entire atmospheric boundary layer was observed. Supported by the weaker high pressure, convection amplified within this air mass and led to the development of thicker stratocumulus clouds that produced precipitation. On 17 July a front associated with a strong and quickly eastward-moving low pressure system north of the islands did pass Graciosa and affected the location of the Azores high.
>
> After a second frontal passage on 19 July, the stable conditions recovered with the center of the Azores high located west of the archipelago. This defined the start of the third synoptic period of the campaign (**20-22 July**). Similar to the first period, the boundary layer was dominated by colder, dry air with reduced cloud cover and less precipitation.

Fig. 2.4 presents the relevant maps of mean surface pressure, surface wind vector, and potential temperature at 950 hPa level obtained from the European Centre for Medium-Range Weather Forecasts (ECMWF) ERA5 atmospheric reanalysis (Hersbach et al., 2018a,b). Table 2.1 summarizes the characteristic weather conditions for the three identified periods.

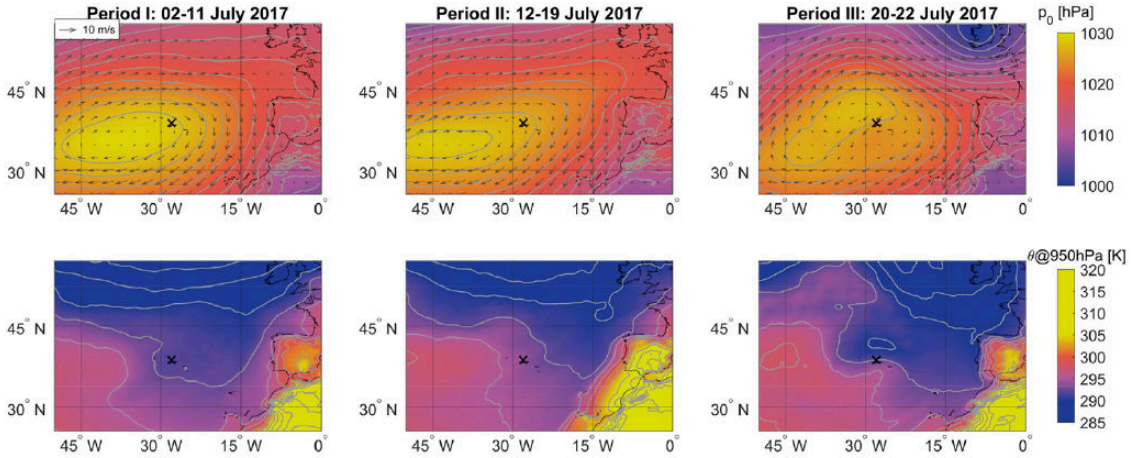

Figure 2.4: Three synoptic periods of the ACORES campaign. Mean surface pressure and wind vectors (top), and potential temperature at 950 hPa (bottom) calculated from the ECMWF ERA5 reanalysis. From Siebert et al. (2021).

Table 2.1: Summary of conditions during the three synoptic periods of the ACORES campaign. From Siebert et al. (2021).

	Dates	**Summary**
Period I	2 - 11 July 2017	Azores High located west, stable conditions with northerly flow of dry and cold air, low cloud fraction with thin shallow convection, less precipitation, front passed on 7/8 July
Period II	12 - 19 July 2017	Azores High centered further west, weak winds, warm and moist air mass, daily cycle of stronger shallow convection with frequent precipitation, fronts passed on 17 and 19 July
Period III	20 - 22 July 2017	Azores High located west, stable conditions with changing winds, dry and cold air mass, low cloud fraction with shallow convection, less precipitation.

2.5 Data selection

In total, there were 17 research helicopter flights performed with ACTOS and SMART-HELIOS within the ACORES project in the period between 2 and 22 July 2017. Each lasted typically two hours. For a complete list see Table 5 in Siebert et al. (2021). Two flights were selected for the comparative study of coupled and decoupled STBLs: flight #5 on 8 July 2017 and flight #14 on 18 July 2017. The choice was dictated by the presence of stratocumulus clouds, STBL stratification

(considerably well-mixed in flight #5, considerably decoupled in flight #14) and a flight pattern involving substantial sampling time below the stratocumulus base.

Segments of two types were selected from the measurement records: vertical profiles (PROFs) and horizontal legs (LEGs). For convenience, for each flight PROFs are ordered chronologically according to their time of execution while LEGs are ordered according to their mean altitude. The segmentation was done manually so that the influence of sharp turns and the pendulum-like motion of the payload is avoided. This resulted in the reduced length of the LEGs, between 3.5 and 12 km. LEGs were flown with a true air speed of 15-20 $\mathrm{m\,s^{-1}}$ and some minor displacements in vertical are unavoidable for the payload on a 170 m long rope. The mean altitudes and exact lengths are listed in Table 2.2.

Table 2.2: Mean altitude and length of LEGs.

Flight #5					
Height [m]	307	553	819	1079	2018
Length [km]	5.44	5.51	7.93	3.94	6.25
Flight #14					
Height [m]	143	287	448	992	2021
Length [km]	8.11	11.92	7.10	4.79	3.49

PROFs are in fact slanted with an ascent or descent rate of about 3-5 $\mathrm{m\,s^{-1}}$ and a true air speed ∼20 $\mathrm{m\,s^{-1}}$ which results in an aspect ratio of 0.15-0.25. The horizontal component of motion is necessary to avoid the downwash of the helicopter rotor affecting wind and turbulence measurements on ACTOS. The initial and final altitudes of PROFs are listed in Table 2.3.

Table 2.3: Initial and final altitude of PROFs.

Flight #5	**PROF1**	**PROF2**	**PROF3**	**PROF4**	**PROF5**
Initial height [m]	85	2005	1065	565	325
Final height [m]	2035	1115	555	305	95
Flight #14	**PROF1**	**PROF2**	**PROF3**	**PROF4**	**PROF5**
Initial height [m]	135	285	465	1905	1315
Final height [m]	295	435	2035	915	175

The chosen segments are marked in altitude profiles in sec. 2.5.1 and 2.5.2 (Fig. 2.7 and Fig. 2.10). The distinction between the two segment types is important for the analysis described in the following chapters, particularly the derivation of turbulence properties.

2.5.1 Flight #5 in the coupled STBL

Flight #5 was performed in the afternoon (14:28-16:26 UTC[1]) on 8 July 2017. That day corresponds to the first synoptic period of the campaign (see sec. 2.4). The surface pressure analysis chart (Fig. 2.5) valid for 12:00 UTC (NOAA Ocean Prediction Center, 2017) indicates the center of the Azores high pressure system was located in the relatively small distance into the northwest direction from the Graciosa island (and slowly moving towards it) which resulted in gentle northerly geostrophic winds (see sec. 4.2.1).

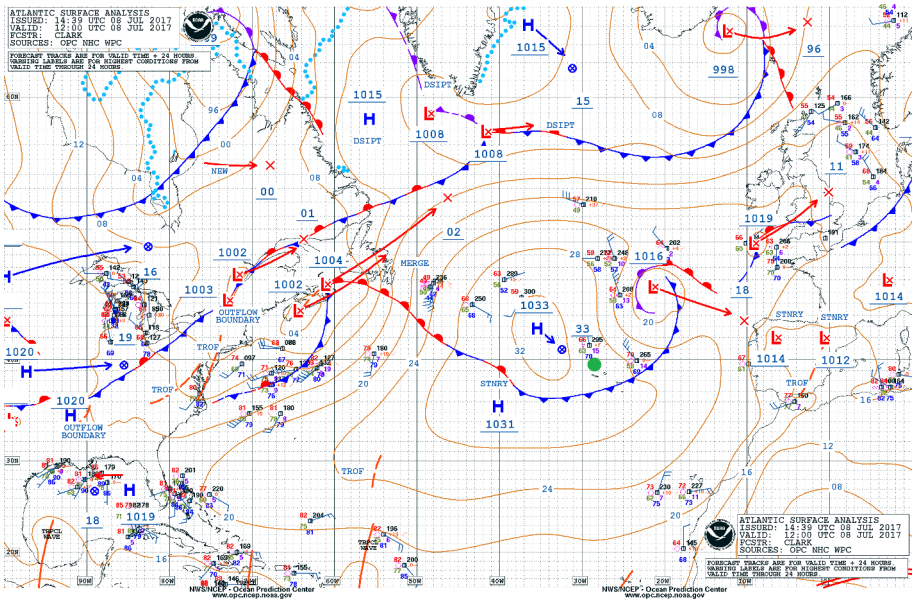

Figure 2.5: Surface pressure analysis chart for the North Atlantic valid for noon on 8 July 2017 issued by the NOAA OPC. Green dot indicates Graciosa.

Stratocumulus clouds emerged behind the cold front which had passed the island the night before (c.f. precipitation pattern described in sec. 4.2.4). The cloud field was moderately thick and quite heterogeneous in structure, with some visible clearings. The satellite image from MODIS on Aqua (Fig. 2.6) confirms this observation, showing dispersed cloud patches in the vicinity of Graciosa.

The flight pattern (Fig. 2.7) involved: a deep PROF from the minimum flight level (60 m) into the FT, two LEGs in the FT with one close to the stratocumulus top, three LEGs in the STBL with one inside the stratocumulus cloud, close to its top. The PROFs are indicated in the figure with different line styles which are

[1]On Azores the local time in summer is equivalent to UTC.

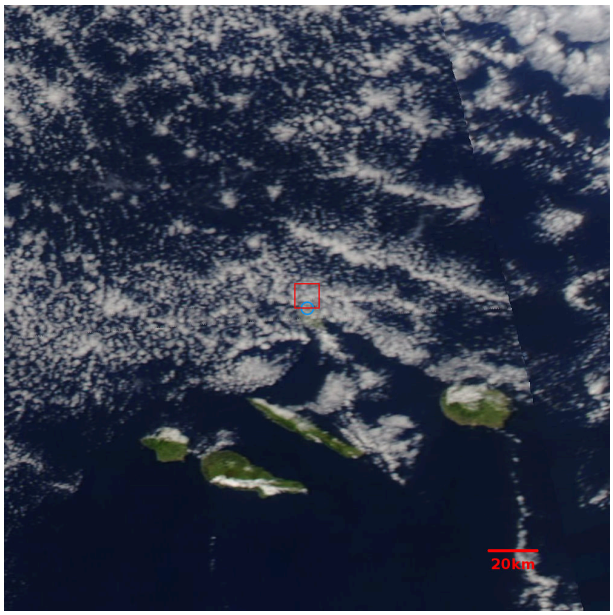

Figure 2.6: Satellite true-color image (250 x 250 km) taken on 8 July 2017 at 15:45 UTC (i.e. during flight #5, the time given corresponds to the left swath covering most of the image) by the MODIS instrument on Aqua overpassing Azores, centered on the Graciosa airport (blue circle), with the overlaid helicopter operation area (red box). The image was acquired from NASA Worldview Snapshots.

used hereafter in the vertical profiles of various derived parameters (ch. 4-6). The altitude ranges corresponding to PROF2-PROF5 of this flight do not overlap, hence they are all marked with dashed lines. The flight pattern consisted of the segments flown either in the east-west or north-south direction.

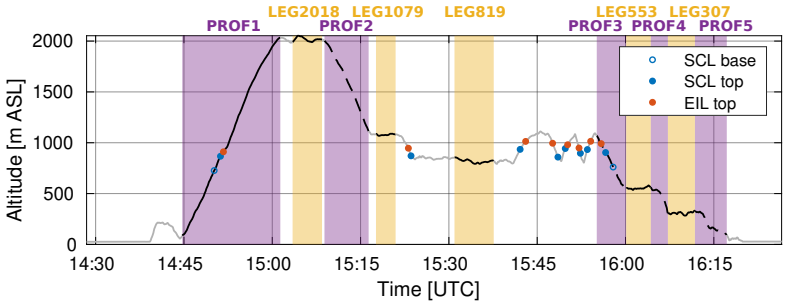

Figure 2.7: ACTOS altitude in flight #5 with the selected PROFs and LEGs. The line styles of the PROFs are consistent with the figures in the following chapters. The altitude ranges corresponding to PROF2-PROF5 of this flight do not overlap and they are all marked with dashed lines. Dots indicate the penetrations of the boundaries of the specific sublayers described in sec. 4.2.

2.5.2 Flight #14 in the decoupled STBL

Flight #14 was performed in the afternoon (15:01-17:04 UTC) on 18 July 2017, shortly after weak precipitation had been noted at the site. That day corresponds to the second synoptic period of the campaign when the center of the high pressure system was located further west from the Azores islands (see sec. 2.4). This is consistent with the surface pressure analysis chart (Fig. 2.8) valid for 12:00 UTC which shows the position of the high to be southwest from Graciosa. Importantly, northwest from Graciosa there is a weak low pressure system quickly moving towards the island. It was mentioned also by Siebert et al. (2021) in their review of synoptic conditions. By the time of the flight, the front had passed Graciosa. Likely, it happened already in the very morning which would explain the origin of heavy precipitation (see sec. 4.3.4) reported at the airport.

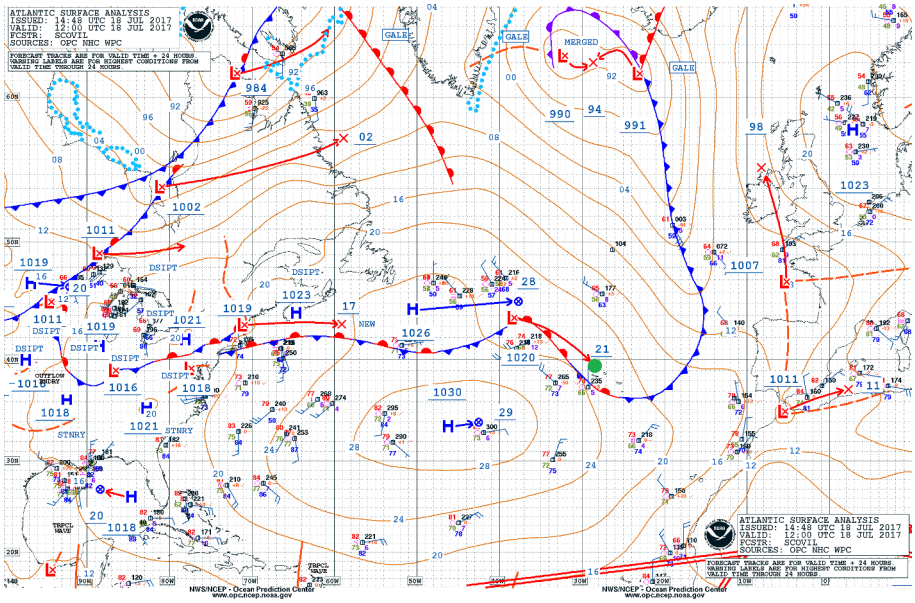

Figure 2.8: Surface pressure analysis chart for the North Atlantic valid for noon on 18 July 2017 issued by the NOAA OPC. Green dot indicates Graciosa.

During the flight, the sky was overcast with stratocumulus clouds of homogeneous structure. Many little cumulus clouds at the initial state of formation were reported over the ocean below the stratocumulus deck. However, they were not observed to reach the stratocumulus base. The MODIS Aqua image (Fig. 2.9) shows a large solid patch of stratocumulus clouds with signatures of a closed-cell convection regime.

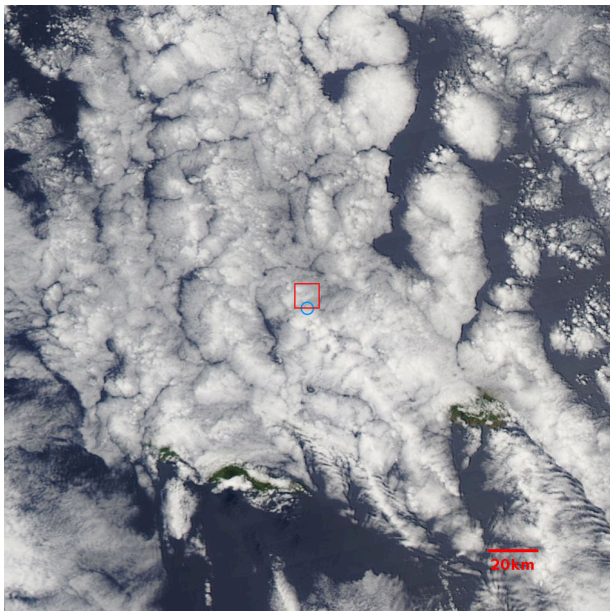

Figure 2.9: Satellite true-color image (250 x 250 km) taken on 18 July 2017 at 14:43 UTC (shortly before flight #14) by the MODIS instrument on Aqua overpassing Azores, centered on the Graciosa airport (blue circle), with the overlaid operation area (red box). The image was acquired from NASA Worldview Snapshots.

The flight pattern (Fig. 2.10) involved: four LEGs in the STBL with one inside the stratocumulus, close to its top, one LEG in the FT and a number of PROFs connecting the LEG levels. In the figure and hereafter, PROF1-PROF3 are all marked with dashed lines because their altitude ranges do not overlap. The whole flight consisted of the segments flown in the east-west direction.

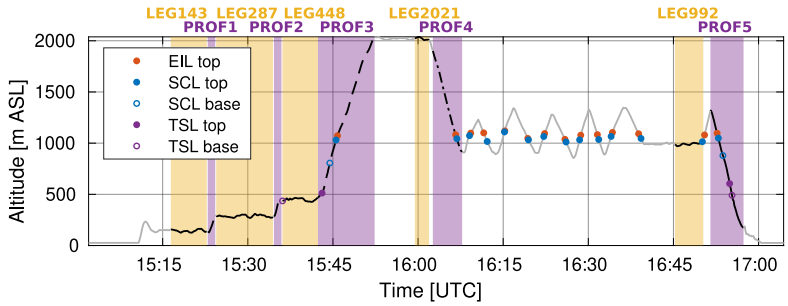

Figure 2.10: ACTOS altitude in flight #14 with the selected PROFs and LEGs. The line styles of the PROFs are consistent with the figures in the following chapters. PROF1-PROF3 are all marked with dashed lines because their altitude ranges do not overlap. Dots indicate the penetrations of the boundaries of the specific sublayers described in sec. 4.3.

Chapter 3

Methods

This chapter describes the selected aspects of the data processing and the details of the derivation methods applied in order to obtain various thermodynamic, turbulence and aerosol parameters which are further used in the comparative analysis of the coupled and decoupled STBLs. Secs. 3.1 and 3.2 contain the material which has been already covered in Nowak et al. (2021). Here, it is expanded with additional details. The content of sec. 3.3 has not been published before.

3.1 Stratification

3.1.1 Meteorological and stability parameters

The vertical segments, marked with purple shading in Figs. 2.7 and 2.10, were utilized to determine the vertical structure of the lower atmosphere. Elementary meteorological conditions as well as the derived stability parameters are shown in Fig. 4.1 for flight #5 and Fig. 4.4 for flight #14. The line style denotes a particular PROF, consistently with the altitude timeseries (Figs. 2.7 and 2.10).

Temperature was measured with the UFT, liquid water mass fraction with the PVM-100A, specific humidity with the LI-7500 (see sec. 2.3). Liquid water potential temperature was calculated following the approximation by Betts (1973):

$$\theta_l = \theta - \frac{\theta}{T}\frac{L_v}{c_p} q_l. \tag{3.1}$$

Horizontal wind speed and direction result from the appropriate standard transformation of the measured flow velocity into Earth-fixed coordinate system, compensating for the platform motion and attitude (Lenschow, 1986; Edson et al., 1998).

Because the helicopter climb rate was not exactly constant in time and individual instruments differ in sampling rate, data points for each variable were grouped and averaged in 10 m high altitude bins (separately for each PROF). To reduce the effect of random eddy penetration and improve clarity, wind profiles were additionally smoothed with a five-point moving average.

LCL was then derived for each altitude level according to Bolton (1980). Such a result is sensitive to gradients of thermodynamic properties in the subcloud layer, signaling the degree of boundary layer coupling. To characterize static stability, Brunt-Väisälä frequency Nb was computed according to:

$$\mathrm{Nb}^2 = \frac{g}{\theta_v}\frac{\partial \theta_v}{\partial z} \tag{3.2}$$

where θ_v was derived from the speed of sound (provided by ultrasonic anemometer-thermometer). To quantify the vertical gradient of horizontal wind, shear rate Sh was obtained following the equation:

$$\mathrm{Sh}^2 = \left(\frac{\partial u_e}{\partial z}\right)^2 + \left(\frac{\partial v_e}{\partial z}\right)^2. \tag{3.3}$$

The derivatives in Eqs. (3.2) and (3.3) were evaluated as the tangents of the linear least-square fits of 10 m binned variables versus z performed inside symmetric five point windows. The ratio of Nb^2 and Sh^2 could be utilized to obtain the gradient Richardson number Ri_g characterizing the relative importance of shear and buoyancy for the stability of the layer (Stull, 1988). However, I do not provide this information because both the nominator and denominator are small numbers, resulting in large uncertainty which makes the outcome rather difficult to interpret.

3.1.2 Decoupling detection

In order to objectively confirm the fact of coupling or decoupling of an STBL, several methods from the literature were employed (Jones et al., 2011; Wood and Bretherton, 2004; Yin and Albrecht, 2000).

The first criterion of Jones et al. (2011) involves the differences of θ_l and total water mixing ratio r_t between the uppermost and the lowermost quarters of the boundary layer. Here, q_t was used instead of r_t. It does not influence the conclusions because those two measures are approximately equal. The sounding is classified as coupled when $\Delta\theta_l = \theta_l^{top} - \theta_l^{bot} < 0.5$ K and $\Delta q_t = q_t^{bot} - q_t^{top} < 0.5$ g kg^{-1}, decoupled

otherwise. The second criterion of Jones et al. (2011) involves the difference between the observed CB and the LCL corresponding to the conditions at the bottom of the boundary layer. It is classified as coupled when $\Delta z = \mathrm{CB} - \mathrm{LCL}^{bot} < 150$ m, decoupled otherwise. Here, I used the mean conditions of the lowest leg (LEG307 for flight #5, LEG143 for flight #14) to estimate LCL^{bot} and q_l measured in PROFs to estimate the CB.

Wood and Bretherton (2004) proposed two decoupling parameters:

$$\alpha_\theta = \frac{\theta_l^- - \theta_l^0}{\theta_l^+ - \theta_l^0} \qquad \alpha_q = \frac{q_t^- - q_t^0}{q_t^+ - q_t^0} \tag{3.4}$$

where superscripts $+$, $-$, 0 denote the values just above the inversion, just below the inversion and in the SML, respectively. They found that α_θ and α_q over the subtropical Eastern Pacific stay in the range from 0 to 0.4, however no exact critical value for decoupling was determined. The higher those parameters, the more decoupled the boundary layer is considered. Here, instead of finding first the height span of the SML, I applied mean values in the lower quarter of the boundary layer ($\theta_l^0 = \theta_l^{bot}$ and $q_t^0 = q_t^{bot}$).

Yin and Albrecht (2000) introduced a stability parameter μ to identify transitions in boundary layer soundings:

$$\mu = -\frac{\partial \theta}{\partial P} + \frac{\varepsilon \theta}{1 + \varepsilon r_v} \frac{\partial r_v}{\partial P} \tag{3.5}$$

where $\varepsilon = R_v/R_d - 1$ depends on the ratio of gas constants for water vapor R_v and dry air R_d while r_v is water vapor mixing ratio. Their procedure detects transition anytime in the subcloud zone the value of μ exceeds by a factor of 1.3 the average $\bar{\mu}$ between 980 and 900 hPa. Here, instead of using pressure levels, I specified $\bar{\mu}$ as the mean value for the whole the boundary layer.

In fact, Eq. (3.5) is of similar form to the derivative of θ_v expanded into "dry" and "moist" contributions corresponding to the gradients of θ and r_v, respectively:

$$\frac{\partial \theta_v}{\partial P} = (1 + \varepsilon r_v) \frac{\partial \theta}{\partial P} + \varepsilon \theta \frac{\partial r_v}{\partial P}. \tag{3.6}$$

The difference is that the contributions in Eq. (3.5) are summed instead of being in partial balance as in Eq. (3.6). Typically, at the transition between the SML and the SBL, θ increases while r_v decreases with height (Turton and Nicholls, 1987). The former contributes to the increase of θ_v, the latter to the decrease so that the

net change is not excessive. However, by adding the contributions one can detect the transition with better sensitivity than using either of the gradients separately.

Following previous studies looking for differences in CTEI between coupled and decoupled stratocumuli (e.g. Xiao et al., 2011), I calculated the Randall-Deardorff parameter (Randall, 1980; Deardorff, 1980):

$$\kappa = 1 + \frac{c_p}{L_v} \frac{\theta_l^+ - \theta_l^-}{q_t^+ - q_t^-}. \tag{3.7}$$

It estimates the potential for buoyancy reversal at the cloud top, i.e. the conditions under which the mixing of the cloudy air volumes with the free tropospheric air can create a mixture denser than any of the initial portions due to evaporative cooling. There is such a possibility if the parameter κ exceeds its critical value of about 0.23.

3.1.3 Radiosoundings

There are typical balloon radiosondes launched from the ARM ENA station on a regular basis to profile the atmosphere (Keeler et al., 2013). The soundings released on a relevant day, a few hours before and after the considered helicopter flight, are used in this study to analyze the stratification with respect to the changes during the day and with respect to the different sampling capabilities of the ACTOS platform and routine radiosondes. Supplementary parameters which are not provided in the data product available through ARM Data Discovery (LCL, μ, Nb and Sh) were derived with the methods analogous to the ones described in sec. 3.1.1.

3.2 Turbulence parameters

The properties of turbulence in the coupled and decoupled STBL were characterized using a number of parameters derived from the high-resolution measurements of flow velocity, temperature and humidity performed onboard ACTOS. Depending on a specific quantity, the results were obtained for vertical or horizontal flight segments which were introduced in sec. 2.5.

In the case of PROFs, the procedure resembles the approach of Tjernstrom (1993). Typically, it involved the computation of a parameter for a timeseries covering the whole flight time. After the timeseries had been computed, appropriate segments were extracted and the data were averaged in 10 m altitude bins (as in sec. 3.1.1).

For LEGs, an entire segment was used to calculate a parameter. Next, each LEG was divided into 7 subsegments of equal length, overlapping by half of the length, and the very same method was applied to calculate this quantity in each subsegment. The standard deviation among the subsegments (Std7) is regarded as the measure of parameter variability and shown with error bars in the plots in ch. 5.

Much of the information on turbulence presented in this study comes from the ultrasonic anemometer-thermometer mounted at the front of ACTOS and sampling three velocity components with 100 Hz frequency. Unfortunately, during the entire ACORES campaign, the lateral channel of the anemometer was affected by a substantial level of artificial fluctuations (up to 1 $\mathrm{m\,s^{-1}}$ in amplitude) attributed to instrumental issues. The origin of this problem is under investigation. It seems to appear for true air speed above about 12 $\mathrm{m\,s^{-1}}$ which makes it relevant for most of the flight time. Such behavior was not observed for the longitudinal and vertical components. Therefore, a simplified geometrical transformation was applied to the measured velocity vector so that a high-resolution retrieval of wind velocity is possible. In comparison with the standard transformation (Lenschow, 1986), the method included pitch rotation but neglected roll and yaw rotations to prevent the lateral channel from coupling with the others. The resulting vector (u, v, w) can be interpreted as the wind velocity in horizontal longitudinal, horizontal lateral and vertical direction, respectively, as long as the platform is not tilted left or right (roll angle is small). This condition was satisfied throughout most of the flight time, except for major turns. For calculating turbulence properties, the segments with the roll angle $<$0.1 rad were selected. The lateral wind component v cannot be used for turbulence analysis but the longitudinal u and vertical w are free from the disturbances.

The modification described is not necessary to obtain mean wind profiles (U, dd) because averaging and smoothing are applied anyway (see sec. 3.1.1). Hence, the high-frequency noise is irrelevant for the final result. Therefore, in the case of the wind profiles presented in ch. 4, simply the standard transformation for airborne platforms was applied.

Reynolds decomposition of the signals (c.f Stull, 1988)

$$x(t) = \langle x(t) \rangle + x'(t) \tag{3.8}$$

into large scale slowly varying $\langle x(t) \rangle$ and small scale fluctuations $x'(t)$ was realized with a simple symmetric running mean. The fluctuations $x'(t)$ were obtained by subtracting that mean from the original signal. Unless specified otherwise, the

chosen window was 50 s which corresponds to the distance of ∼1 km. Such length is enough to penetrate at least a few large turbulent eddies typical for the atmospheric boundary layer (Malinowski et al., 2013).

3.2.1 Turbulence Kinetic Energy and variances

The variances of turbulent fluctuations $\langle u'^2 \rangle$, $\langle w'^2 \rangle$, $\langle T'^2 \rangle$, $\langle q_v'^2 \rangle$ and the third moment of vertical velocity fluctuations $\langle w'^3 \rangle$ were obtained by taking average along LEGs. Because lateral wind fluctuations were not available, horizontal isotropy is assumed to approximate missing $\langle v'^2 \rangle$ with $\langle u'^2 \rangle$ in the TKE computation:

$$\mathrm{TKE} = \langle u'^2 \rangle + \frac{1}{2} \langle w'^2 \rangle . \tag{3.9}$$

It is worth remembering that variances and TKE usually represent mostly large scales because larger eddies in turbulence cascade are more energetic than smaller ones. Those large eddies are therefore responsible for the major part of the variance. In consequence, only LEGs were utilized to estimate TKE at several levels in the atmosphere due to the need for relatively long segments to sample the large eddies. PROFs are not suitable for this purpose as the conditions are not necessarily homogeneous in vertical and the steep slanted path of the helicopter covers a wide range of altitudes within the period of a single Reynolds averaging window.

The accuracy of the results is limited by the length of the LEGs. Based on the estimates obtained with the methods of Lenschow et al. (1994), in the boundary layer the variances are subject to the systematic sampling error of about 5 % and the random error of about 20 %. In the case of $\langle w'^3 \rangle$, those errors are accordingly larger (order of 10 % and 100 %, respectively, unless $\langle w'^3 \rangle$ almost vanishes). Importantly, in the plots in ch. 5, Std7 is provided because it can be as well estimated for other variables characterizing turbulence. The subsegment variability was found to be of the same order as the total sampling error, in most cases larger than it. See appendix A for the detailed treatment of sampling errors.

3.2.2 TKE production and heat fluxes

Turbulence kinetic energy can be generated by buoyancy and wind shear (ignoring advection and turbulent transport). The two respective terms of the TKE budget equation (Stull, 1988), buoyancy production/consumption and shear production,

were estimated for each LEG employing the method of eddy correlation:

$$B = \frac{g}{\langle \theta_v \rangle} \langle w'\theta_v' \rangle , \qquad S = - \langle w'u' \rangle \frac{\partial u}{\partial z}. \tag{3.10}$$

Here, only the longitudinal component of shear production could be calculated because the lateral wind fluctuations were not available (see sec. 3.2). It was attempted to overcome this limitation by estimating the missing correlation $\langle w'v' \rangle$ using the gradient transport theory (K-theory) or invoking the isotropy assumption for the Reynolds stress tensor. Unfortunately, both methods lead to an even stronger dependence of the outcome on horizontal wind derivatives which are subject to error related to in-flight wind measurement. Eventually, to avoid unacceptably large inaccuracies, in this study only the first component of the conventional shear production term is provided.

The correlations were computed along the LEGs. The derivatives were estimated from the PROFs covering the relevant altitude range. Inevitably, such an approach introduces some inaccuracy as the exact place and time of the derivative estimation is different than for the correlation estimation. Because the longitudinal–lateral–vertical coordinate system related to the platform changes its orientation with respect to the Earth as the platform turns, a simple differentiation of components might lead to spurious vertical gradients due to the changes in platform orientation. In order to avoid such an issue, first, the vector representing the vertical gradient of the horizontal wind velocity was calculated using u_e, v_e wind components in the Earth-fixed reference frame. Next, the projection of this vector onto the LEG-averaged transient longitudinal direction was used as $\frac{\partial u}{\partial z}$ in Eq. (3.10).

Besides, crucial for the properties and the evolution of stratocumulus clouds is the transport of heat and moisture across the boundary layer. This vertical transport is closely related to the degree of dynamic coupling in the STBL. To quantify the transport, sensible and latent heat fluxes were estimated according to Eq. (1.3).

The range of scales represented in the correlations is limited by the lowest spatial resolution of the two multiplied signals. The anemometer (u, w, θ_v) resolves the scales down to ∼0.5 m (where this limit stems from the path length and spectral transfer properties (Kaimal et al., 1968)), the thermometer (θ) down to ∼2 cm, the hygrometer (q_v) down to ∼1 m. As a result, $\langle w'\theta_v' \rangle$, $\langle w'u' \rangle$ and $\langle w'\theta' \rangle$ are resolved down to ∼0.5 m while $\langle w'q_v' \rangle$ down to ∼1 m. Those three instruments work satisfactorily also inside clouds of moderate liquid water content and droplet concentration, as the stratocumulus observed here (Cruette et al., 2000; Siebert and

Teichmann, 2000). In comparison with some other studies, the buoyancy estimation in the cloud does not include the contributions of liquid water flux $\langle w'q_l' \rangle$ and droplet sedimentation $\widetilde{w_T q_l}$ which are expected to be relatively small (considering moderate q_l) and of the opposite sign, therefore partly compensate.

Similarly to the variances, the accuracy of the fluxes obtained with eddy correlation is limited by the length of the LEGs. In the boundary layer, the systematic sampling error was estimated for about 5 % while the random error for about 50 % (Lenschow et al., 1994) unless the flux vanishes. The subsegment variability (marked with error bars in the plots in ch. 5) is in most cases larger than the total sampling error. See appendix A for the detailed treatment of sampling errors.

To complement airborne measurements at specified levels in the atmosphere, B, Q_s and Q_l at the surface were estimated with the Coupled Ocean-Atmosphere Response Experiment bulk algorithm version 3.0 (COARE 3.0) described in Fairall et al. (2003). Sea surface temperature was taken from the satellite multi-mission product provided by the Group for High Resolution Sea Surface Temperature (JPL MUR MEaSUREs, 2015). Other inputs to the algorithm were the measurements onboard ACTOS: from the lowest point of the PROFs or the mean values of the lowest LEG. Those two options result in similar outcomes. The former is used hereafter because PROFs offer the measurements which were performed closer to the surface. The input and output data for the COARE 3.0 algorithm are compared in Table 3.1.

Table 3.1: Parameterized surface fluxes estimated with the COARE 3.0 algorithm.

	Flight #5		**Flight #14**	
	PROF1	**LEG307**	**PROF1**	**LEG143**
z [m]	88	307	130	143
P [hPa]	1020.3	994.8	1007.9	1006.3
T [° C]	19.6	16.7	20.0	19.9
q_v [g kg^{-1}]	9.4	9.3	10.9	11.3
U [m s^{-1}]	6.3	5.3	7.0	5.7
F_{sol} [W m^{-2}]	1129	692	695	688
F_{ter} [W m^{-2}]	355	351	401	402
SST [° C]	21.75	21.75	22.05	22.05
STBL depth [m]	855	855	1045	1045
B [10^{-4}m^2 s^{-3}]	5.6	6.7	4.0	3.2
Q_s [W m^{-2}]	11.0	16.1	6.7	5.3
Q_l [W m^{-2}]	129.5	117.7	106.5	85.5

3.2.3 TKE dissipation rate

TKE dissipation rate quantifies the transfer of TKE down the energy cascade and its viscous conversion into heat. This quantity was calculated invoking a common assumption of homogeneous, isotropic, stationary turbulence which leads to a specific form of power spectra and structure functions (Kolmogorov, 1941). Nevertheless, the theoretical assumptions are often hardly satisfied in the atmosphere, e.g. considering complex stratification, and therefore ϵ estimation from moderate-resolution (not directly resolving dissipative scales) measurements is challenging (Siebert et al., 2006b; Jen-La Plante et al., 2016; Wacławczyk et al., 2017, 2020). To account for possible anisotropy, ϵ was derived separately for the longitudinal and vertical velocity fluctuations, following the methods of Siebert et al. (2006b). The quality of the estimations was characterized with additional parameters describing the deviation of experimental data from the theoretical dependencies.

3.2.3.1 Structure function method

Second order structure function (SFC) was calculated for the measured u' and w' according to the equation:

$$\mathcal{D}_u(r) = \left\langle |u'(x+r) - u'(x)|^2 \right\rangle \tag{3.11}$$

where r is the distance between data points (given by true air speed) and the average is taken over the positions x along the flight path. The SFC was then resampled, i.e. averaged inside the logarithmically equidistant bins covering the assumed inertial range $r \in [0.4, 40]$ m, with eight bins per decade (see Fig. 3.1). The resampling was applied in order to account for the density of data points increasing with scale in logarithmic coordinates.

Theory predicts that in the inertial range SFC has the form (Pope, 2000):

$$\mathcal{D}(r) = C^{sfc}(\epsilon r)^{\frac{2}{3}} \tag{3.12}$$

where C^{sfc} is a constant, experimentally determined to $C_u^{sfc} \approx 2.0$ for longitudinal and $C_w^{sfc} \approx 2.6$ for vertical velocity component. ϵ^{sfc} was calculated by the least-squares fit of this relationship to the resampled SFC. The resampling described above is crucial for the result as otherwise weights would need to be introduced in the fit procedure or the result of the fit would be almost solely dependent on the SFC values from the large scale tail of the assumed inertial range.

A second fit was performed according to:

$$\mathcal{D}(r) = C^* r^s \tag{3.13}$$

with two fitted parameters: a prefactor C^* and an exponent s corresponding to the slope in log-log plot. The exponent is used as a benchmark of the agreement of the SFC form with theory. Additionally, the Pearson correlation coefficient R^{sfc} was computed for the resampled points. It quantifies the linearity of the experimental SFC in log-log coordinates. Consequently, s and R^{sfc} assess to some extent the reliability of the derived ϵ.

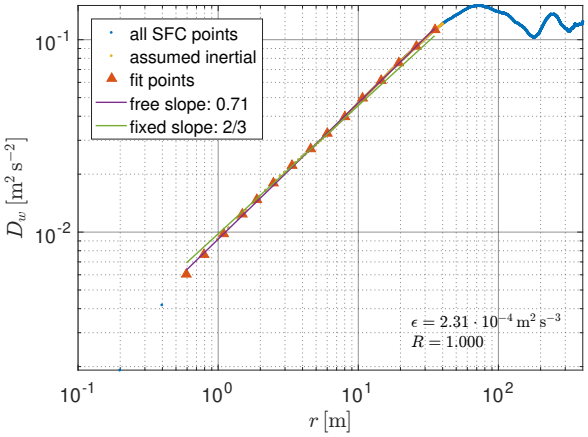

Figure 3.1: Example of ϵ derivation with the structure function method (flight #5, LEG307, vertical component). The computed SFC (Eq. (3.11), blue) is resampled in the assumed inertial range (yellow) to obtain logarithmically spaced points (triangles) which are used for two least squares fits: one with a free slope (Eq. (3.13), purple), one with a fixed theoretical slope (Eq. (3.12), green). From Nowak et al. (2021).

3.2.3.2 Power spectrum method

Power spectral density (PSD) of u' and w' was calculated with the Welch algorithm. The window was chosen as half the length of the segment. The windows overlap by half of their length, so, in turn, there are three individual PSDs averaged in the Welch scheme. The final PSD was then resampled in the assumed inertial range, analogously to the SFC (see Fig. 3.2).

Theory predicts the following PSD form in the inertial range (Pope, 2000):

$$\mathcal{P}(f) = C^{psd} \left(\frac{U_s}{2\pi}\right)^{\frac{2}{3}} \epsilon^{\frac{2}{3}} f^{-\frac{5}{3}} \tag{3.14}$$

where f is frequency and C^{psd} is a constant ($C_u^{psd} \approx 0.49$ for longitudinal and $C_w^{psd} \approx 0.65$ for vertical component). ϵ^{psd} was derived by fitting this relationship to the resampled PSD. A second fit was performed according to:

$$\mathcal{P}(f) = C^* f^p \tag{3.15}$$

where the fitted PSD exponent p corresponds to the slope in log-log plot. Together with the Pearson correlation coefficient for the resampled points R^{psd} it measures the agreement of the PSD form with theory and the reliability of the derived ϵ.

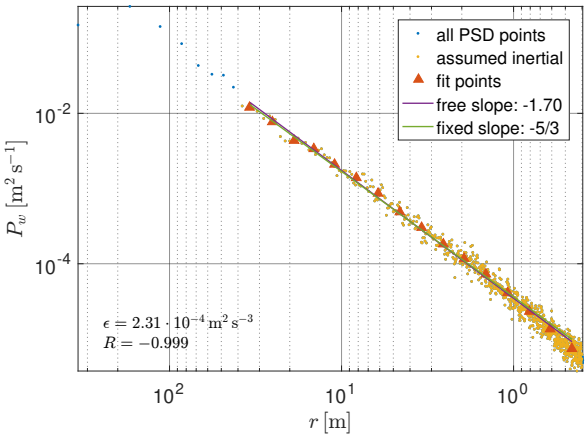

Figure 3.2: Example of ϵ derivation with the power spectrum method (flight #5, LEG307, vertical component). The computed PSD (blue) is resampled in the assumed inertial range (yellow) to obtain logarithmically spaced points (triangles) which are used for two least squares fits: one with a free slope (Eq. (3.15), purple), one with a fixed theoretical slope (Eq. (3.14), green). From Nowak et al. (2021).

3.2.3.3 Application of the methods

In the case of PROFs, the moving window of 2 s was applied to the timeseries u' and w'. In each window, ϵ was derived separately with the two methods for the two velocity components, together with the exponents and the correlation coefficients. Such a solution was verified to provide sufficiently good fits and constitutes the compromise between high final spatial resolution (short window desired) and adequate representation of SFC or PSD (long window desired). This approach follows earlier studies which determined the instantaneous dissipation rate utilizing the same type of data as here (Siebert et al., 2006b; Katzwinkel et al., 2012). Siebert et al. (2006b) have chosen the window of 1 s based on their sensitivity tests and the arguments

provided by Frehlich et al. (2004) and Muschinski et al. (2004). Because I derive not only ϵ but also slopes and correlations, I decided to increase the window to 2 s so that the linear fits cover a considerable portion of the inertial range and a sufficient number of logarithmically equidistant resampled points (see sec. 3.2.3.1).

In the case of LEGs, both methods were applied to the whole segments. Then, SFC and PSD were in practice averaged over a relatively long horizontal distance. This approach provides an estimate of 'mean' dissipation in contrast to 'local' values computed in short windows in the case of PROFs. The results on small-scale turbulence, including ϵ, s and p, should not be compared between PROFs and LEGs in a straightforward way. They are representative for small and large fluid volumes, respectively. Long horizontal segments may cover various air volumes differing in turbulence intensity and its properties, e.g. dissipation rate or inertial range scaling. According to the refined Kolmogorov hypothesis (Kolmogorov, 1962), due to intermittency of turbulence, ϵ distribution depends on the scale on which it is evaluated. This dependence inside clouds was investigated experimentally by Siebert et al. (2010). The SFC and PSD derived on a long segment are expected to follow their theoretical forms more accurately which is indeed the case (see sec. 5.3).

In this work, the calculation of ϵ with two different methods was motivated by the usual discrepancies and difficulties in estimating dissipation from airborne measurements (Wacławczyk et al., 2017, 2020). The results (sec. 5.3) demonstrate a good agreement between the methods as long as the relative variations with height are concerned. In terms of absolute values, ϵ^{psd} is usually systematically higher than ϵ^{sfc} (around a factor of 2). In general, the derived SFC resembles its theoretical form better than the PSD which is indicated by the fitted exponents and the correlation coefficients being closer to the theoretical values and to unity, respectively. This agrees with Siebert et al. (2006b) who found the SFC method to be more robust for ϵ estimation from velocity signals acquired onboard airborne platforms.

What is more, the longitudinal fluctuations appear to result in slightly higher dissipation than the vertical ones in most cases. However, the statistics of vertical velocity fluctuations are always in better agreement with theory than the longitudinal one as signaled by the fitted SFC and PSD exponents as well as the respective correlation coefficients.

In order to estimate the uncertainties of the results, I used the random errors of the fitted parameters (computed with a standard method from least-squares fit residuals). The random error of PROF-derived dissipation rate equals $\sim$50 % in the

boundary layer and ∼150 % in the FT. The error of the LEG-derived ϵ is ∼30 % for longitudinal component and ∼15 % for vertical component in the boundary layer while ∼150 % for both components in the FT. The random error of the fitted slopes is ∼0.04 for s and ∼0.16 for p in the case of PROFs while ∼0.02 in the case of both LEG-derived slopes. Notwithstanding, the given values represent the uncertainties due to the random errors of the fit only. The reliability of the derived dissipation rates can be also assessed by comparing the results of the two derivation methods, by comparing the fitted SFC and PSD slopes with their theoretical values or using the deviation of the computed correlation coefficients from unity.

3.2.4 Anisotropy

The assumption of isotropy, involved in the classical theory of Kolmogorov (1941), might be violated in many specific situations in the atmospheric boundary layer, e.g. under strong buoyancy and wind shear at stratocumulus top (Malinowski et al., 2013; Jen-La Plante et al., 2016; Akinlabi et al., 2019) or in the surface layer (Mahrt, 2014). To investigate the deviations from isotropy, I used anisotropy ratios A of two types, bulk and spectral, relating the w-derived parameters to the u-derived ones.

The bulk anisotropy ratios are defined as:

$$A_{var} = \sqrt{\frac{\langle w'^2 \rangle}{\langle u'^2 \rangle}}, \qquad A_\epsilon^{sfc} = \frac{\epsilon_w^{sfc}}{\epsilon_u^{sfc}}, \qquad A_\epsilon^{psd} = \frac{\epsilon_w^{psd}}{\epsilon_u^{psd}}. \tag{3.16}$$

Variance anisotropy ratio A_{var} relates mostly to larger eddies which have a dominant contribution to the total variance. Isotropy is indicated by the values close to 1, while A_{var} <1 or A_{var} >1 indicate anisotropic turbulence dominated by horizontal and vertical fluctuations, respectively. On the other hand, dissipation anisotropy ratios A_ϵ regard mostly the inertial range eddies because the ϵ derivation exploits the SFC or PSD scaling in the inertial range. Analogously, the values close to unity indicate isotropy.

A_{var} is the ratio of LEG-derived velocity variances. Both A_ϵ were computed for LEGs as well as for PROFs. In the case of PROFs, the profiles of ϵ_w and ϵ_u were divided one by another (point-by-point).

The spectral anisotropy is the scale-dependent ratio of the PSDs for vertical and longitudinal velocity:

$$A_\mathcal{P}(r) = \frac{\mathcal{P}_w(U_s/r)}{\mathcal{P}_u(U_s/r)} \tag{3.17}$$

where true air speed U_s is utilized to convert frequency into distance. A similar approach was exercised by Pedersen et al. (2018) who compared the modeled and measured anisotropy in the region of stratocumulus top. They used both horizontal velocity components, however, did not explicitly consider the distinction between longitudinal and lateral directions in their analysis. In the inertial range, the Kolmogorov theory predicts $A_{\mathcal{P}} = 4/3$. Such a value of the experimentally derived $A_{\mathcal{P}}$ should then indicate isotropy at a particular scale r. Importantly, it is not necessarily satisfied outside the inertial range, i.e. in the dissipative part of the spectrum or for the large scales above the integral length scale.

To obtain $A_{\mathcal{P}}$, the same resampling procedure as in sec. 3.2.3.2 was applied to the LEG-derived PSDs but across the whole available range of scales (not only the inertial). The relevant ratio was then calculated point-by-point. The data collected with the ultrasonic anemometer-thermometer are sufficient for the analysis of the spectral anisotropy in the inertial range as Siebert and Muschinski (2001) demonstrated that the spectra of velocity fluctuations measured with an earlier version of that instrument in a considerably turbulent environment follow closely the expected 5/3 power law, a flattening is observed only at frequencies larger than 30 Hz and the ratio of the transverse and longitudinal spectra equals 4/3.

3.2.5 Length scales

Turbulence energy cascade is often characterized by several length scales: integral scale L, Taylor microscale λ and Kolmogorov microscale η. The integral length scale corresponds to the energy-containing eddies which are involved in TKE generation. In the energy cascade, it marks the beginning of the inertial subrange where turbulent flow is considerably isotropic despite the anisotropy of large-scale factors.

The indefinite integral of the autocorrelation function $\mathcal{R}(r)$ involved in the formal definition of L (Pope, 2000) cannot be evaluated experimentally due to the limited available segment length. Instead, three pragmatic solutions are: integration to the first zero of the autocorrelation function (Lenschow, 1986), estimating the distance where the correlation declines by a factor of e or fitting the assumed function form to the power spectrum of the signal (Lenschow et al., 1994). The second method was chosen because it is robust enough to provide reasonable results in all the cases relevant for this study, in contrast to the others which might occasionally fail if $\mathcal{R}(r)$ only slowly decreases with distance.

For this reason, L was obtained by estimating the distance at which the autocorrelation

$$\mathcal{R}_u(r) = \frac{\langle u'(x+r)u'(x)\rangle}{\langle u'^2\rangle} \tag{3.18}$$

declines by a factor of e. The very same procedure was applied to longitudinal as well as vertical velocity to provide L_u and L_w, respectively. According to Pope (2000), under isotropic conditions $L_w = \frac{1}{2}L_u$. Such a proportion can then indicate isotropy in the relevant eddy scale.

At the Taylor microscale, viscosity starts to substantially affect the dynamics of turbulent eddies. The scales which are larger are believed not to be significantly influenced by viscous effects. λ is often reported in laboratory studies and numerical simulations of turbulent flows as the property which shall be independent of a generation mechanism. Under the assumption of isotropy, the Taylor microscale can be related to velocity variance and dissipation rate. Two length scales, longitudinal and vertical, were estimated according to the formulas:

$$\lambda_u = \sqrt{30\nu\frac{\langle u'^2\rangle}{\epsilon_u^{sfc}}}, \qquad \lambda_w = \sqrt{15\nu\frac{\langle w'^2\rangle}{\epsilon_w^{sfc}}} \tag{3.19}$$

where ν is air viscosity for which the temperature and pressure dependence is considered (Sutherland, 1893). In homogeneous isotropic turbulence $\lambda_w = \frac{1}{\sqrt{2}}\lambda_u$ (Pope, 2000).

The Kolmogorov microscale corresponds to the smallest eddies where TKE is dissipated into heat by viscosity. Following dimensional arguments of the famous similarity hypothesis (Kolmogorov, 1941), it equals:

$$\eta_u = \left(\frac{\nu^3}{\epsilon_u^{sfc}}\right)^{\frac{1}{4}}. \tag{3.20}$$

This microscale was calculated separately for longitudinal (η_u) and vertical (η_w) direction with the same formula. Provided local small-scale isotropy, they should be equal. Because the definition of η involves only small scale quantities, it could be obtained for LEGs as well as for PROFs. For convenience, in λ and η derivation, only ϵ^{sfc} was used because the SFC proved to resemble its theoretical form better than the PSD (see sec. 3.2.3.3 and 5.3).

3.3 Aerosol properties

The degree of coupling in an STBL can influence the distribution of aerosol particles. Typically, the particles are small enough to neglect their sedimentation within the timescales relevant for the boundary layer circulation. However, the effects of circulation and mixing may alter between coupled and decoupled conditions. Their impact on aerosols properties was examined by comparing N_p, N_{CCN} and PNSD between the two cases. The processing of aerosol particles by various chemical and physical mechanisms (photochemistry, nucleation, hygroscopic growth, etc.) is not considered in this study.

The concentrations, N_p and N_{CCN}, were sampled by the CPC and the miniCCNC, respectively, with the rate of 1 s which ensures satisfactory spatial resolution. The size distribution was provided by the combination of the SMPS and the OPC. The SMPS system developed at TROPOS is optimized with respect to weight and power consumption for the operation onboard ACTOS. See Wehner et al. (2010) for the details about its construction. The instrument requires 120 s to complete a scan covering the size range 6-250 nm. The scans are performed in an alternate manner: from small to large D_p (up-scan) and in the opposite direction (down-scan). Larger particles (250 nm - 2.5 µm) are sized and counted by the OPC which provides results every 1 s. Wide-range composite PNSDs are then calculated in 2 min long segments by combining the SMPS-derived part with the suitably averaged OPC-derived part according to the method given by Pfeifer et al. (2014). Prior to the campaign, the SMPS and the OPC have been compared with a well-characterized reference instrument (Twin Differential Mobility Particle Sizer) and showed a good agreement within the measurement uncertainties.

The PNSD scanning procedure has essential consequences for the interpretation of the results. Within the time corresponding to one scan, substantial horizontal and vertical distance can be flown by the platform. Needless to say, there might be local changes in aerosol properties inside the penetrated volume. What is more, one diameter bin is measured at a time, so each particular point in the SMPS part of the PNSD represents a slightly different location. Being aware of the limitations, in the following, I indicate the direction of the scan (up or down) and the spatial domain corresponding to the presented PNSD. In the case of PROFs, individual PNSD scans are shown. In the case of LEGs, a few scans executed within the time of the segment are averaged assuming horizontal homogeneity.

A common inlet at the front of ACTOS (c.f. Fig. 2.3) is used for the CPC, SMPS and OPC. The sample flow is directed through a diffusion dryer to provide dry measurement conditions ($<$ 50 % relative humidity) and further divided by a flow splitter into the lines leading to the instruments. The miniCCNC was served by another inlet and a dryer located at the side of ACTOS. All the measurements were corrected for the variations in flow volume due to pressure changes and for the losses within the inlet line. The results were converted for the standard temperature (288 K) and pressure (1013.15 hPa). The calibrations, corrections and data post-processing of the aerosol measurements were performed by B. Wehner, S. Henning and J. Luckerath.

Chapter 4

Stratification

This chapter describes the stratification of the two STBLs, coupled and decoupled, in terms of meteorological and thermodynamic properties derived from the airborne measurements performed with ACTOS and selected ground-based routine observations performed at the ARM ENA site. The content of sections 4.1, 4.2.1, 4.2.2, 4.3.1, 4.3.2 comes in large part from Nowak et al. (2021). The content of sections 4.2.3, 4.2.4, 4.3.3 and 4.3.4 has not been published before.

4.1 Quantitative judgement of the degree of coupling

The parameters characterizing the internal coupling of the boundary layer (see sec. 3.1.2) were estimated using PROF1 of flight #5 and PROF5 of flight #14. According to the criteria of Jones et al. (2011), it is evident that flight #5 ($\Delta\theta_l = -0.51$°C, $\Delta q_t = 0.13$ g kg^{-1}, $\Delta z = -72$ m) was performed in a coupled STBL while flight #14 ($\Delta\theta_l = 1.19$°C, $\Delta q_t = 0.90$ g kg^{-1}, $\Delta z = 216$ m) in a decoupled STBL. The negative values of $\Delta\theta_l$ and Δz suggest instability but they might be also attributed to the horizontal inhomogeneities of stratocumulus structure (see sec. 2.5.1) in combination with the slanted flight path.

Consistently, the parameters of Wood and Bretherton (2004) are smaller for flight #5 ($\alpha_\theta = -0.12$, $\alpha_q = 0.04$) than for flight #14 ($\alpha_\theta = 0.26$, $\alpha_q = 0.26$). The stability parameter of Yin and Albrecht (2000) is plotted in panel (d) of Figs. 4.1 and 4.4. It varies significantly with height and the critical value is occasionally exceeded in both flights. This method was probably optimized for radiosoundings in a different climate regime and does not seem robust in the case of ACTOS data.

In both studied cases, the CTEI parameter exceeds the critical value ($\kappa = 0.71$ for flight #5 and $\kappa = 0.34$ for #14), indicating the possibility of buoyancy reversal resulting from mixing at the cloud top. This buoyancy reversal is of potentially higher importance at the top of the coupled STBL. The decoupling measures, together with the conditions at the relevant levels in the boundary layer, are summarized in Table 4.1 below.

Table 4.1: Parameters characterizing the coupling of the boundary layer and the cloud top entrainment instability.

Parameter	**Flight #5**	**Flight #14**
θ_l^{bot} [°C]	17.96	18.85
θ_l^{top} [°C]	17.45	20.04
θ_l^{-} [°C]	17.35	20.47
θ_l^{+} [°C]	22.86	25.09
$\Delta\theta_l$ [°C]	-0.51	1.19
α_θ	-0.12	0.26
q_t^{bot} [g kg^{-1}]	9.56	11.61
q_t^{top} [g kg^{-1}]	9.43	10.71
q_t^{-} [g kg^{-1}]	9.25	10.63
q_t^{+} [g kg^{-1}]	1.73	7.84
Δq_t [g kg^{-1}]	0.13	0.90
α_q	0.04	0.26
LCL^{bot} [m]	787	649
CB [m]	715	865
κ	0.71	0.34

4.2 Coupled STBL

4.2.1 Vertical structure

The profiles of thermodynamic and stability variables in flight #5 exhibit a well-mixed STBL (Fig. 4.1). Temperature falls with height with near-constant lapse rate inside the boundary layer, followed by a sharp inversion at the top. Liquid water potential temperature is almost constant from close to the surface up to the stratocumulus top, where it features the increase of ∼5 K. Total water mass fraction behaves analogously, with the decrease of ∼7 g kg^{-1} above the cloud top. Interestingly, very dry air is located at the top of the temperature inversion. It is further capped by the layer of considerably higher q_v, however much lower than

inside the boundary layer. Liquid water mass fraction in the cloud is moderate and suggests a non-trivial cloud structure. There were cloud clearings penetrated as ACTOS moved along the slanted path, evident in the high rate records of q_l (not shown here). Wind velocity fluctuates in the boundary layer within $\pm 1\ \mathrm{m\,s^{-1}}$ around the mean $\sim 5\ \mathrm{m\,s^{-1}}$. Wind shear across the cloud top and the inversion can be noticed. Wind direction is from NNW throughout the sampled height.

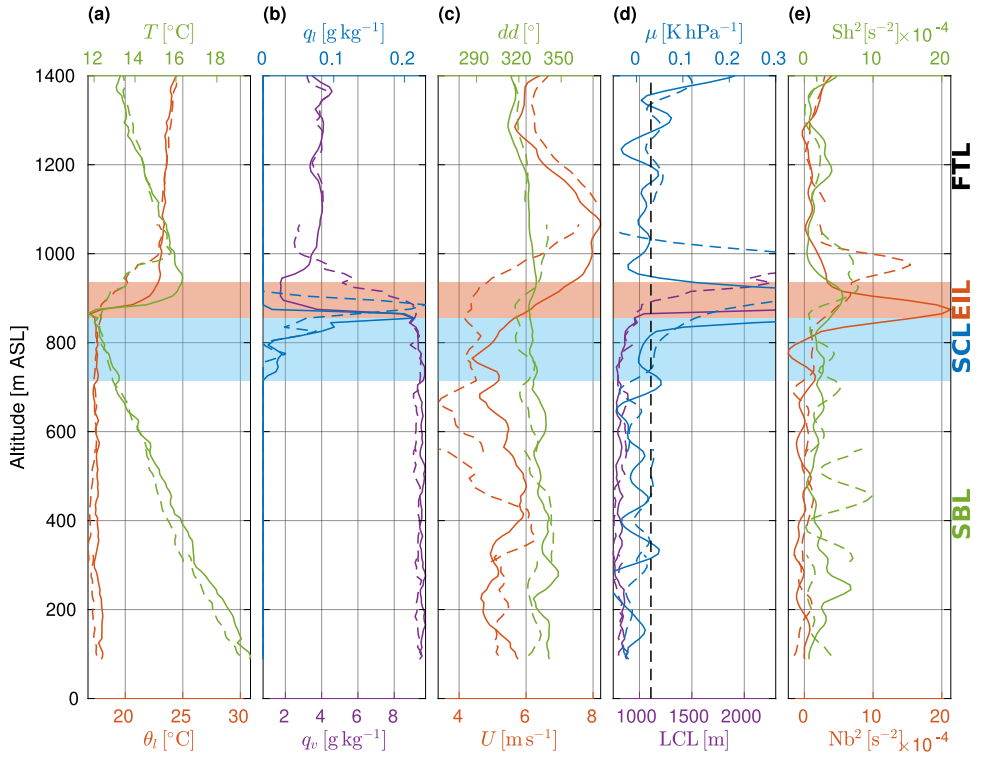

Figure 4.1: Vertical structure of the coupled STBL: (a) temperature T and liquid water potential temperature θ_l, (b) liquid water mass fraction q_l and specific humidity q_v, (c) wind speed U and direction dd, (d) lifting condensation level LCL and stability parameter μ with its critical level (dashed black line), (e) squared Brunt-Väisälä frequency Nb^2 and wind shear rate Sh^2. Line styles correspond to the specific profiles (c.f. Fig. 2.7). Color shadings denote the sublayers: entrainment interface layer (red) and stratocumulus layer (blue). From Nowak et al. (2021).

Significant differences can be observed between the PROFs in wind speed and the position of the inversion. Subsequent PROFs were not performed at the same time and location, so certain variability is expected. Airborne sampling features inevitable randomness due to probing specific structures (eddies, updrafts, cloud holes, etc.), thus slanted profiles do not represent mean conditions accurately.

LCL stays roughly equal from the lowest level up to the cloud base. Interestingly, at low levels, it is slightly higher than the actual cloud base which might be again related to the horizontal inhomogeneities in the cloud structure. Brunt-Väisälä frequency indicates weak static instability in the boundary layer, consistently with the findings of Ghate et al. (2015), see sec. 1.4.3. The instability is somewhat stronger inside the cloud than below (see exact value of Nb^2 in Table 4.2). On the other hand, the capping inversion features very strong stability. Wind shear is more variable which can be attributed to sampling issues mentioned above.

4.2.2 Partition into sublayers

Based on the profiles of θ_l, q_l and q_v, the following sublayers were distinguished manually: the EIL including the temperature inversion and the very top of the cloud, the SCL containing the cloud, the SBL ranging from the cloud base down to the surface, and the sublayer representing free tropospheric conditions (FTL, not necessarily adjacent to the EIL top). For reference, the EIL and SCL are marked with red and blue shading, respectively, in Fig. 4.1 and following. The heights and average properties inside the sublayers are listed in Table 4.2. The deepest profile (PROF1, solid line), was used for sublayer distinction because the specific heights may vary between PROFs. The individual penetrations of the sublayer boundaries during the other flight segments (PROFs and dolphin porpoises) are indicated in Fig. 2.7. Suitable normalization and averaging between individual PROFs, as proposed by Ghate et al. (2015), is not possible in this study because the other PROFs are not deep enough.

4.2.3 Temporal evolution of stratification

The profiles provided by the two radiosoundings on 8 July 2017, launched about three hours before the helicopter take-off and about one hour after the landing, are presented in Fig. 4.2. Consistently with the ACTOS measurements (Fig. 4.1), they show a relatively well-mixed boundary layer.

Above a very warm surface layer over land, temperature decreases with height with near-constant lapse rate. In both soundings, there is a pronounced temperature inversion at a similar height range as observed during the flight. A similar difference in the inversion height, of about 100 m, as between the soundings was also evident between the individual PROFs during the flight. Therefore, it can be

Table 4.2: Average meteorological conditions and stability parameters inside the specified sublayers of the atmosphere during flight #5 derived from PROF1. Temperature lapse rate Γ, squared Brunt-Väisälä frequency Nb^2 and wind shear rate Sh^2 were obtained by calculating the derivatives over the depth of each sublayer. Other parameters were simply averaged over relevant heights.

Parameter	**SBL**	**SCL**	**EIL**	**FTL**
Height [m]	0-715	715-855	855-935	1005-1385
T [° C]	16.24	12.59	14.53	14.41
θ_l [° C]	17.62	17.52	20.59	23.54
Γ [K km^{-1}]	-10.9	-10.1	73.9	-7.2
q_t [g kg^{-1}]	9.53	9.43	3.19	3.89
U [m s^{-1}]	5.3	5.0	6.5	6.8
dd [°]	337	330	329	323
LCL [m]	814	845	3363	3130
Nb^2 [10^{-4}s^{-2}]	-0.4	-0.6	15.4	0.7
Sh^2 [10^{-4}s^{-2}]	0.0	0.3	5.1	1.0

attributed to the combination of horizontal inhomogeneities and horizontal advection. The measured temperature gradient is not as sharp as in Fig. 4.1 due to the limited resolution of the radiosonde thermometer and the considerable ascent rate of the balloon. Potential temperature is almost constant with height from above the surface layer up to the boundary layer top where it features the increase of ∼5 K. Importantly, θ does not account for liquid water content, which is not measured in radiosounding. Therefore, θ is not conserved in moist processes. Specific humidity indicates that the surface layer near the airport is quite humid, probably due to the proximity of the ocean and the northerly winds. Higher up, the balloon rises over the land of the island, which shall explain the slight decrease of q_v. Then, the sonde leaves the layer characterized by the land influence and reports near-constant q_v up to the top of the boundary layer. The decrease across the inversion is ∼5 g kg^{-1}. The dry layer adjacent to the inversion top is likely unresolved by the hygrometer of the radiosonde (c.f. Fig. 4.1, panel (b)). The measurements of relative humidity suggest that the cloud penetrated in the first sounding was very thin while there was no cloud penetrated in the second sounding. This might relate to the substantial inhomogeneity of the cloud structure (see Fig. 2.6 in sec. 2.5.1). On the other hand, the minor increase of θ and minor decrease of q_v above 600 m in the first sounding might be related to a weak decoupling in the cloud clearing region.

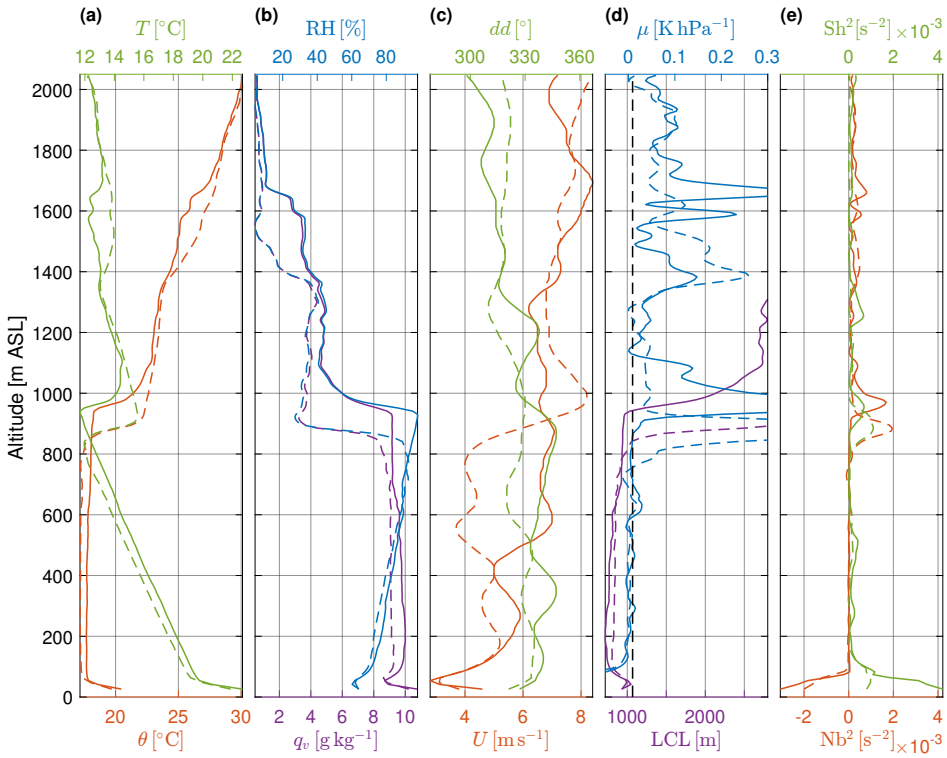

Figure 4.2: Radiosoundings launched at ARM ENA site on 8 July 2017, before (at 11:31, solid) and after (at 17:30, dashed) flight #5: (a) temperature T and potential temperature θ, (b) relative humidity (RH) and specific humidity q_v, (c) wind speed U and direction dd, (d) lifting condensation level LCL and stability parameter μ with its critical level (dashed black line), (e) squared Brunt-Väisälä frequency Nb^2 and wind shear rate Sh^2.

The wind blows consistently from the NNW direction in the boundary layer. The surface layer over land is characterized by significant wind shear. In the sounding launched after the flight, a similar gradient in wind speed at the STBL top was observed as in the ACTOS profiles. However, the second sounding exhibits the gradient at around 500 m in the middle of the boundary layer. One may speculate it is related to the influence of the island topography in combination with the path of the sonde. Indeed, the highest hills on Graciosa reach almost 400 m a.s.l.

LCL slowly increases with height throughout the boundary layer suggesting it is not ideally well-mixed. This increase is most pronounced in the first sounding at about 600-700 m. A local maximum of μ can be found at the same level. Nb^2 is strongly negative in the surface layer, indicating considerable instability. It is nearly zero in the middle boundary layer, indicating neutral stability, and positive

in the inversion layer which points out stable stratification. Sh^2 is large close to the surface and in the inversion layer, where significant gradients of U were identified. In general, both soundings can be considered consistent with the ACTOS profiles performed in flight #5 which implies the stratification of the atmosphere in the study area did not undergo dramatic changes over the timescale of several hours.

4.2.4 Temporal evolution of cloud structure

The daily evolution of the ceilometer backscatter profiles is shown in Fig. 4.3. After several hours of precipitation at night, a rain-free stratocumulus-topped boundary layer appeared over the ARM ENA site. The CB was gradually increasing over the day which implies the increase of LCL. This was realized mostly by drying rather than warming because both T and q_v decreased a bit from the first to the second radiosounding (Fig. 4.2). Most likely, the height of the STBL top was also increasing with time. Having measurements at one point only, it is difficult to discern the contributions of advection and entrainment to the growth of the boundary layer.

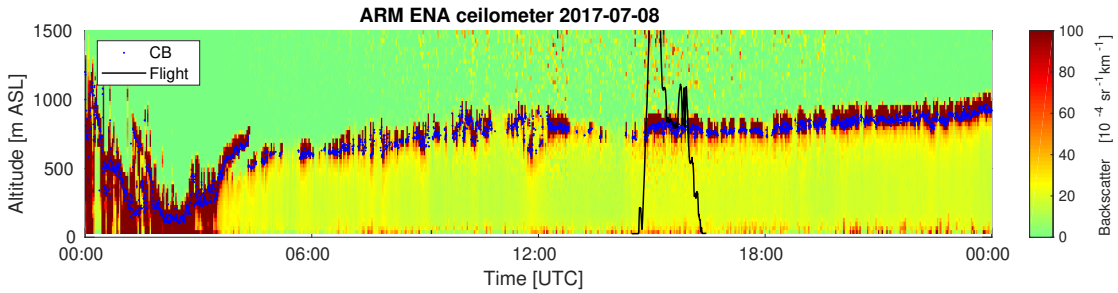

Figure 4.3: Profiles of the backscatter coefficient measured by the ceilometer at the ARM ENA site throughout 8 July 2017. Blue dots denote the estimation of cloud base height derived with the default ceilometer algorithm. For reference, black solid line marks the altitude profile in flight #5.

The cloud structure was scattered, in agreement with the satellite image (Fig. 2.6), in particular in the morning and early afternoon. β seems to be slightly larger below the clouds in comparison to the clear sky areas, in particular under the somewhat lowered cloud bases. Possibly, surface-generated aerosols can be lifted up by the boundary layer updrafts which also contribute to cloud formation and usually exhibit lower LCLs in relation to the downdrafts originating at the cloud top.

4.3 Decoupled STBL

4.3.1 Vertical structure

The profiles in flight #14 exhibit a decoupled STBL (Fig. 4.4). Liquid water potential temperature gradually rises with height whereas specific humidity decreases step-wise. Despite the distinct q_v gradient in the middle of the boundary layer, its value in the lowest part and in the subcloud section is relatively stable. This suggests that both the upper and the lower STBL portions are internally mixed. The FT is quite humid, with q_v larger than for flight #5. The difference in θ_l at the stratocumulus top is ∼5 K while in q_t only ∼3 g kg^{-1}. The stratocumulus is thicker and more abundant in liquid water than in the previous case. Wind velocity varies ±1 m s^{-1} around the mean ∼6 m s^{-1}. Wind direction is predominantly from the NW. There is significant wind shear across the inversion, with the difference in U reaching ∼4 m s^{-1}.

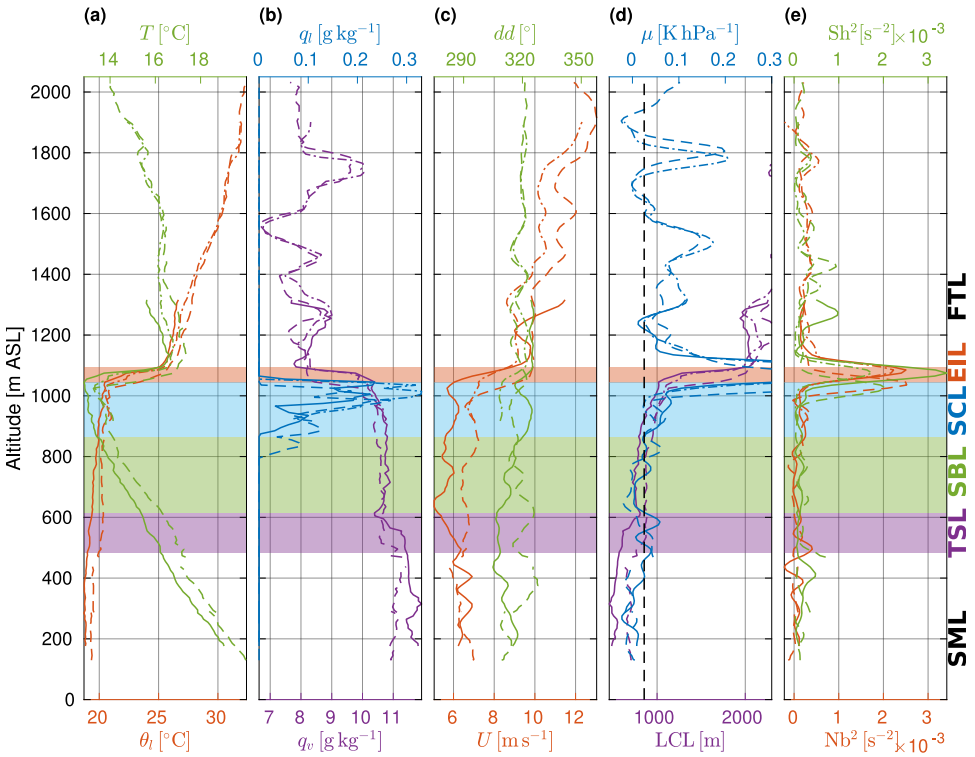

Figure 4.4: Vertical structure of the decoupled STBL (flight #14). Notation as in Fig. 4.1. Line styles are consistent with Fig. 2.10. Color shadings denote the sublayers: entrainment interface layer (red), stratocumulus layer (blue), subcloud layer (green), transition layer (purple). From Nowak et al. (2021).

LCL replicates the gradients of q_v in the middle of the boundary layer. It corresponds to the actual CB only in the section right below the cloud which is a signature of decoupling. Brunt-Väisälä frequency indicates weak static stability throughout most of the profile, including the cloud, consistently with the observations of Ghate et al. (2015), see sec. 1.4.3. The peak in the inversion layer coincides well with the maximum of Sh^2. The parameter μ shows a local maximum, exceeding the critical value, at about 580 m. However, it is not very pronounced and not the only one, owing to large variations with height.

4.3.2 Partition into sublayers

Similarly to flight #5, the following sublayers were distinguished: the FTL, the EIL, the SCL, and the SBL extending from the cloud base down to the level where LCL is no longer in agreement with the observed CB. In addition, two more sublayers typical for decoupled conditions were introduced: the TSL containing the major gradients in specific humidity and wind speed, and the SML extending from the surface up to the bend in θ_l profile (where it begins to rise with height, c.f. Fig. 4.4, panel (a)). A somewhat arbitrary boundary of 385 m was chosen to represent the top of the SML which is directly influenced by surface processes. For reference, the EIL, SCL, SBL and TSL are marked with red, blue, green and purple shading, respectively, in Fig. 4.4 and following. The heights and average properties inside the sublayers are listed in Table 4.3. Here, PROF5 was used for the sublayer identification because it covers most of the STBL depth. The individual penetrations of the sublayer boundaries during other flight segments are indicated in Fig. 2.10.

4.3.3 Temporal evolution of stratification

The profiles provided by the two radiosoundings on 18 July 2017, launched about four hours before the helicopter take-off and shortly after the landing, respectively, are presented in Fig. 4.5. The first one features a deep cloud layer. The second one exhibits a decoupled STBL, in agreement with ACTOS measurements (Fig. 4.4).

Likewise the coupled case, there is a surface layer evident in the profiles. It is related to the direct influence of land and manifests in high temperature and humidity, significant wind shear and static instability. In the first sounding, Γ changes from dry to moist at the CB of ∼600 m. The cloud base is indicated by the maximum possible relative humidity reached at this point. Here, θ begins to steadily

Table 4.3: Average meteorological conditions and stability parameters inside the specified sublayers of the atmosphere during flight #14 derived from PROF5. Notation as in Table 4.2.

Parameter	**SML**	**TSL**	**SBL**	**SCL**	**EIL**	**FTL**
Height [m]	0-385	485-615	615-865	865-1045	1045-1095	1150-1400
T [° C]	18.06	15.79	14.36	13.10	13.90	16.05
θ_l [° C]	18.81	19.20	19.61	20.16	22.37	26.29
Γ [K km^{-1}]	-10.1	-7.1	-7.4	-2.9	84.6	-5.2
q_t [g kg^{-1}]	11.65	11.08	10.75	10.68	9.65	8.48
U [m s^{-1}]	6.5	5.8	5.5	6.0	7.3	9.9
dd [°]	314	308	314	322	322	325
LCL [m]	508	658	769	905	1328	2040
Nb^2 [10^{-4}s^{-2}]	0.5	0.9	0.1	1.5	28.0	1.5
Sh^2 [10^{-4}s^{-2}]	0.2	0.8	0.1	0.1	45.6	1.5

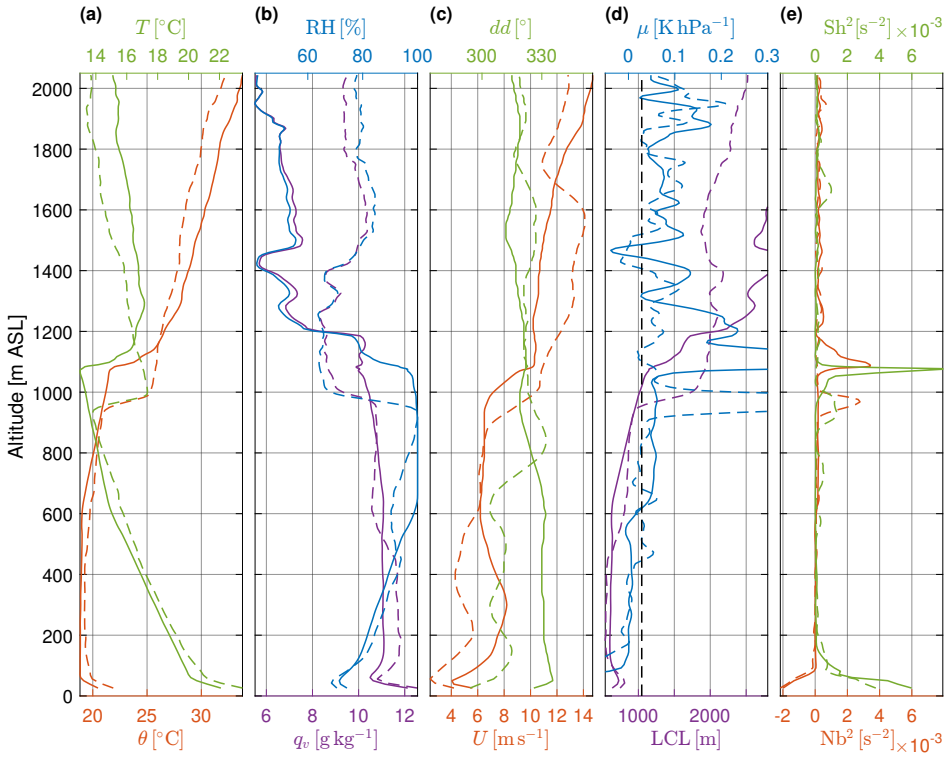

Figure 4.5: Radiosoundings launched at ARM ENA site on 18 July 2017, before (at 11:38, solid) and after (at 17:30, dashed) flight #14. Notation as in Fig. 4.2.

rise because of the latent heat released in condensation which is not accounted for in the definition of 'dry' potential temperature, in contrast to θ_l (c.f. Eq. (3.1)). Simultaneously, q_v slowly decreases as condensation transfers water vapor into liquid droplets. The temperature inversion is located at ∼1100 m and θ increases by ∼5 K there. Interestingly, the decrease of q_v of only ∼3 g kg^{-1} occurs 100 m higher than the inversion.

In the second sounding, at about 450-500 m, Γ changes, θ starts to increase with height and q_v decreases. Those properties indicate STBL decoupling, which stays in a good agreement with the ACTOS measurements. The cloud is relatively thin. The temperature inversion is located at ∼950 m with similar differences of θ and q_v as in the previous sounding and the profiles of flight #14. The gradient of specific humidity can be identified at a similar level as in Fig. 4.4 but it is not as pronounced due to the limited resolution of the radiosonde hygrometer and the considerable climb rate.

Wind speed in the boundary layer is ∼6 m s^{-1} for both soundings. There is some variability in the lower part, possibly due to the effect of island topography, and significant shear across the inversion. Interestingly, wind direction in the lower atmosphere changes from the NNW to the NW between the soundings. Recalling the surface pressure chart for this day (Fig. 2.8), it might be related to the passage of a weak front in the afternoon.

LCL replicates the gradient of q_v in the middle of the STBL in the second sounding which confirms the intuition for decoupling and complies with the ACTOS measurements. The stability parameter μ has two local maxima around that level. Brunt-Väisälä frequency and shear rate behave as expected, with significant deviations from zero only in the surface layer over land and in the EIL.

4.3.4 Temporal evolution of cloud structure

The cloud cover was solid throughout most of the day until the evening (Fig. 4.6), consistently with the satellite image (Fig. 2.9). Rain often fell onto the observation site which can be related to deeper stratocumulus than in the coupled case. Intermittent precipitation periods might be connected to the cellular mesoscale structure implied by the satellite image.

In the afternoon, scattered cumulus clouds emerged over the site below the stratocumulus base (c.f. sec. 7.5). Interestingly, the backscatter coefficient below the

stratocumulus decreases from the early morning to the late afternoon, possibly due to the scavenging of aerosol particles and the decoupling of the circulation which disturbs the transport from the surface. The surface-generated particles are likely lifted up in the cumulus updrafts which would explain enhanced β below the cumuli. In the evening, another airmass containing only scattered clouds was advected.

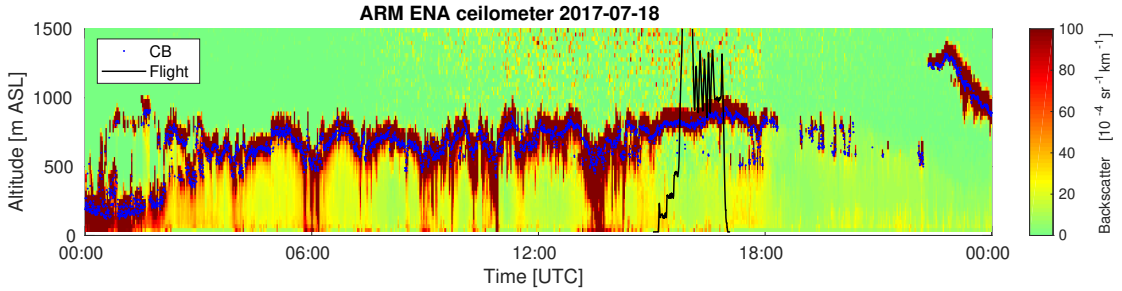

Figure 4.6: Profiles of the backscatter coefficient measured by the ceilometer at the ARM ENA site throughout 18 July 2017. Blue dots denote the estimated cloud base height, black line marks the altitude profile in flight #14.

Chapter 5

Turbulence

The properties of turbulence in the coupled and decoupled STBLs are documented in a series of plots. Depending on flight segment type, they are illustrated with continuous profiles (PROFs) and/or dots with error bars (LEGs). For reference, the sublayers introduced in ch. 4 are indicated in the figures with color shadings. The mean PROF-derived values inside the sublayers are listed in Tables 5.1 and 5.2.

The content of this chapter corresponds to sec. 5 of Nowak et al. (2021). Here, the material is expanded with some additional details.

5.1 Turbulence Kinetic Energy and variances

Figure 5.1 presents the variances of vertical and longitudinal velocity fluctuations, TKE, the third moment of vertical velocity, the variances of temperature and specific humidity in the LEGs of flights #5 and #14.

Generally, the TKE inside the coupled STBL decreases with height from the middle of the SBL up to the cloud top. Despite slightly unstable stratification, the contribution from the horizontal velocity variance is dominant over the vertical one. The latter reaches its minimum value below the cloud, where B is close to zero (c.f. Fig. 5.2i in sec. 5.2).

The estimated TKE is also large in the FT above the temperature inversion. This is rather an artifact due to the likely presence of gravity waves favored under stable conditions. It is implied by the power spectra of w, u, q_v, θ_v (not shown) which indicate that most of the variance can be attributed to a peak at the wavelength of about 450 m. A similar observation was made for the cospectra of wu, wq_v and $w\theta_v$ (not shown) which indicate that most of the covariance can be attributed to the

same range of wavelengths. Recall that LEG1079 was flown very close to the EIL and the cloud top which often features undulated interface.

The third moment of vertical velocity is positive in the lowest LEG307, suggesting strong but localized updrafts and weak but widespread downdrafts. Higher up, it is close to zero. These results ought to be interpreted with caution because the estimation of $\langle w'^3 \rangle$ can be subject to errors due to insufficient statistics related to the small chance of penetrating infrequent but intense events (Lenschow et al., 1994; Kopec et al., 2016). See appendix A for details.

The fluctuations of temperature and humidity can be significant wherever there are spatial gradients of those quantities or in the presence of sources or sinks of heat and moisture. Such conditions occur close to the cloud top, where radiative cooling is the sink of heat and the mixing between the air volumes of considerably contrasting properties occurs. Indeed, the measured variances are highest in the cloud segment and decrease downward into the boundary layer where T and q_v are locally more uniform.

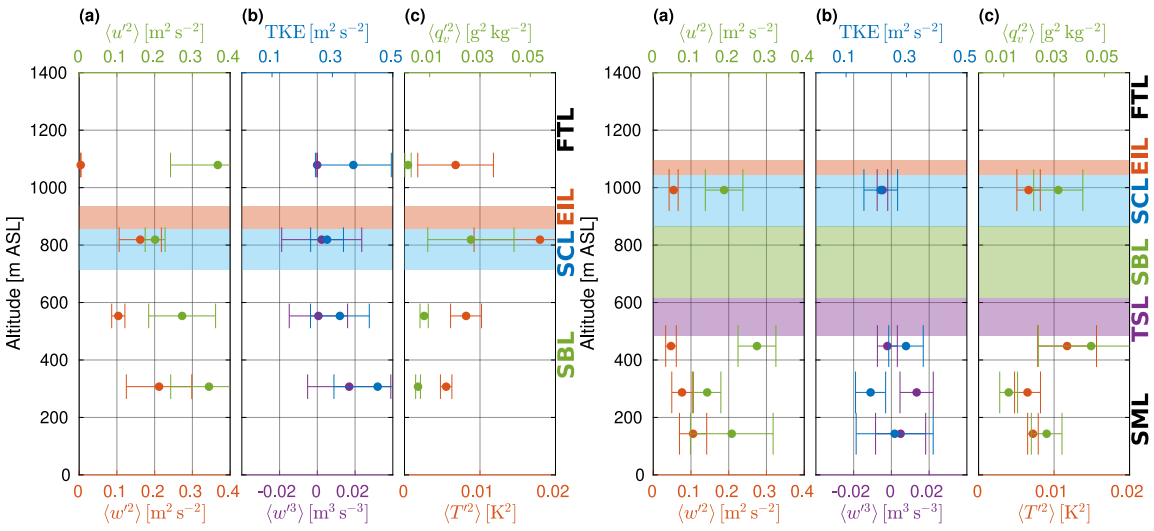

(i) Coupled STBL (flight #5). (ii) Decoupled STBL (flight #14)

Figure 5.1: Statistics of turbulent fluctuations: (a) variance of horizontal $\langle u'^2 \rangle$ and vertical $\langle w'^2 \rangle$ velocity, (b) turbulence kinetic energy TKE and third moment of vertical velocity $\langle w'^3 \rangle$, (c) variance of temperature $\langle T'^2 \rangle$ and specific humidity $\langle q_v'^2 \rangle$. From Nowak et al. (2021).

In the decoupled STBL, the TKE level is in general lower than in the coupled case. The profiles of the velocity variances across the SML resemble a typical mixed

layer with shear, i.e. high TKE at the bottom and the top which is realized mostly by the contribution of horizontal velocity variance (e.g. Stull, 1988, ch. 4). The prevalence of horizontal in comparison to the vertical velocity variance is particularly visible for LEG448, close to the transition, where $\langle w'^2 \rangle$ reaches its minimum. Similarly to the TKE, $\langle T'^2 \rangle$ and $\langle q_v'^2 \rangle$ exhibit maximum at this level. Temperature and specific humidity can be considered passive scalars which undergo mixing. The increased variances are caused by gradient production rather than by any diabatic sources (see Stull, 1988, Eqs. (4.3.2) and (4.3.3) therein).

The skewness of the vertical velocity is slightly positive in the SML with the maximum in LEG287 At the transition and in the cloud, it is close to zero with a tendency towards negative values. This suggests the dominant role of updrafts in the SML and downdrafts in the SCL.

Altogether, the results can be interpreted as a signature of decoupling between the circulations in the lower and upper parts of the boundary layer, as downdrafts originated at the cloud top and updrafts originated at the surface seem to slow down and diverge horizontally at the transition level.

5.2 TKE production and turbulent fluxes

The buoyant production of TKE is expected to be significant inside the cloud and close to the surface while the shear production is expected to be significant at the bottom and the top of the boundary layer (Markowski and Richardson, 2010). Such a picture is in general agreement with the results for flight #5. In the coupled STBL observed there (Fig. 5.2i), B is maximum in the LEG flown inside the cloud ($8.0{\cdot}10^{-4}$ m^2 s^{-3}), drops to nearly zero below the cloud and increases towards the surface, reaching $5.6{\cdot}10^{-4}$ m^2 s^{-3} (estimated with the COARE 3.0 algorithm). S is more uniform in the boundary layer, yet subject to substantial variability among the subsegments.

Sensible heat flux reaches the maximum of almost 40 W m^{-2} close to the cloud top, stays small and positive in the middle of the boundary layer with the surface value of around $Q_s = 11$ W m^{-2} (according to the COARE 3.0 algorithm).

Latent heat flux follows a nearly linear decrease from $Q_l = 130$ W m^{-2} at the ocean surface, which is the source of moisture due to evaporation, to roughly zero below the cloud. At low levels in the atmosphere (at the surface and in LEG307) the contribution of moisture transport to buoyancy is of the same order as the

contribution of heat transport, c.f. Eq. (1.6). In the cloud top region Q_l exceeds 100 W m^{-2} (subject to very large variability).

The reason for the massive upward transport of both the latent and sensible heat in the cloud might be the radiative and evaporative cooling at the stratocumulus top. LEG819 was performed close to the cloud top but neither exactly at the interface nor inside the EIL, so the fluxes do not represent the entrainment of warm and dry air from the FT but rather the air volumes which were cooled in the cloud top region and descend through the cloud (Gerber et al., 2016). The isobaric diabatic cooling at the cloud top leads to the reduction of potential temperature and the resulting negative buoyancy induces sinking motion. In effect, negative w' correlates with negative θ' resulting in positive heat flux. If the temperature is reduced, then also q_v of the initially saturated volume should decline because some part of the water vapor needs to condensate. Therefore, the descending cooled volumes also feature smaller q_v which results in positive Q_l. Similar arguments can be applied to the evaporative cooling mechanism. Then, the descending volumes are only those which were subject to buoyancy reversal in the course of mixing. It is not clear what are the exact contributions of radiative and evaporative cooling towards the observed heat fluxes. Although κ significantly exceeds the critical value (see sec. 4.1), which suggests the importance of evaporation, radiative cooling might still be dominant as in the study of Gerber et al. (2016).

In the decoupled STBL observed in flight #14 (Fig. 5.2ii), the production terms B and S are of the same order as in the coupled case. The COARE 3.0 algorithm provides $B = 4.0{\cdot}10^{-4}$ m^2 s^{-3}, $Q_s = 6.7$ W m^{-2}, $Q_l = 107$ W m^{-2} at the surface. B decreases with height and can be expected to turn into buoyancy consumption in the TSL. This can be considered an important signature of decoupling. In the cloud, B is again positive, yet significantly smaller ($2.6{\cdot}10^{-4}$ m^2 s^{-3}) than at a similar location in the coupled STBL. Shear production is present in the SML and at the transition as well as in the cloud top region.

Sensible heat flux in the decoupled boundary layer is relatively small, reaching the maximum of ∼10 W m^{-2} at ∼140 m. Latent heat flux features a nearly linear decrease with height from the maximum of ∼100 W m^{-2} at the surface to roughly zero close to the transition. In the lower part of the STBL (at the surface, in LEG143 and LEG287) the contribution of moisture transport to buoyancy is of the same order as the contribution of heat transport (not shown). Both sensible and latent heat fluxes observed in the cloud (LEG992) are small, in contrast to the

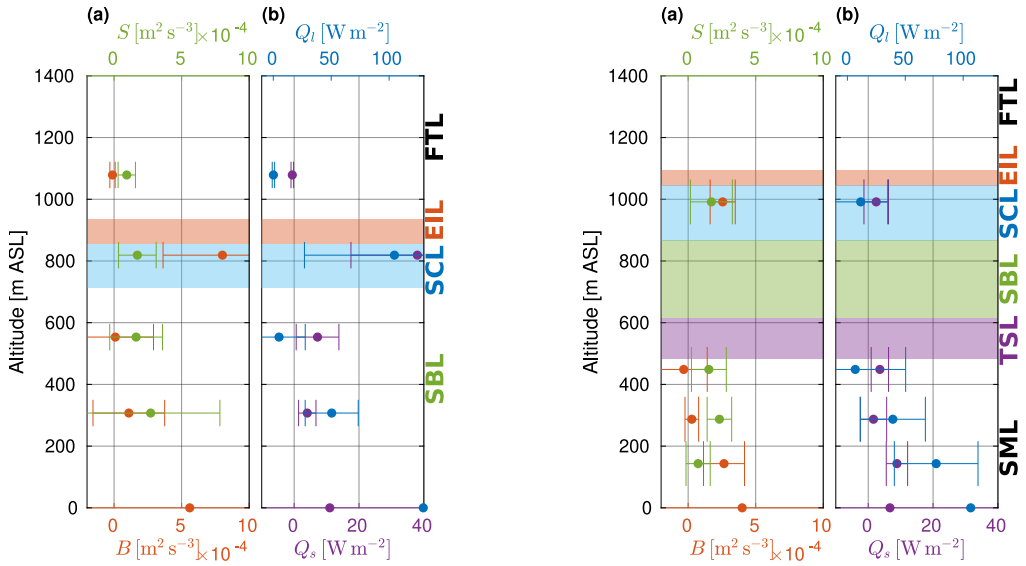

(i) Coupled STBL (flight #5). (ii) Decoupled STBL (flight #14)

Figure 5.2: (a) TKE production by buoyancy B and shear S, (b) sensible Q_s and latent Q_l heat fluxes. The lowest dot denotes the parameterized surface value obtained with the COARE 3.0 algorithm. From Nowak et al. (2021).

coupled case. Together with rather moderate B in the cloud, this suggests that the drivers of convection, i.e. radiative and evaporative cooling, are not as efficient in this situation which might have been one of the reasons why decoupling occurred. The CTEI parameter (see sec. 4.1) is indeed smaller in the decoupled cloud in comparison to the coupled one which implies less efficient evaporative cooling. However, the comparison of radiative cooling effects between the cases requires further investigation. Another observation is that the moisture delivery from the ocean surface to the cloud ought to be limited in the decoupled STBL as Q_l vanishes at a much lower height in comparison to the cloud base than in the coupled case.

5.3 TKE dissipation rate

The measurements in the coupled STBL during flight #5 (Fig. 5.3) indicate relatively small variability of ϵ throughout the boundary layer depth and its substantial decrease right above the cloud top. The values fluctuate by roughly one order of magnitude, between 10^{-4} m^2 s^{-3} and 10^{-3} m^2 s^{-3}. Importantly, those variations do not correlate between the PROFs, hence they are the manifestation of some intermit-

tency and random effects involved in airborne sampling rather than any systematic stratification. Among the LEGs, the highest dissipation rate was observed in the one close to the cloud top, where also substantial B was revealed (see sec. 5.2). On the other hand, the PROF-derived continuous profiles of ϵ do not show any significant difference between the cloud and the subcloud part. It suggests that even though the TKE might be produced at specific places it is probably redistributed well by the circulation across the STBL before being dissipated by viscosity (c.f. transport analysis by Kopec et al. (2016)).

Inside the STBL, the exponents of structure function (sec. 3.2.3.1) and of power spectrum (sec. 3.2.3.2) are close to their theoretical values (2/3 and $-5/3$, respectively), in striking contrast to the FT. The individual deviations occasionally reach 40 % in the STBL. On average, the deviations are a bit smaller inside the SCL than in the SBL (see Table 5.1). Typically, the SFCs and PSDs seem to be flatter than the theory predicts (the absolute values of s and p are smaller than theoretical). Such behavior might be attributed to the inhomogeneity and nonstationarity of turbulence and different stages of its development (Vassilicos, 2015). The SFCs and PSDs of vertical fluctuations follow the Kolmogorov theory closer than those of longitudinal fluctuations, signaling some anisotropy in the turbulence energy cascade.

The correlation coefficients R^{sfc} and R^{psd} (sec. 3.2.3) are close to unity in the coupled STBL. This implies that both the SFC and the PSD can be considered linear in log-log coordinates in the assumed inertial range of scales. The correlation is higher for LEGs than for PROFs due to better averaging. It sharply decreases across the EIL, suggesting that in the FT the assumptions involved in the derivation of ϵ are not satisfied. Therefore, ϵ estimates above the boundary layer cannot be considered credible (Akinlabi et al., 2019). On the other hand, inside the STBL the observed forms of SFCs and PSDs are reasonably consistent with the theoretical predictions.

The measurements in the decoupled STBL during flight #14 (Fig. 5.4) present the lower values of ϵ and more variability with respect to height. The PROF-derived results averaged across the sublayers increase from the SML up to the SCL (see Table 5.2). Such a trend is consistent for all derivation methods and velocity components, despite some differences in the absolute values among them. The LEG-derived ϵ decreases with height, from the surface up to the transition.

The vertical profiles of s and p reveal an internal layering of the STBL. In contrast to the coupled case, all the PROF-derived exponents deviate significantly from the

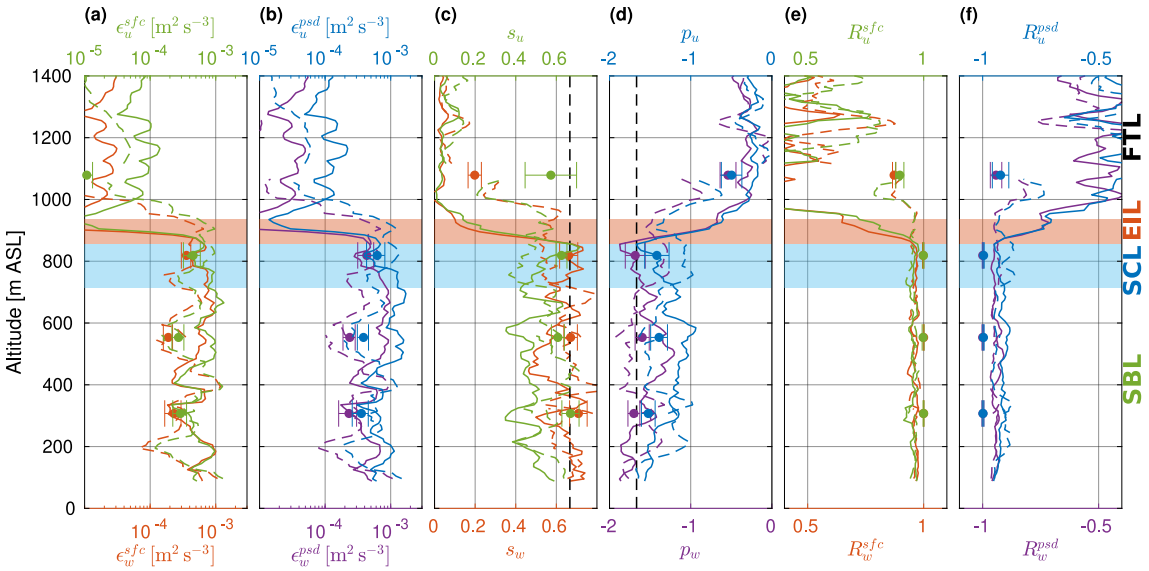

Figure 5.3: TKE dissipation rate and inertial range scaling in the coupled STBL (flight #5): (a), (b) dissipation rate ϵ, (c), (d) fitted exponents s and p, (e), (f) correlation coefficient R. Superscripts sfc and psd denote the structure function and power spectrum methods, respectively. Subscripts u and w denote the horizontal and vertical velocity components, respectively. The dissipation rates for LEG1079 which are not visible in panels (a), (b) are smaller than 10^{-5} m^2 s^{-3}. From Nowak et al. (2021).

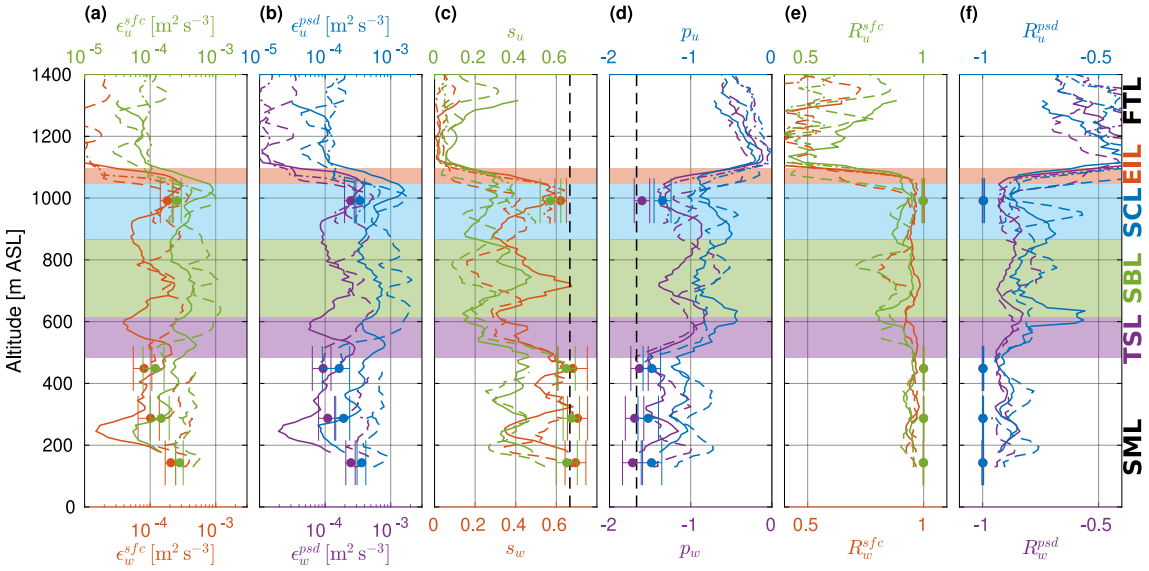

Figure 5.4: TKE dissipation rate and inertial range scaling in the decoupled STBL (flight #14). Notation as in Fig. 5.3. From Nowak et al. (2021).

theoretical values. The deviations are appreciably smaller in the SML than in the SBL and the SCL, clearly demonstrating that the turbulence in the upper part of the decoupled STBL is further from Kolmogorov's concepts than in the lower part. The parameters inside the SCL and the SBL are comparable, suggesting there is an efficient circulation and mixing across them. Those facts were expected, taking into account the analysis of stratification (sec. 4.3.1) and TKE production (sec. 5.2). Most probably, the turbulence generated in the cloud top region is redistributed by the large eddies and the transport terms of the TKE balance equation (Stull, 1988) across the SCL and the SBL. Though, the properties of such turbulence are remarkably far from the Kolmogorov theory assuming homogeneity, isotropy and stationarity. In the light of this observation, the dissipation rates obtained with the methods based on the theoretical inertial range scaling can become questionable. The conditions in the lowermost part of the atmosphere better resemble theoretical Kolmogorov turbulence, albeit the assumptions are still distant from being exactly fulfilled. The profiles of R^{sfc} and R^{psd} are in agreement with the above hypothesis suggesting different character and origin of turbulence in the upper and lower parts of the STBL. The absolute values are smaller than in the coupled case. In the SBL and the SCL, the correlation is even quite poor at some particular heights.

In contrast to the PROFs, the LEG-derived exponents stay mostly close to 2/3 or -5/3, accordingly, while the correlations are close to one. The observed discrepancy might result from the combination of horizontal inhomogeneity and intermittency of turbulence. PROF-derived and LEG-derived parameters should not be directly compared because they represent small and large fluid volumes, respectively (see the discussion in sec. 3.2.3.3). Unfortunately, none of the horizontal segments during flight #14 was performed in the SBL.

5.4 Anisotropy

The coupled STBL sampled in flight #5 features the bulk anisotropy ratios predominantly in the range between 0.5 and 1.0 (Fig. 5.5i). The variance anisotropy ratio is the largest (0.9) for the horizontal segment inside the cloud, close to its top, where the turbulence is efficiently generated by buoyancy (see sec. 5.2). In the SBL, the values are a bit smaller. Despite the substantial local fluctuations in A_ϵ^{sfc} and A_ϵ^{psd}, their average level can be considered constant across the boundary layer. There is very little difference between the SBL and the SCL. The SFC-derived anisotropy

ratio is relatively close to unity, suggesting near isotropic conditions. However, the PSD-derived ratio, typically around 0.6, seems to indicate the dominant role of horizontal fluctuations. The reason for such a discrepancy between the methods is not clear. It can be related to the bias in the estimation of dissipation rates between them (c.f. Wacławczyk et al., 2020). Nevertheless, both anisotropy ratios indicate no internal layering inside the STBL. In the FT, under static stability and weak turbulence production, horizontal motions dominate.

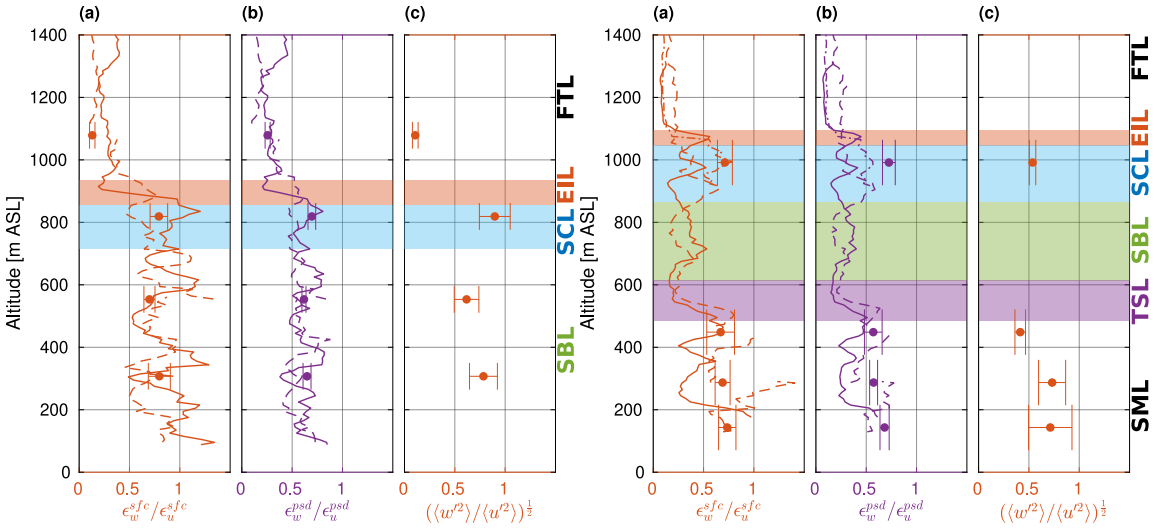

(i) Coupled STBL (flight #5). (ii) Decoupled STBL (flight #14)

Figure 5.5: Turbulence anisotropy ratios. From Nowak et al. (2021).

In the decoupled STBL investigated in flight #14, the bulk anisotropy ratios are on average smaller than in the previous case (Fig. 5.5ii), indicating the prevalence of horizontal fluctuations over the vertical ones. The variance anisotropy is the largest in the surface layer (reaching 0.72), smaller in the cloud (0.54) and close to the transition (0.41). The dissipation anisotropy ratios imply the separation of the STBL into two parts with the border in the TSL. In the upper part, covering the SCL and the SBL, A_ϵ^{sfc} and A_ϵ^{psd} are visibly smaller than in the SML. Again, the PSD-derived ratio is systematically lower than the SFC-derived one but the discrepancy is not as pronounced as in the case of flight #5. Importantly, the change at ∼500 m correlates well with the change in s and p (see sec. 5.3) as well as with the gradient of q_v (see sec. 4.2.1). This fact confirms the hypothesis involving two major circulation circuits dividing the STBL into two parts, cloud-driven and surface-driven, which are internally relatively well-mixed but feature turbulence of different character.

The spectral anisotropy ratios in the coupled STBL presented in Fig. 5.6i are of a similar form for all the three LEGs inside the boundary layer, contrasting with those performed in the FT. Inside the STBL, $A_{\mathcal{P}}$ matches approximately the theoretical value of 4/3 in the range of 5-100 m, indicating the isotropic properties of turbulence in the inertial subrange of the energy cascade. The anisotropy ratios gradually decrease for larger scales which are of the order of the integral length scale (see sec. 5.5). The scales of the order of a few hundred meters, which is close to the boundary layer depth (about 850 m), might be also influenced by the proximity of the bottom and top interfaces limiting their vertical extent. On the opposite side of the spectrum (small scales), $A_{\mathcal{P}}$ can be affected by the differences in the spectral transfer functions of the sonic anemometer for different velocity components (Kaimal et al., 1968). A similar effect was briefly described by Siebert et al. (2006b). In the FT, $A_{\mathcal{P}}$ hardly reaches 1.0 because vertical excursions are damped by stability. In the case of LEG1079, it is particularly small, probably because that level was very close to the strongly stable temperature inversion.

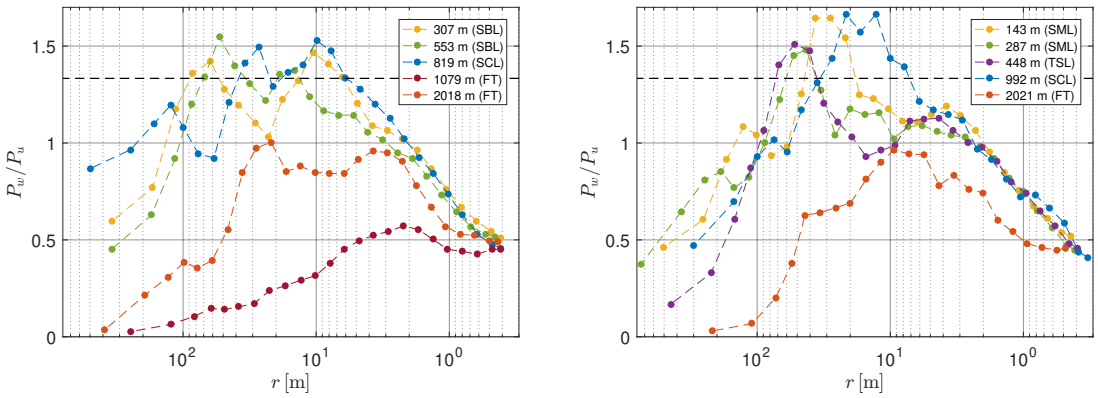

(i) Coupled STBL (flight #5). (ii) Decoupled STBL (flight #14)

Figure 5.6: Spectral anisotropy ratio. The horizontal dotted line denotes the 4/3 level expected for isotropy in the inertial range. From Nowak et al. (2021).

In the decoupled STBL (Fig. 5.6ii), $A_{\mathcal{P}}$ follows a similar pattern as observed in the coupled case. Nonetheless, the maximum values are higher, reaching up to 1.7 at the scales of 20-40 m in LEG143 and LEG992 which are the lowest and the highest segments inside the STBL. One may speculate that those scales, featuring the prevalence of vertical fluctuations, are related to the typical size of surface layer plumes and the typical size of cloud top downdrafts manifested as cloud holes

(Gerber et al., 2005). The range of scales where $A_{\mathcal{P}}$ indicates conditions close to local isotropy is narrower than in the coupled STBL. On the side of large scales, $A_{\mathcal{P}}$ falls below the theoretical 4/3 already at around 70 m for the two central LEGs and around 50 m for the two peripheral LEGs (regarding the perspective of the boundary layer). This observation can be related to the integral length scales which are smaller than in flight #5 for the most part (see sec. 5.5). What is more, the depths of the two sections of the boundary layer corresponding to the supposed circulation circuits (∼500 m) are also smaller than the entire depth of the coupled STBL (∼850 m).

5.5 Length scales

In the coupled STBL, the estimated integral scales vary around 100-150 m (Fig. 5.7i). The longitudinal scale L_u increases, whereas the vertical L_w decreases with height. The ratio L_w/L_u (not shown) decreases from about 1.3 in the lowest LEG to about 0.5 (as expected for isotropic turbulence) close to the cloud top. The variability of the integral scales among the subsegments is extensive, reflecting poor averaging on relatively short distances which prevents the accurate calculation of decorrelation length (see sec. 3.2.5).

The estimated Taylor microscales fit into the range of 30-80 cm and decline with height from the middle to the top of the STBL. As predicted, the longitudinal λ_u is larger than the vertical λ_w. Their ratio λ_u/λ_w equals $\sqrt{2}$ (corresponding to the isotropy of small-scale turbulence) only in the cloud LEG and is larger below. One may speculate that the turbulence is close to isotropic at the time and location of its generation but such isotropy is broken in the process of transport.

The Kolmogorov microscale is almost constant across the STBL (∼2 mm) which can be expected as it depends practically only on the dissipation rate (the viscosity changes only by a minor part in the lower atmosphere).

In the decoupled STBL, the integral scales are significantly smaller in comparison to the previous case, hardly exceeding 100 m (Fig. 5.7ii). The longitudinal L_u dominates over the vertical L_w, probably due to the separation of the circulation into two circuits and due to the weak static stability which both limit the vertical extent of eddies and promote horizontal elongation. In contrast to the coupled case, the ratio L_w/L_u equals about one half in the lowest LEG close to the surface which is, interestingly, again the location of an intensive TKE production.

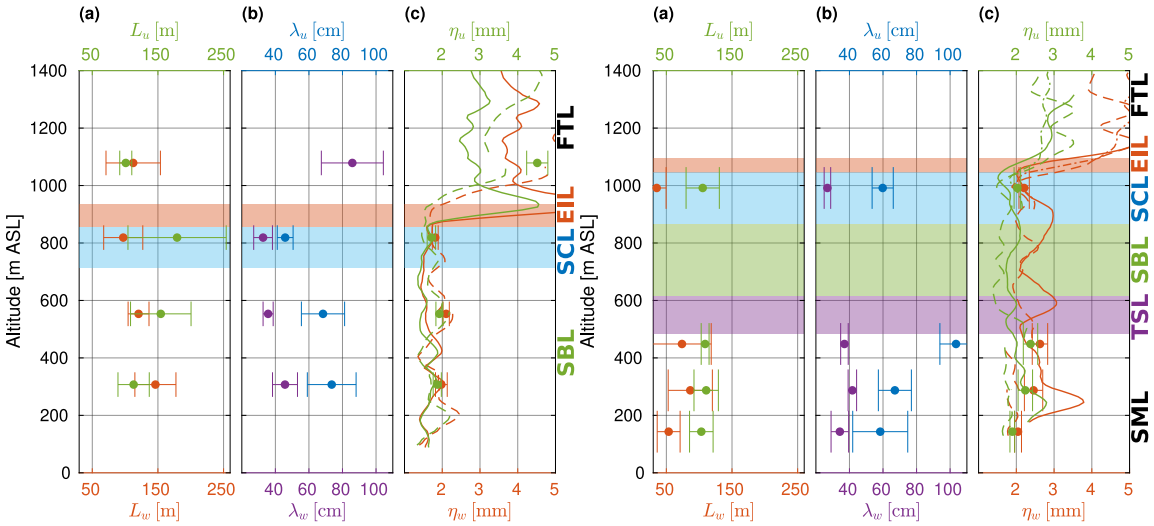

(i) Coupled STBL (flight #5). (ii) Decoupled STBL (flight #14)

Figure 5.7: Turbulent length scales: (a) integral scale L, (b) Taylor microscale λ, (c) Kolmogorov microscale η. Subscripts u and w denote the horizontal and vertical velocity components, respectively. Some of the results for the LEGs in the FT are out of the range presented. From Nowak et al. (2021).

The Taylor microscale is mostly of the same order as in the former case. In the transition zone and the cloud, the substantial detachment between the longitudinal and the vertical can be observed. The ratio λ_u/λ_w is significantly larger than expected for isotropic turbulence. This effect is most pronounced in LEG448 close to the transition. One may speculate it is the consequence of turbulence decay – far from the production in the cloud and at the surface, the TKE is here dissipated and consumed by stability (sec. 5.2).

The Kolmogorov microscale visibly fluctuates but on average it stays close to constant across the STBL. In contrast to the coupled case, there is some difference between η_u and η_w which directly relates to A_ϵ^{sfc} discussed in sec. 5.4.

Table 5.1: Average turbulence properties inside the sublayers of the atmosphere during flight #5 derived from PROF1.

Parameter	**SBL**	**SCL**	**EIL**	**FTL**
Height [m]	0-715	715-855	855-935	1005-1385
ϵ_w^{sfc} [cm^2 s^{-3}]	5.6	6.1	1.9	0.2
ϵ_u^{sfc} [cm^2 s^{-3}]	6.5	6.6	2.2	0.8
ϵ_w^{psd} [cm^2 s^{-3}]	5.6	5.1	1.5	0.3
ϵ_u^{psd} [cm^2 s^{-3}]	9.2	8.5	2.6	1.2
s_w	0.61	0.67	0.29	0.03
s_u	0.47	0.55	0.34	0.05
p_w	-1.53	-1.70	-1.10	-0.31
p_u	-1.25	-1.42	-1.03	-0.23
R_w^{sfc}	0.96	0.97	0.79	0.37
R_u^{sfc}	0.95	0.96	0.87	0.42
R_w^{psd}	-0.94	-0.95	-0.81	-0.49
R_u^{psd}	-0.91	-0.93	-0.81	-0.41
$\epsilon_w^{sfc}/\epsilon_u^{sfc}$	0.87	0.94	0.54	0.28
$\epsilon_w^{psd}/\epsilon_u^{psd}$	0.62	0.63	0.41	0.29
η_w^{sfc} [mm]	1.7	1.6	4.0	4.0
η_u^{sfc} [mm]	1.6	1.6	3.0	2.9

Table 5.2: Average turbulence properties inside the sublayers of the atmosphere during flight #14 derived from PROF5.

Parameter	**SML**	**TSL**	**SBL**	**SCL**	**EIL**	**FTL**
Height [m]	0-385	485-615	615-865	865-1045	1045-1095	1150-1400
ϵ_w^{sfc} [cm^2 s^{-3}]	0.6	1.1	1.2	1.3	1.8	0.1
ϵ_u^{sfc} [cm^2 s^{-3}]	1.2	3.4	3.5	4.6	3.8	0.6
ϵ_w^{psd} [cm^2 s^{-3}]	0.6	1.5	1.6	1.9	2.5	0.1
ϵ_u^{psd} [cm^2 s^{-3}]	1.9	5.6	5.4	7.8	6.5	0.9
s_w	0.52	0.45	0.47	0.44	0.38	0.04
s_u	0.38	0.27	0.33	0.24	0.28	0.16
p_w	-1.39	-1.10	-1.10	-1.11	-1.05	-0.34
p_u	-1.16	-0.76	-0.78	-0.68	-0.85	-0.46
R_w^{sfc}	0.95	0.96	0.96	0.96	0.87	0.30
R_u^{sfc}	0.94	0.91	0.92	0.90	0.89	0.70
R_w^{psd}	-0.90	-0.89	-0.89	-0.89	-0.81	-0.45
R_u^{psd}	-0.89	-0.79	-0.79	-0.79	-0.83	-0.59
$\epsilon_w^{sfc}/\epsilon_u^{sfc}$	0.48	0.31	0.34	0.29	0.48	0.09
$\epsilon_w^{psd}/\epsilon_u^{psd}$	0.34	0.26	0.30	0.24	0.39	0.09
η_w^{sfc} [mm]	3.0	2.6	2.5	2.5	2.4	5.6
η_u^{sfc} [mm]	2.4	1.9	1.9	1.8	1.9	3.0

Chapter 6

Aerosols

The properties of aerosol particles in the coupled and decoupled STBL are presented in the form of vertical profiles and size distribution plots. Mean PROF-derived values inside the sublayers of the atmophere are listed in Tables 6.1 and 6.3; mean LEG-derived values in Tables 6.2 and 6.4. Additionally, the possible origin of the aerosol particles residing in the specific sublayers is discussed. The content of this chapter has not been published.

6.1 Total particle and CCN number concentrations

The vertical variations of N_p and N_{CCN} measured in the coupled and decoupled STBL are shown in Fig. 6.1i, panel (a), and Fig. 6.1ii, panel (a), respectively. There is a very good agreement between the observations from different PROFs during both flights, except for the SBL in the coupled STBL. The offset in N_p between the outgoing ascent (PROF1) and the returning descent (PROF3-5) can be attributed to the advection and temporal evolution of the air mass during the flight. It was noted in sec. 2.5.1 that the cloud field was considerably inhomogeneous which implies variable local conditions.

During flight #5 in the coupled STBL, N_p was observed to be constant with height throughout the SBL. Inside the cloud, it is naturally smaller owing to the activation of a considerable portion of the particles which serve as CCNs in the course of cloud formation. The large variations in the SCL can be explained by the inhomogeneous structure of the cloud and the clearings penetrated by the ACTOS platform during PROFs (see sec. 2.5.1). In the FT, N_p is significantly larger than in the SBL (see Table 6.1) and stays constant with height up to about 1400 m.

Similarly to N_p, there is no trend of N_{CCN} with respect to height in the SBL, though some local fluctuations can be observed. The considerable concentration of interstitial CCNs inside the SCL stems from the clearings penetrated or from the maximum supersaturation level smaller than 0.2 % which was applied in the miniCCNC. In the FT, N_{CCN} is constant up to 1400 m in accordance to N_p. However, in contrast to N_p, it is smaller than in the SBL. This fact suggests that, in comparison to the boundary layer, the free tropospheric aerosol contains much larger proportion of Aitken mode particles which are too small to be activated. Such a speculation is confirmed by the analysis of the size distributions in sec. 6.2.

In general, the constant profiles of N_p and N_{CCN} in the SBL agree with the statement that the coupled STBL is dynamically well-mixed. Strong gradients of both quantities across the EIL indicate that there is limited mixing between the STBL and the FT.

Table 6.1: Average aerosol parameters inside the sublayers of the atmosphere derived from PROF1 of flight #5.

Parameter	**SBL**	**SCL**	**EIL**	**FTL**
Height [m]	0-715	715-855	855-935	1005-1385
N_p [cm^{-3}]	363.2	249.8	367.1	446.2
N_{CCN} [cm^{-3}]	155.5	63.2	109.4	95.6

Table 6.2: Aerosol parameters measured in LEGs of flight #5: mean values (M) and standard deviations among the subsegments (S).

Height [m]	**307**		**553**		**819**		**1079**		**2018**	
	M	S	M	S	M	S	M	S	M	S
N_p [cm^{-3}]	321.3	1.1	320.8	2.5	246.9	18.4	454.9	1.1	445.3	39.2
N_{CCN} [cm^{-3}]	164.3	3.7	161.0	7.2	70.7	15.0	91.4	4.1	87.2	11.1

The stratification of aerosols observed in the decoupled STBL during flight #14 features visible layering in terms of number concentration (Fig. 6.1ii, panel (a)). Inside the boundary layer, N_p and N_{CCN} are smaller than for the coupled case, in agreement with the conclusions of Dong et al. (2015), see sec. 1.2.4. N_p and N_{CCN} exhibit the smallest values inside the cloud which is expected due to droplet activation. In the SBL, the concentrations are smaller than in the SML (see Table 6.3) which indicates inhibited exchange between those parts of the atmosphere. The gradient at the height of 500 m coincides with the change of the properties of small-

scale turbulence (see sec. 5.3 and 5.4) and with the gradient of specific humidity (see sec. 4.2).

One may speculate that the reason for the difference in N_p and N_{CCN} between the SML and the SBL can be twofold. First, the SML is supplied with the particles generated at the ocean surface which are not effectively transported to the upper part of the decoupled STBL due to the split circulations. Second, the cloud might remove some of the CCNs in precipitation. The SBL is supposed to be well-mixed with the cloud, hence also efficiently exchanges aerosols. For this reason, precipitation reduces the aerosol concentration inside both the SCL and the SBL. Drizzle was indeed noticed at the airport shortly before the flight (see sec. 4.3.4). Moreover, if precipitation evaporates partly in the SML, its net effect is to supply processed particles into the SML at the expense of the SBL and the SCL.

In the FT, both N_p and N_{CCN} are larger than inside the STBL. Interestingly, the profiles are rather complex and involve strong vertical gradients which divide the FT into a number of sublayers characterized by different concentrations. This observation relates to the similarly complex stratification of the FT in terms of specific humidity (see sec. 4.3.1).

Table 6.3: Average aerosol parameters inside the sublayers of the atmosphere derived from PROF5 of flight #14.

Parameter	**SML**	**TSL**	**SBL**	**SCL**	**EIL**	**FTL**
Height [m]	0-385	485-615	615-865	865-1045	1045-1095	1150-1400
N_p [cm^{-3}]	234.8	175.9	162.8	133.4	271.4	343.7
N_{CCN} [cm^{-3}]	97.1	68.5	56.7	16.3	90.9	147.2

Table 6.4: Aerosol parameters measured in LEGs of flight #14: mean values (M) and standard deviations among the subsegments (S).

Height [m]	**143**		**287**		**448**		**992**		**2021**	
	M	S	M	S	M	S	M	S	M	S
N_p [cm^{-3}]	235.5	1.8	226.9	5.9	207.7	35.8	146.9	14.0	440.2	7.7
N_{CCN} [cm^{-3}]	100.0	2.5	96.7	3.5	74.9	8.0	20.9	10.5	67.8	7.0

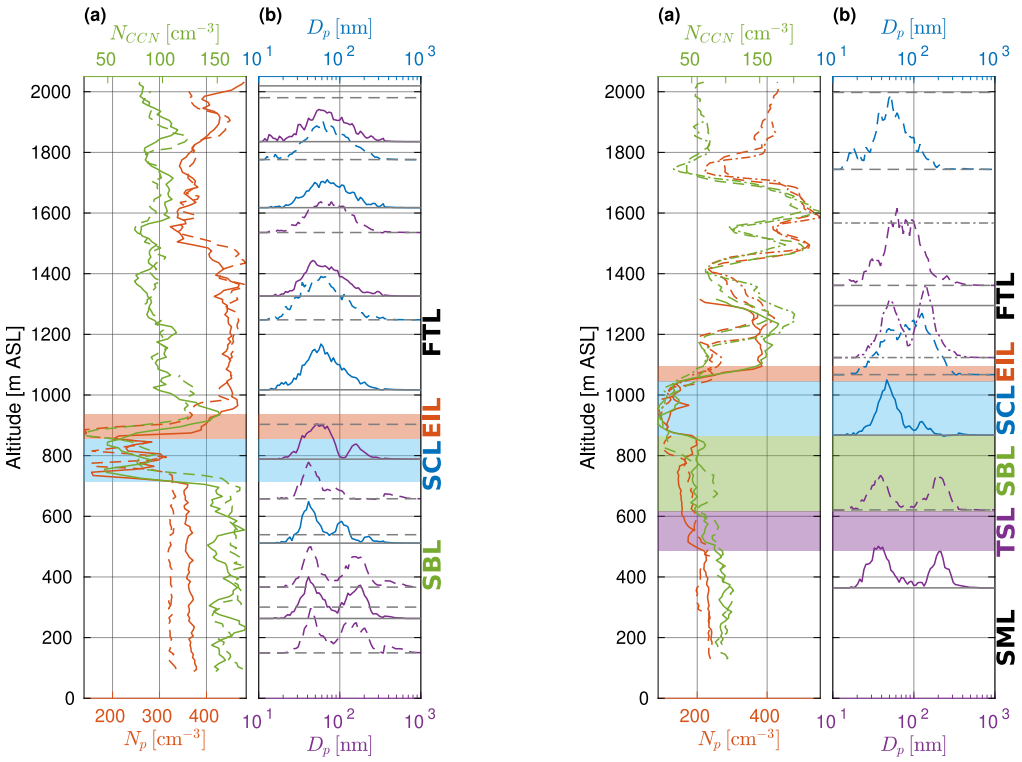

(i) Coupled STBL (flight #5). (ii) Decoupled STBL (flight #14)

Figure 6.1: Vertical variability of aerosol properties: (a) total particle number concentration N_p and cloud condensation nuclei number concentration N_{CCN}, (b) particle number size distributions ($dN/dlogD$) with respect to diameter D_p (the top and bottom axes are the same). Each distribution represents a 2 min scan. Horizontal gray lines indicate the range of altitudes corresponding to the distribution plotted with the same line style. The lower of the two lines is also the zero level for this size distribution. All the size distributions are scaled with the same factor so that they allow the comparison between each other. The color of the line denotes up-scan (blue) or down-scan (purple). Color shading indicates the sublayers which were introduced in ch. 4.

6.2 Size distribution

Individual scans of the particle number size distribution acquired during PROFs are shown in panels (b) of Fig. 6.1. The PNSDs acquired during LEGs are given in Fig. 6.2.

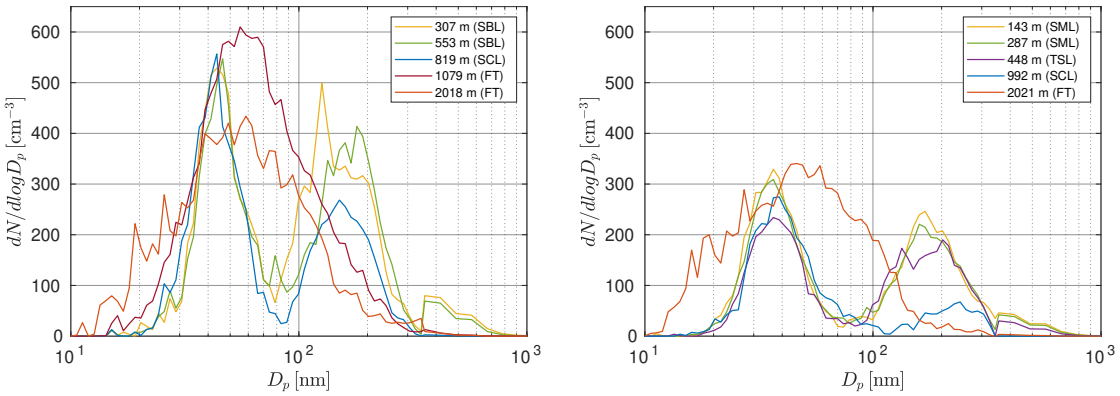

(i) Coupled STBL (flight #5). (ii) Decoupled STBL (flight #14)

Figure 6.2: Aerosol particle number size distributions measured in horizontal segments - average over the individual scans performed within the time of the segment.

6.2.1 Boundary layer

In both flights, the PNSDs predominantly exhibit three modes inside the boundary layer, in agreement with the long-term statistics collected at the ARM ENA site by Zheng et al. (2018a). Those modes peak at the diameters of around 40, 150 and 350 nm. Zheng et al. (2018a) called them Aitken mode, accumulation mode and larger accumulation mode (see sec. 1.4.4). The first two modes feature comparable concentrations while for the last one the concentration is significantly smaller. There is a good agreement between the PROF-derived and the LEG-derived PNSDs with respect to this aspect. In general, the PNSD values are larger for the coupled case, in accordance to the higher total concentrations (see Tables 6.1, 6.2, 6.3 and 6.4).

The size distributions do not vary markedly with height in both STBLs, except for the in-cloud measurements. This could be expected for the coupled STBL which is well-mixed throughout its entire depth. On the other hand, this fact suggests that the particles in the sublayers of the decoupled STBL may come from the same source although their total concentration differs between those sublayers (see Fig. 6.1ii,

panel (a), and Table 6.3). One simple hypothesis explaining such observations would be to assume that the decoupling of the boundary layer under study is not a long-term feature but rather a relatively recent event. Indeed, periodic decoupling is a typical element of the diurnal cycle of an STBL and often occurs in the afternoon due to solar insolation offsetting radiative cooling at the cloud top (see sec. 1.3.1.2). Flight #14 was performed exactly at this time of the day.

Inside the clouds, the PNSDs are affected by activation which removes larger particles to create water droplets. Typically, in-cloud size distributions are supposed to be almost devoid of the accumulation and larger accumulation modes. Due to the scanning strategy explained in sec. 3.3, the results should be interpreted with caution, considering different regions penetrated by the platform. Then, the direction of the profile (ascent or descent) and the direction of the scan (up or down) together with the vertical variability of the total concentration need to be taken into account.

For instance, the forth PNSD from the bottom in panel (b) of Fig. 6.1i (blue solid line) was measured during an ascent (PROF1). The scan started from the smallest diameters at about 500 m and finished with the largest at about 800 m. The Aitken mode was sampled still below the cloud. It is not affected by activation anyway, so no difference is expected in relation to the lower layers. However, only left and right portions of the accumulation mode are visible. The left portion was measured before actually entering the cloud. Additionally, even inside the cloud the supersaturation might have not been enough to activate those relatively small particles. The right portion could have been sampled inside cloud clearings (as this stratocumulus was noticed to be of inhomogeneous patchy character). On a related note, the peak of the accumulation mode measured in LEG819 in the SCL is lower than inside the SBL, yet quite pronounced. This is again the result of averaging cloudy and clear-air volumes. The former are expected to be almost deprived of the particles of this mode, the latter can exhibit aerosol properties similar to the SBL.

Unlike the cloud in the coupled STBL, the decoupled stratocumulus had a homogeneous structure. This explains an almost complete absence of the accumulation mode in the in-cloud LEG992 of flight #14 in contrast to LEG819 of flight #5 (Fig. 6.2, blue lines). Some remaining large diameter particles might have been too hydrophobic to be activated at that particular maximum supersaturation level in the cloud.

6.2.2 Free troposphere

In general, the PNSDs measured in the FT exhibit only one pronounced mode with the peak at the diameter of about 60 nm. The apparent shape and the position of the peak in the case of the PROF-derived size distributions in flight #14 (Fig. 6.1ii, panel (b)) are seriously affected by the scanning strategy (see sec. 3.3) combined with the vertical variability of N_p (Fig. 6.1ii, panel (a)).

For instance, the third distribution from the top in panel (b) of Fig. 6.1ii (dotted-dashed purple line) seems to show two modes. However, such a statement is incorrect because this particular down-scan performed during the descent (PROF4) covered the altitude range from about 1750 m down to almost 1100 m. The minimum in the PNSD at 80-90 nm was then induced by the local minimum in N_p at 1400 m.

Due to the remarkable vertical variability of N_p observed in the FT in flight #14, no conclusions can be formulated regarding the vertical dependence of the PNSDs. On the other hand, the conditions during flight #5 allow to distinguish two sublayers: from ∼1000 to ∼1400 m and from ∼1500 to ∼2000 m (Fig. 6.1i). In the lower sublayer, average N_p is higher and the peak of the PNSD slightly shifted towards smaller diameters in comparison to the upper sublayer.

In both flights, the PNSDs corresponding to the highest sampled altitudes (1800-2000 m) include ultrafine particles (diameters below 25 nm). The presence of ultrafine particles may indicate an active process of new particle formation. Yet, this needs to be confirmed by a further analysis of the process rates and local conditions.

6.3 Air mass origin

The origin of the sampled air volumes residing at different heights was examined using the Hybrid Single-Particle Lagrangian Integrated Trajectory (HYSPLIT) version 4 model (Stein et al., 2015) developed by NOAA Air Resources Laboratory (NOAA ARL). The 5-day backward trajectories were calculated using Global Data Assimilation System (GDAS) meteorological data as input. The results are presented in Fig. 6.3 and 6.4.

For the case of the coupled STBL on 8 July 2017, four levels were chosen: 400 m (in the SBL), 800 m (in the SCL), 1200 m and 1700 m (corresponding to the two sublayers of the FT differing in aerosol properties, see sec. 6.2.2). The first trajectory shows the advection from the NW over the Atlantic. The other three trajectories

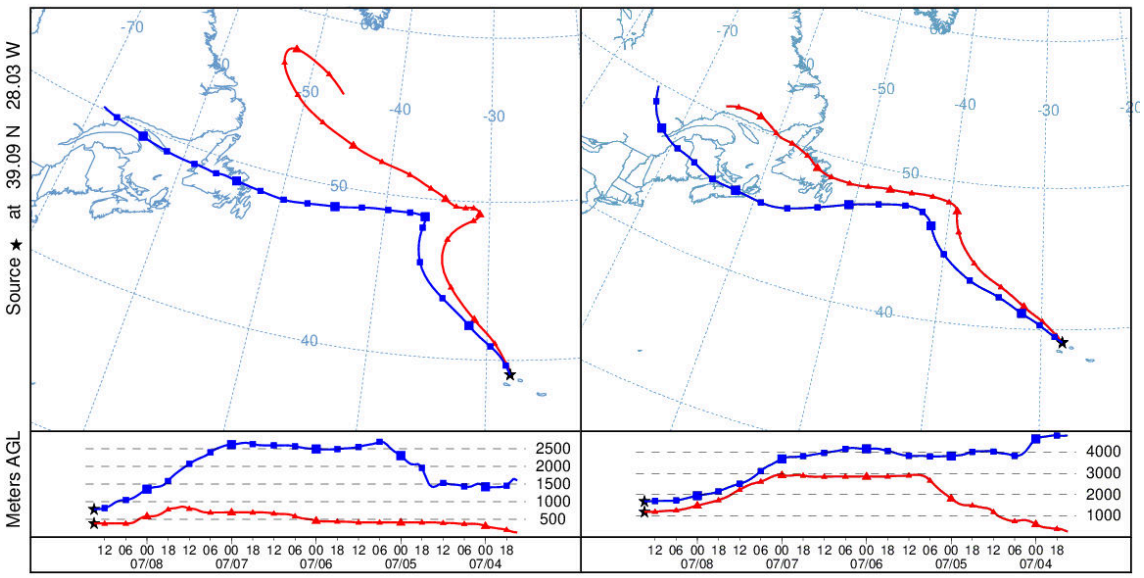

Figure 6.3: 5-day backward trajectories arriving at Graciosa on 8 July 2017 at 15:00 UTC (flight #5 in the coupled STBL) at the heights of 400 (left, red), 800 (left, blue), 1200 (right, red), 1700 (right, blue) m a.s.l. calculated with the HYSPLIT model using GDAS meteorological data as input.

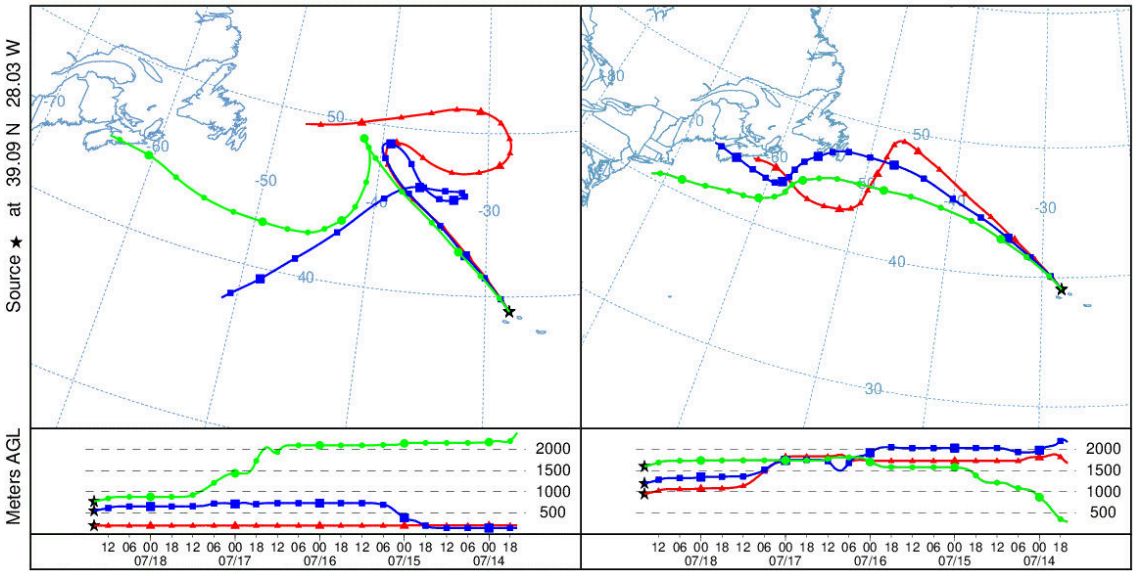

Figure 6.4: 5-day backward trajectories arriving at Graciosa on 18 July 2017 at 16:00 UTC (flight #14 in the decoupled STBL) at the heights of 200 (left, red), 550 (left, blue), 770 (left, green), 950 (right, red), 1200 (right, blue), 1600 (right, green) m a.s.l. calculated with the HYSPLIT model using GDAS meteorological data as input.

are similar to each other. They are related to the advection from North America at high levels which is a frequent pattern in this region (see sec. 1.4.4).

The long-range transport of continental aerosols explains high N_p observed in the FT (see sec. 6.1). In addition, the trajectory ending in the SCL suggests the entrainment of the transported aerosol into the boundary layer. Those observations stay in agreement with the studies of aerosol budget in the marine boundary layer at the site (Zheng et al., 2018a). Recall Fig. 1.30 taken from their work which indicates that Aitken mode particles are principally entrained from the FT; accumulation mode particles originate from the entrainment (note that the free-tropospheric PNSDs partly overlap with the accumulation mode in Fig. 6.2), condensational growth and sea spray aerosol emission; larger accumulation mode is mostly SSA. The difference in N_p between the two levels in the FT might be caused by different exact sources of emission as the trajectories diverge in height at about 3 days back.

For the case of the decoupled STBL on 18 July 2017, six levels were selected: 200 m (in the SML), 550 m (in the TSL), 770 m (in the SBL), 950 m (in the SCL), 1200 m and 1600 m (corresponding to the two levels in the FT differing in aerosol properties, see sec. 6.1). The three lower trajectories show the advection from the NW. However, they diverge in direction at about 1.5 day back. Those corresponding to the SML and the TSL stay at low level over the ocean. The one corresponding to the SBL comes from North America and signals the entrainment from high altitudes. The upper three trajectories are similar to each other. They indicate long-range transport from the American continent.

In general, the implications of the air mass analysis for the aerosol budget in the boundary layer are similar as given for the coupled case. Nevertheless, the trajectories suggest different origin of the air in the upper (SCL+SBL) and lower (SML+TSL) portions of the decoupled STBL. However, it is unknown when the decoupling emerged. A considerable amount of aerosol particles might have been entrained from the FT and mixed inside the STBL before the onset of decoupling.

Chapter 7

Summary and discussion

This chapter collects the results of the study, compares them with the relevant observations reported in the literature and discusses the findings in the broader context of STBL dynamics. The content of the chapter is based on sec. 6 of Nowak et al. (2021). Here, the material is considerably complemented with additional details.

7.1 Comparison of the cases

Two cases of marine stratocumulus-topped boundary layer, coupled (**CP**) and decoupled (**DCP**), have been compared in terms of stratification, turbulence and aerosol properties. The observations were performed in summer in the region of the ENA with the use of the helicopter-borne platform ACTOS. Its moderate true air speed in combination with the closely collocated fast-response instruments provides high spatial resolution measurements of turbulent fluctuations of wind velocity, temperature and humidity. Similarities and differences between the two cases can be summarized as follows.

1. *Cloud structure*

   CP Horizontally heterogeneous stratocumulus cloud consisted of dispersed patches with clearings in between.

   DCP Relatively homogeneous stratocumulus cloud overcast the sky. Little cumuli at the initial state of formation were emerging below. They did not reach the base of stratocumulus.

2. *Stratification*

   CP Conserved variables, θ_l and q_t, feature nearly constant profiles up to the capping inversion at ∼850 m. LCL can be considered consistent with the cloud base height.

   DCP Above the relatively well-mixed SML, θ_l slowly increases with height up to the capping inversion at ∼1050 m, indicating weak stability. There is a significant gradient of q_t in the TSL. LCL is close to the observed stratocumulus base in the SBL only. Decoupling of the STBL was detected according to the simple thermodynamic criteria.

   In both cases, winds are moderate and appreciable wind shear is observed across the cloud top and the EIL.

3. *TKE production*

   CP TKE is efficiently generated by buoyancy with simultaneous importance of in-cloud and surface processes. Buoyancy production follows a typical STBL profile: decreases with height from the surface upwards, vanishes or turns slightly negative below the cloud base, to be again substantial inside the cloud due to latent heat release and diabatic cooling.

   DCP TKE is generated by buoyancy at the surface and B decreases with height to zero at the SML top, turning into buoyancy consumption in the TSL. In the cloud, B is weaker than at the surface, about three times smaller than for the coupled case. Buoyancy effects can be also deduced from spectral anisotropy in the uppermost and lowermost boundary layer LEGs which suggest the dominance of vertical motions in the scales of 10-40 m.

   The contribution of shear to TKE production is not negligible in both cases. This result can be partly an artifact because only the longitudinal term could be evaluated.

4. *Heat fluxes*

   In both cases, latent heat flux qualitatively resembles the profile of B which is consistent with the considerable contribution of moisture transport to buoyancy in the lower part of the STBL. Q_l is large at the ocean surface and

decreases to zero at similar level as the minimum of B. Sensible heat flux is positive throughout observed layers but mostly smaller than Q_l.

CP Q_l and Q_s are positive and of significant magnitude close to the cloud top which can be attributed to diabatic cooling (radiative and/or evaporative).

DCP Q_l and Q_s are small close to the cloud top, about an order of magnitude weaker than for the coupled STBL. Additionally, Q_l vanishes in the middle of the boundary layer at a level much lower in relation to the cloud base which disturbs moisture delivery from the ocean to the stratocumulus cloud.

5. *Turbulent fluctuations*

In both cases, TKE is dominated by the contribution of horizontal velocity fluctuations. Variances of temperature and humidity are significant in the regions where mixing between air volumes of different properties occurs – due to local gradients or sources/sinks, i.e. at the cloud top, at the surface and at the transition in the decoupled STBL.

CP Maximum TKE is found in the middle of the SBL, which together with the positive $\langle w'^3 \rangle$ at this level point out the role of surface-related factors in generating convection. The vertical velocity variance suggests a profile somewhat different than the convective similarity scaling. In the cloud, $\langle u'^2 \rangle$ and $\langle w'^2 \rangle$ are almost equal implying isotropic conditions.

DCP The SML follows the structure of a typical mixed layer with shear (c.f Stull, 1988). Updrafts are stronger than downdrafts. TKE, $\langle T'^2 \rangle$ and $\langle q_v'^2 \rangle$ are the largest close to the transition. In the cloud, the fluctuations are relatively weak, in particular $\langle w'^2 \rangle$, in concordance with limited B and small heat fluxes.

6. *TKE dissipation*

CP Derived ϵ varies weakly throughout the height, i.e. despite accidental variations no systematic layering can be observed. Although TKE is efficiently produced by buoyancy in the cloud and at the surface, it is probably redistributed well across the depth before being dissipated by vis-

cosity. The form of SFCs and PSDs is reasonably consistent with the theoretical predictions for inertial range scaling in homogeneous, isotropic, stationary turbulence (Kolmogorov, 1941). Though, less steep scaling (smaller absolute values of s and p) can be found at some places in the SBL.

DCP Derived ϵ is smaller than in the coupled case and features differences between the sublayers. Despite relatively high B at the surface, similar to the coupled case, average ϵ in the SML is smaller than in the SCL. Importantly, SFCs and PSDs scaling in the inertial range considerably deviates from the theoretical slopes (2/3 and -5/3). These deviations are more pronounced and more variable in the SCL and SBL in comparison with the SML, underlining different character of turbulence in the upper and lower parts of the decoupled STBL. Probably, TKE generated in the surface region and in the cloud, respectively, is redistributed in the two circulation zones separately, without major transport through the transition.

Discrepancies between PROF-derived and LEG-derived quantities result from the contrast between local and mean turbulence characteristics. The observed relative tendencies are consistent among the derivation methods and velocity components, in spite of some discrepancies in the absolute values.

7. *Anisotropy of turbulence*

CP Derived anisotropy ratios indicate that the turbulence is relatively close to isotropy. This condition is met best in the cloud where a significant TKE production occurs.

DCP The degree of anisotropy varies between the sublayers. In the uppermost part (SCL and SBL) horizontal small-scale velocity fluctuations dominate over the vertical. This effect is less pronounced in the SML. The change in anisotropy ratios in the TSL coincides with the difference in s and p right below the strong q_v gradient.

8. *Length scales of turbulence*

Integral length scales of the order of 100 m show that turbulent eddies are substantially smaller than the depth of the STBL or the depths of the decou-

pled sublayers. Thus, they can be considered small enough to be transported by larger circulations.

CP In the middle SBL, w' is correlated on longer distances than u', while the opposite holds in the SCL. This agrees with the supposed form of circulation in the boundary layer, i.e. downdrafts originated at the cloud top and updrafts originated at the surface pair in the middle and diverge horizontally in the vicinity of the top and bottom boundaries.

DCP Integral length scales are smaller than in the coupled case. In accordance with anisotropy ratios, L_u is larger than L_w. The same holds for Taylor microscales. The difference between λ_u and λ_w is particularly pronounced close to the transition. It seems that even smaller turbulent eddies there are elongated horizontally.

Interestingly, $L_w/L_u \approx \frac{1}{2}$ implied by isotropy assumption holds only in the regions of intensive buoyant TKE production: in the cloud for the coupled STBL and close to the surface for the decoupled STBL. Kolmogorov scale is $\sim$2 mm in both cases.

9. *Aerosols*

In both STBLs, the particle number size distributions do not change significantly with height (except for the influence of activation in the cloud) and indicate three principal modes: Aitken, accumulation and larger accumulation. In the FT, there is one major mode. Ultrafine particles were observed at the highest altitudes of the measurements. Total particle and CCN number concentrations exhibit strong gradients across the EIL which indicates limited exchange between the STBL and the FT. Backward trajectories suggest boundary layer advection from the NW over the ocean for the lowest levels ($\lesssim$700 m) and the transport from North America combined with a possible entrainment of the long-range-transported aerosols into the boundary layer for the higher levels.

CP N_p and N_{CCN} are constant with height in the SBL. In the FT, N_p is larger while N_{CCN} smaller than in the boundary layer.

DCP Average N_p and N_{CCN} are smaller than in the coupled STBL. In the SBL, the concentrations are smaller than in the SML, indicating an inhibited

exchange of particles between the sublayers. The gradients of N_p and N_{CCN} inside the TSL coincide with the change in the properties of small-scale turbulence and the gradient of q_v. In the FT, N_p and N_{CCN} are larger than in the boundary layer.

7.2 Results in the light of literature

7.2.1 Coupled STBL

Most of the results concerning the coupled case are consistent with the previous studies of stratocumulus dynamics (see sec. 1.2). The thermodynamic stratification represents a well-mixed STBL (e.g. Stull, 1988; Markowski and Richardson, 2010; Wood, 2012; Malinowski et al., 2013). It is slightly unstable which is a usual situation according to Ghate et al. (2015). The profile of B shows that the convection is driven both by cloud top cooling and by surface thermal instability, in agreement with Duynkerke et al. (1995), Stevens et al. (2005), Kopec et al. (2016), Mellado et al. (2018) and Dodson and Small Griswold (2021). The latent heat flux dominates over the sensible heat flux, in accordance to Ghate et al. (2015). The profile of Q_l resembles the results of Dodson and Small Griswold (2021), indicating maxima at the surface and in the cloud while a minimum in the middle of the boundary layer. The variances of temperature and humidity maximize in the cloud, similarly to Duynkerke et al. (1995). $\langle w'^3 \rangle$ is positive in the middle of the SBL and nearly zero otherwise, as in the modeling case of DYCOMS-II RF01 (Stevens et al., 2005; Mellado et al., 2018) but in contrast to the case of POST TO13 (Kopec et al., 2016). The concentration and size distribution of aerosols are constant throughout the SBL while the dominant sources of aerosol particles are likely sea spray emission and long-range transport from North America combined with the downward entrainment into the STBL, in agreement with the previous measurements in the region (Dzepina et al., 2015; Zheng et al., 2018a; Wang et al., 2020).

On the other hand, the profile of $\langle w'^2 \rangle$ is somewhat different than the upside-down convective similarity scaling (Lenschow et al., 1980). It rather exhibits maxima in the cloud and in the middle of the SBL while a minimum below the cloud, in contrast to Duynkerke et al. (1995), Stevens et al. (2005), Kopec et al. (2016) and Mellado et al. (2018). However, such a behavior of $\langle w'^2 \rangle$, followed by A_{var}, is similar to the observations of Dodson and Small Griswold (2021). TKE is maximum in the

middle of the SBL, instead of the top and bottom of the boundary layer (Stevens et al., 2005; Kopec et al., 2016). Together with the positive $\langle w'^3 \rangle$, this highlights the importance of surface processes. It might be related to the small cloud depth (relative to the STBL depth) and the net cooling at the cloud top reduced during daytime in comparison to often considered nocturnal stratocumulus. Furthermore, no clear maxima of ϵ at the top and at the bottom of the STBL were observed, in contrast to Stevens et al. (2005) and Mellado et al. (2018). This is rather related to the difference in sampling strategy, as aircraft measurements or numerical studies apply a considerable horizontal averaging in comparison to local variability captured in PROFs analyzed here.

7.2.2 Decoupled STBL

The observations in the decoupled STBL summarized in the points 2-5 in sec. 7.1 fit well into the range of conditions reported in the literature (see sec. 1.3). The thermodynamic stratification is slightly stable (c.f. Ghate et al., 2015) and involves the sublayers which are typical for a decoupled STBL (c.f. Fig. 1.16). The considerably deep SBL is dynamically connected with the SCL, similarly to Nicholls and Leighton (1986) but in contrast to Nicholls (1984) and De Roode and Duynkerke (1997) who did not observed independent SBL and TSL. The separation between the SBL and the conditionally unstable TSL is indicated by the gradients in q_v and LCL, in accordance to Nicholls and Leighton (1986) and Jones et al. (2011). On the other hand, the separation between the TSL and the SML is not as clear in the thermodynamic profiles, similarly to Lambert et al. (1999) but in contrast to Nicholls and Leighton (1986) and Tjernström and Rogers (1996). Mean LCL in the SML is higher than the top of this sublayer but significantly lower than the stratocumulus base, as in Lambert et al. (1999).

Vertical velocity variance is small close to the transition and relatively large in the middle of the SML, comparably to Nicholls (1984), Nicholls and Leighton (1986), De Roode and Duynkerke (1997) and Tjernström and Rogers (1996). There is not enough data collected in the SCL and SBL to judge whether those sublayers exhibit an upside-down convective scaling as in the studies mentioned. TKE is large close to the transition, in contrast to De Roode and Duynkerke (1997). Nevertheless, the positive $\langle w'^3 \rangle$ in the SML and negative $\langle w'^3 \rangle$ in the SCL agree with Nicholls and Leighton (1986), De Roode and Duynkerke (1997) and Lambert et al. (1999).

Similarly to Nicholls (1984), the observed $\langle T'^2 \rangle$, and $\langle q_v'^2 \rangle$ are significant close to the surface and close to the transition while showing a local minimum in the SML. The analogous behavior of $\langle u'^2 \rangle$ is contrary to the linear decrease with height in the SML suggested by Tjernström and Rogers (1996).

The latent heat flux is larger than the sensible heat flux, as in Durand and Bourcy (2001). Q_l decreases nearly linearly from the maximum at the surface (Bretherton et al., 1995; Bretherton and Wyant, 1997) to about zero in the TSL, in agreement with Nicholls (1984), Tjernström and Rogers (1996) and Durand and Bourcy (2001). However, Lambert et al. (1999) disputed the nearly linear character of this decrease, suggesting rather sharp gradient right at the SML top. Q_s is maximum in the middle of the SML and reaches a minimum at somewhat lower altitude than Q_l, as observed by Lambert et al. (1999). In contrast to the previous studies (Nicholls, 1984; Tjernström and Rogers, 1996), both heat fluxes are small in the cloud.

Buoyant TKE production is positive in the cloud and at the surface, while there is a region of negative B around the transition, in agreement with Nicholls (1984), Turton and Nicholls (1987), De Roode and Duynkerke (1997) and Durand and Bourcy (2001). The decrease of B with height in the SML is nearly linear as in Nicholls (1984) and Lambert et al. (1999). In the lower part of the boundary layer, the contribution of moisture transport to buoyancy is dominant over sensible heat transport, as noticed by Lambert et al. (1999) and Durand and Bourcy (2001).

Although the PROF-derived dissipation rate is very variable with height, its mean value in the upper part of the boundary layer (SBL+SCL) is larger than in the lower part (SML+TSL), as in Lambert et al. (1999) and Durand and Bourcy (2001). The LEG-derived ϵ representing horizontally averaged conditions decreases with height in the SML, similarly to the measurements of Lambert et al. (1999).

The properties and origins of aerosols in the decoupled STBL are generally comparable to the coupled case. However, average N_p and N_{CCN} are smaller than in the coupled STBL, in agreement with Dong et al. (2015).

7.2.3 Novel findings

The important novelty of this work are the results on small-scale turbulence (points 6-8 in sec. 7.1). To the best of the author's knowledge, the parameters like local dissipation rate, inertial range scaling exponents, small-scale turbulence anisotropy as well as turbulent length scales were not considered in the context of STBL cou-

pling before. Although Lambert et al. (1999) proposed the method of diagnosing decoupling based on the minimum in ϵ profile, they derived ϵ from slanted aircraft segments. Therefore, it can be considered horizontally averaged in relation to the values derived from much steeper helicopter PROFs.

The results on aerosol properties are not particularly surprising, taking into account the difference in circulation patterns between the coupled and decoupled STBLs (see sec. 7.3). Nevertheless, to the best of my knowledge, the sharp gradients in N_p and N_{CCN} in the middle of the decoupled boundary layer have not been explicitly measured and the PNSDs have not been compared between the decoupled sublayers before.

7.3 Importance of circulation and small-scale turbulence

Based on the results presented in this work, one can hypothesize that turbulence is redistributed across the depth of a coupled STBL but in the case of a decoupled STBL primarily in the sublayer where it was generated. Therefore, specific microscopic properties – TKE dissipation rate, inertial range scaling and anisotropy – can differ between the parts of a decoupled STBL.

It is important to emphasize the often omitted distinction between *circulation* and *turbulence*. Here, by *circulation* one should understand motions responsible for mixing across relatively deep layers, of vertical scales comparable to the boundary layer depth. They usually originate from thermally driven currents, sinking from the cloud top or rising from the surface. Circulation might take the form of the organized structures of downdrafts and updrafts (resembling Rayleigh-Bennard convection cells). Those correspond to the peak in vertical velocity spectra, typically at ∼1 km in STBLs (Lambert and Durand, 1999). *Turbulence* features a cascade of eddies with universal scaling properties (Kolmogorov, 1941), spanning from the integral length scale (∼100 m in STBLs) down to the Kolmogorov scale (∼1 mm) where TKE is dissipated by viscosity. Such turbulence can be generated by flow instabilities at specific locations (here typically close to the surface and the cloud top) and distributed by circulation within the STBL, alongside other constituents.

Importantly, the variances and fluxes estimated in this study (sec. 5.1 and 5.2) include the contributions of both those phenomena. Circulation is only partly resolved as the cutoff of ∼1 km in Reynolds decomposition was applied due to the

limited length of the LEGs (sec. 3.2). Similar issue was also discussed by De Roode and Duynkerke (1997). The advantage of this work is a good representation of turbulence because here a significant portion of the inertial range is resolved. The main processes operating in the coupled and decoupled STBLs, including circulation and turbulence, are schematically illustrated in Fig. 7.1.

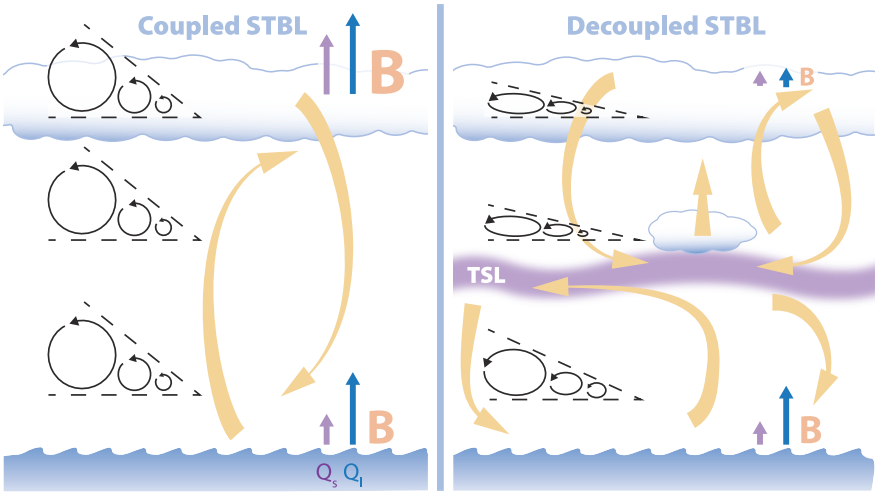

Figure 7.1: Schematic of the main processes in the coupled (left) and decoupled (right) STBL: primary circulation (yellow arrows), turbulence eddy cascade (circular arrows confined in an angle with extent proportional to inertial range scaling exponent p), TKE buoyancy production (red B letter of size proportional to strength), sensible and latent heat fluxes (purple and blue arrows, respectively, of length proportional to strength) at the surface and in the cloud top region. The sketch was drawn by Katarzyna Nurowska according to my concept. From Nowak et al. (2021).

7.4 Potential mechanisms responsible for the observed decoupling

The results of the comparison between the coupled and decoupled STBL are in agreement with the common concept of the dominant mixing patterns in such boundary layers (e.g. Wood, 2012). Decoupling occurs when the thermally driven circulation weakens to the level that it cannot mix air throughout the entire depth. Then, the STBL separates into two parts: cloud driven and surface driven. Explaining the particular mechanism of decoupling operating in the presented case is beyond the scope of this study and would require more complete data on airmass evolution.

Nevertheless, "deepening-warming" mechanism (Bretherton and Wyant, 1997) seems plausible. Such a conclusion was reached by Kazemirad and Miller (2020) who modeled the Lagrangian evolution of the STBL on synoptic scale in the period including flight #14 on 18 July 2017. Deepening-warming is typical for the summertime in the region of ENA where air masses are advected over progressively warmer waters (see sec. 1.3.1.1). The most important driver for this process is the increasing ratio of surface latent heat flux to net radiative cooling in the cloud. The former was indeed relatively large, the latter was probably relatively small, as suggested by the weak heat fluxes (see sec. 5.2). Decoupling occurs more readily for large entrainment efficiency. The derived B is quite weak in the decoupled cloud, much smaller than in the coupled one, which might be the result of enhanced entrainment warming offsetting radiative cooling (c.f. De Roode and Duynkerke, 1997). In addition, some precipitation was reported shortly before the flight (see sec. 4.3.3) and evaporative cooling could have contributed to stabilizing the lower part of the STBL. To sum up, several mechanisms described in sec. 1.3.1 might have contributed to the observed decoupling. The exact effects of the individual processes is rather impossible to discern on the ground of the presented data which are confined to the period of the flight.

7.5 Transition layer and cumulus convection

Both turbulence and circulation can contribute to the vertical transport of heat and moisture which is crucial for maintaining a stratocumulus cloud. In a decoupled STBL, the transport by turbulence through the transition is rather limited. However, it may be efficiently realized by a small number of updrafts which are strong and moist enough to penetrate the conditionally unstable TSL (here, measured $\Gamma = -7.1\ \mathrm{K\,km^{-1}}$, moist adiabatic $\Gamma_m = -4.7\ \mathrm{K\,km^{-1}}$), reach their LCL and form cumulus clouds. The image of such cumuli was captured by a camera onboard ACTOS (Fig. 7.2). Based on the series of images from PROF5, the cloud base height was estimated to ∼660 m and the cloud depth to ∼100 m. None of those cumuli was penetrated by ACTOS.

The onset of cumulus convection depends on the properties of the TSL which makes this sublayer crucial for the overall STBL dynamics. The altitude range corresponding to the TSL was estimated in sec. 4.3.2 based on the gradients of q_v, θ_l and U observed in PROF5. However, the layer containing the strongest gradients

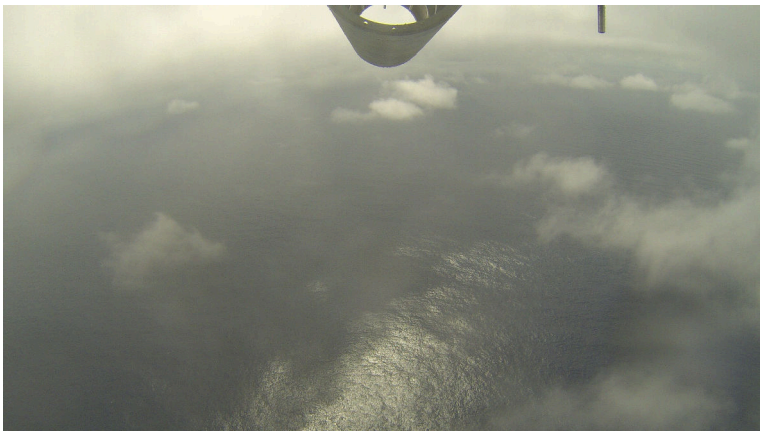

Figure 7.2: Cumulus clouds under stratocumulus in the decoupled STBL. Photograph was taken during PROF5 of flight #14 by the camera mounted on the bottom of ACTOS. From Nowak et al. (2021).

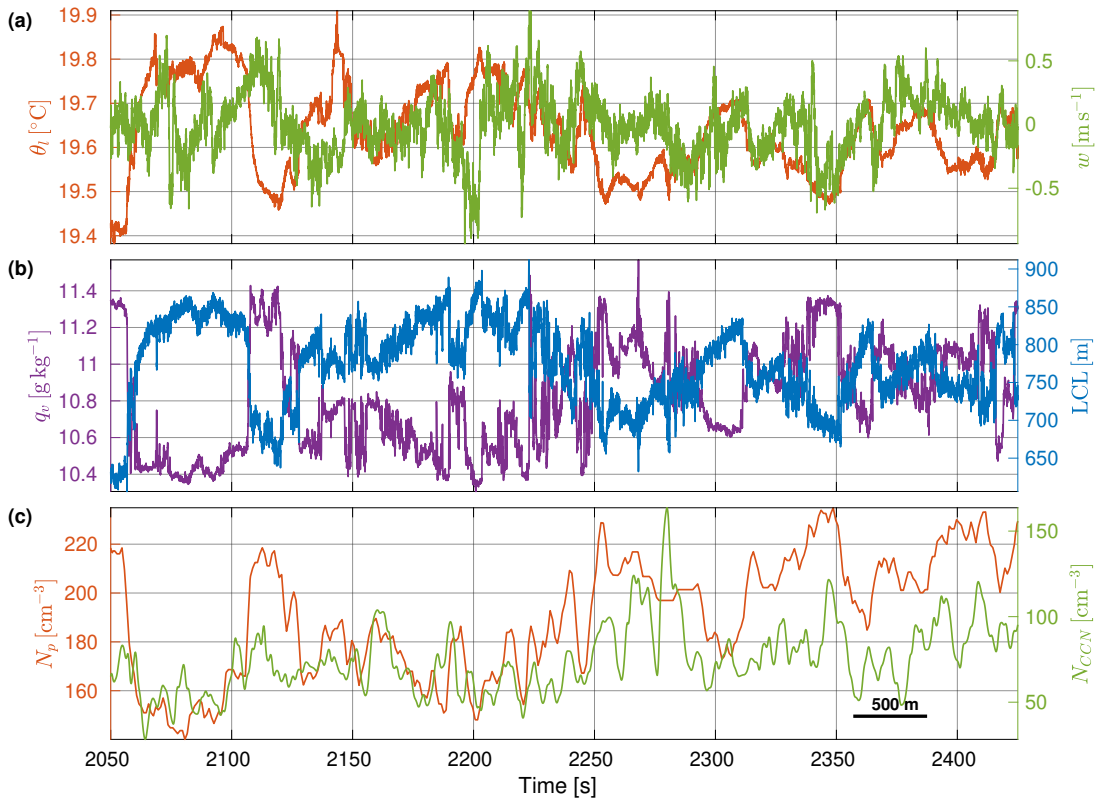

Figure 7.3: Timeseries measured in LEG448 of flight #14 (decoupled STBL): (a) liquid water potential temperature θ_l and vertical wind velocity w, (b) specific humidity q_v and lifting condensation level LCL, (c) total particle N_p and CCN N_{CCN} number concentrations.

can be significantly thinner while its exact location and depth vary in space and time. This gradient layer was penetrated several times during LEG448 (Fig. 7.3). The data suggest that the gradient layer is not horizontally flat but rather undulating because the variations in platform altitude (standard deviation is 10 m for LEG448) cannot explain the observed variations in the signals. Consistently with the difference in the conditions across the TSL, the changes of θ_l are correlated with LCL but anticorrelated with q_v, N_p and N_{CCN}. Based on the timeseries of LEG448 and PROF5, the estimated depth of the gradient layer is $\Delta z \approx 50$ m while the corresponding differences in conditions are: $\Delta\theta \approx 0.4$ K, $\Delta q_v \approx 1$ g kg^{-1}, $\Delta RH \approx 8$ %, $\Delta U \approx 0.8$ m s^{-1}, $\Delta LCL \approx 200$ m, $\Delta N_p \approx 70$ cm^{-3}, $\Delta N_{CCN} \approx 50$ cm^{-3}.

The histograms of the instantaneous LCL (Fig. 7.4) indicate that LEG448 was performed at the top interface of the SML. Some values represent the conditions in the SML as measured in LEG143 and LEG287, some represent the conditions in the SBL (note that the mean LCL in the SBL is 769 m, see Table 4.3) and some represent the conditions intermediate between the SML and the SBL. Importantly, the estimated cumulus base corresponds to the LCL typical for LEG143 and LEG287 in the SML. This fact indicates that the cumulus plumes originate in the SML and they are subject to rather limited entrainment in the TSL before reaching their respective LCL. Such conclusion is also supported by the increased ceilometer backscatter coefficient below the cumulus clouds detected at the ARM ENA site after the flight (see sec. 4.3.4).

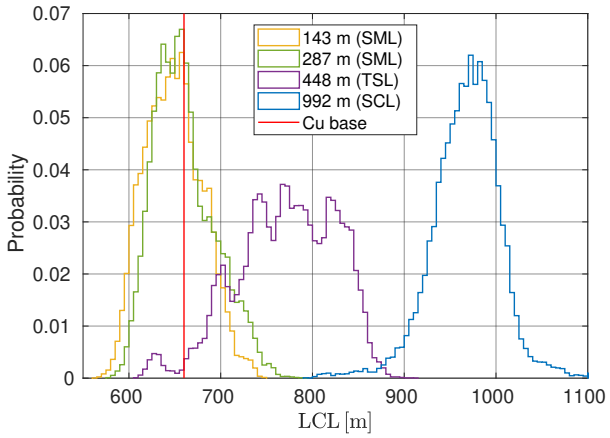

Figure 7.4: Histograms of the instantaneous LCL measured during LEGs in the decoupled STBL. The red line denotes the base of cumulus clouds estimated from the series of photographs captured by the camera onboard ACTOS.

The gradient layer described above is contained in the TSL and shares many characteristics with the EIL capping the STBL. Analogously to the EIL controlling the transport between the STBL and the FT, this gradient layer controls the transport between the SML and the SBL. Contrary to the strongly stable EIL, its weak stability enables some updrafts from the SML to penetrate, form cumulus clouds and provide an intermittent transport, which is crucial for maintaining and driving the evolution of the overlying stratocumulus. Despite their inevitable importance for the dynamics of STBLs, the properties of the TSL and the gradient layer have not been systematically investigated.

It is a challenge to conduct a relevant systematic climatological analysis due to the limited number of observations. Aircraft measurements are scarce while the resolution of routine radiosoundings is often insufficient. For instance, the gradient in q_v is rather poorly resolved in the radiosounding given in Fig. 4.5. With a typical ascent rate of $\sim$5 $\mathrm{m\,s^{-1}}$ and a sampling interval of $\sim$2 s, a hygrometer with a time constant of a second and an accuracy of a single percent in RH would be desired. It would be even more challenging to detect the small difference in θ_l. As a consequence, common criteria for diagnosing STBL decoupling are based on the difference in mean conditions between the uppermost and lowermost portions of the boundary layer (see sec. 3.1.2).

Because the gradient layer is undulating as suggested by the data of LEG448, even aircraft measurements may fail to properly capture local conditions. This was pointed out already by Turton and Nicholls (1987), p. 997, who underlined the role of a good observation strategy: "While cloud layer decoupling is predicted to occur quite often, the consequential modification of the horizontally averaged vertical thermodynamic structure remains fairly small. (...) Data averaged in this way will appear 'nearly well-mixed' whether separation has occurred or not. A more detailed analysis of individual profiles and turbulence data is necessary to determine whether decoupling has taken place".

More insight into the mechanisms of vertical transport in a decoupled STBL can be provided by appropriately designed numerical simulations. The case of 18 July 2017 analyzed in the current study also calls for a high-resolution simulation to be setup with the help of the results presented here.

Appendix A

Sampling errors of turbulent moments and fluxes

The estimation of sampling errors was performed following the methods given by Lenschow et al. (1993, 1994). They derived formulas for systematic and random sampling errors involving integral time scale and measurement period of a given signal. Because here a moving airborne platform is considered, integral length scale L and segment length $\mathcal{L}$ are used instead, invoking Taylor's frozen flow hypothesis.

The errors were determined for turbulent moments (see sec. 3.2.1 and 5.1) and fluxes (see sec. 3.2.2 and 5.2) obtained from LEG measurements. It was found that the standard deviations among subsegments (Std7, see sec. 3.2), which served throughout the current work as an assessment of variability, is of the same order as the random error (L94ran), exceeding it in most of the cases, while the systematic error (L94sys) is usually significantly smaller.

Integral length scales

For each variable x out of (u, θ_v, q_v, T), three integral length scales were estimated according to the procedure described in sec. 3.2.5: L_x corresponding to the autocorrelation of x', L_{wx} corresponding to the correlation of w' and x', L_f corresponding to the autocorrelation of the product $w'x'$. Additionally, the correlation coefficient R_{wx} of w' and x' was calculated. The obtained integral length scales and correlation coefficients are listed in Tables A.1 and A.2 for flights #5 and #14, respectively. In one case, L_{wq_v} could not be determined because the autocorrelation function did not reach sufficiently small value within the available record.

Turbulent moments

The systematic error of a variance was estimated using Eq. (14) of Lenschow et al. (1994):

$$\frac{\Delta_{sys}^{\langle x'^2\rangle}}{\langle x'^2\rangle} = 2\frac{L_x}{\mathcal{L}}. \tag{A.1}$$

The random error of a variance was estimated using their Eq. (36):

$$\frac{\Delta_{ran}^{\langle x'^2\rangle}}{\langle x'^2\rangle} = \sqrt{2\frac{L_x}{\mathcal{L}}}. \tag{A.2}$$

In the case of a third moment, the coefficient a was found by solving their Eq. (20):

$$\frac{\langle x'^3\rangle}{\langle x'^2\rangle^{3/2}} = \frac{2a(3+4a^2)}{(1+2a^2)^{3/2}} \tag{A.3}$$

and then its value was applied in their Eq. (21) to estimate the systematic error:

$$\frac{\Delta_{sys}^{\langle x'^3\rangle}}{|\langle x'^3\rangle|} = 3\left(2 - \frac{1}{(1+a^2)(3+4a^2)}\right)\frac{L_x}{\mathcal{L}}. \tag{A.4}$$

The random error of a third moment was estimated according to Eq. (B40) of Lenschow et al. (1993):

$$\frac{\Delta_{ran}^{\langle x'^3\rangle}}{|\langle x'^3\rangle|} = \sqrt{\frac{(1+a^2)(1+147a^2+1476a^4+780a^6)}{a^2(1+a^2)(3+4a^2)^2}\frac{L_x}{\mathcal{L}}}. \tag{A.5}$$

The sampling errors of turbulent moments are compared with the subsegment variability in Tables A.3 and A.4 for flights #5 and #14, respectively.

Turbulent fluxes

The systematic error of a flux was estimated using Eq. (30) of Lenschow et al. (1994):

$$\frac{\Delta_{sys}^{\langle w'x'\rangle}}{|\langle w'x'\rangle|} = 2\frac{L_{wx}}{\mathcal{L}}\left(1 - \left(1 - e^{-\frac{\mathcal{L}}{L_{wx}}}\right)\left(\frac{L_{wx}}{\mathcal{L}}\right)\right). \tag{A.6}$$

The random error of a flux was estimated using their Eq. (48):

$$\frac{\Delta_{ran}^{\langle w'x'\rangle}}{|\langle w'x'\rangle|} = \sqrt{\frac{2L_f}{\mathcal{L}}\frac{1+R_{wx}^2}{R_{wx}^2}}. \tag{A.7}$$

The sampling errors of turbulent fluxes are compared with the subsegment variability in Tables A.5 and A.6 for flights #5 and #14, respectively.

Table A.1: Integral scales and correlations in flight #5 (coupled STBL).

Height [m]		**307**	**553**	**819**	**1079**	**2018**
Length [km]		5.44	5.51	7.93	3.94	6.25
w'	L_w [m]	146	120	97	112	64
u'	L_u [m]	113	154	179	101	112
	L_{wu} [m]	520	54	31	185	182
	L_f [m]	80	83	39	59	46
	R_{wu} [m]	-0.26	-0.20	-0.11	0.21	-0.31
θ'_v	L_{θ_v} [m]	108	110	172	79	117
	$L_{w\theta_v}$ [m]	353	655	255	25	50
	L_f [m]	48	59	56	37	12
	$R_{w\theta_v}$ [m]	0.30	-0.08	0.46	-0.09	-0.16
q'_v	L_{q_v} [m]	160	136	94	120	318
	L_{wq_v} [m]	157	82	200	NaN	152
	L_f [m]	48	90	43	88	18
	R_{wq_v} [m]	0.56	0.06	0.54	-0.00	0.09
T'	L_T [m]	76	129	204	108	250
	L_{wT} [m]	156	177	238	178	59
	L_f [m]	21	46	51	30	27
	R_{wT} [m]	0.27	0.29	0.55	-0.12	0.14

Table A.2: Integral scales and correlations in flight #14 (decoupled STBL).

Height [m]		**143**	**287**	**448**	**992**	**2021**
Length [km]		8.11	11.92	7.10	4.79	3.49
w'	L_w [m]	53	86	74	35	249
u'	L_u [m]	103	111	109	105	180
	L_{wu} [m]	54	88	63	64	6
	L_f [m]	33	46	29	28	28
	R_{wu} [m]	0.10	-0.18	-0.13	0.14	-0.00
θ'_v	L_{θ_v} [m]	85	50	153	62	115
	$L_{w\theta_v}$ [m]	69	6	596	107	21
	L_f [m]	19	13	71	23	12
	$R_{w\theta_v}$ [m]	0.29	0.03	-0.10	0.28	-0.16
q'_v	L_{q_v} [m]	79	119	117	82	74
	L_{wq_v} [m]	69	89	489	244	160
	L_f [m]	34	60	62	35	25
	R_{wq_v} [m]	0.44	0.42	0.07	0.04	0.11
T'	L_T [m]	52	76	127	49	28
	L_{wT} [m]	33	2	148	130	489
	L_f [m]	29	21	20	23	14
	R_{wT} [m]	0.24	0.01	0.17	0.16	0.28

Table A.3: Statistical errors of the LEG-derived moments in flight #5 (coupled STBL): standard deviation among subsegments (Std7), systematic (L94sys) and random (L94ran) sampling errors.

Height [m]		**307**		**553**		**819**		**1079**		**2018**	
$\langle w'^2 \rangle$	$[\mathrm{m^2\,s^{-2}}, \%]$	0.212		0.104		0.162		0.004		0.006	
	Std7	0.087	41	0.018	17	0.056	35	0.001	23	0.002	29
	L94sys	0.011	5.4	0.005	4.4	0.004	2.4	0.0002	5.7	0.0001	2.0
	L94ran	0.049	23	0.022	21	0.025	16	0.001	24	0.001	14
$\langle w'^3 \rangle$	$[10^{-2}\mathrm{m^3\,s^{-3}}, \%]$	1.69		0.06		0.23		-0.01		-0.02	
	Std7	2.20	130	1.55	2658	2.12	908	0.02	182	0.02	108
	L94sys	0.23	13.4	0.01	10.9	0.01	6.1	0.001	14.3	0.001	5.1
	L94ran	3.38	200	0.99	1699	1.45	619	0.01	130	0.01	74
$\langle u'^2 \rangle$	$[\mathrm{m^2\,s^{-2}}, \%]$	0.34		0.27		0.20		0.37		0.20	
	Std7	0.10	29	0.09	32	0.03	13	0.13	34	0.10	49
	L94sys	0.01	4.2	0.02	5.6	0.01	4.5	0.02	5.1	0.01	3.6
	L94ran	0.07	20	0.06	24	0.04	21	0.08	23	0.04	19
$\langle q_v'^2 \rangle$	$[10^{-3}\mathrm{g^2\,kg^{-2}}, \%]$	5.4		7.8		26.4		1.4		0.0005	
	Std7	1.0	18	1.6	21	17.1	65	1.3	91	0.0001	18
	L94sys	0.3	5.9	0.4	4.9	0.6	2.4	0.1	6.1	0.0001	10.2
	L94ran	1.3	24	1.7	22	4.1	15	0.3	25	0.0001	32
$\langle T'^2 \rangle$	$[10^{-3}\mathrm{K^2}, \%]$	3.3		7.5		18.4		7.3		7.8	
	Std7	0.9	26	3.0	39	8.0	43	6.3	86	3.7	47
	L94sys	0.1	2.8	0.4	4.7	0.9	5.1	0.4	5.5	0.6	8.0
	L94ran	0.6	17	1.6	22	4.2	23	1.7	23	2.2	28

Table A.4: Statistical errors of the LEG-derived moments in flight #14 (decoupled STBL): standard deviation among subsegments (Std7), systematic (L94sys) and random (L94ran) sampling errors.

Height [m]		**143**		**287**		**448**		**992**		**2021**	
$\langle w'^2 \rangle$	[$m^2\,s^{-2}$,%]	0.106		0.076		0.047		0.054		0.004	
	Std7	0.036	34	0.027	36	0.014	30	0.012	22	0.002	35
	L94sys	0.001	1.3	0.001	1.5	0.001	2.1	0.001	1.5	0.001	14.3
	L94ran	0.012	11	0.009	12	0.007	14	0.007	12	0.002	38
$\langle w'^3 \rangle$	[$10^{-2}m^3\,s^{-3}$,%]	0.49		1.34		-0.21		-0.47		-0.01	
	Std7	1.33	272	0.88	66	0.53	247	0.28	59	0.02	287
	L94sys	0.02	3.3	0.05	3.6	0.01	5.2	0.02	3.7	0.002	35.7
	L94ran	0.58	119	0.59	44	0.23	105	0.27	57	0.02	295
$\langle u'^2 \rangle$	[$m^2\,s^{-2}$,%]	0.21		0.14		0.27		0.19		0.05	
	Std7	0.11	53	0.04	25	0.05	18	0.05	27	0.01	32
	L94sys	0.01	2.5	0.003	1.9	0.01	3.1	0.01	4.4	0.005	10.3
	L94ran	0.03	16	0.02	14	0.05	18	0.04	21	0.01	32
$\langle q_v'^2 \rangle$	[$10^{-3}g^2\,kg^{-2}$,%]	27.1		12.0		44.7		31.7		1.2	
	Std7	6.1	23	3.5	30	21.0	47	9.8	31	0.4	32
	L94sys	0.5	1.9	0.2	2.0	1.5	3.3	1.1	3.4	0.1	4.3
	L94ran	3.8	14	1.7	14	8.1	18	5.9	19	0.3	21
$\langle T'^2 \rangle$	[$10^{-3}K^2$,%]	6.7		5.9		11.0		7.7		4.9	
	Std7	0.6	9	1.1	18	3.4	31	3.0	39	0.8	17
	L94sys	0.1	1.3	0.1	1.3	0.4	3.6	0.2	2.0	0.1	1.6
	L94ran	0.8	11	0.7	11	2.1	19	1.1	14	0.6	13

Table A.5: Statistical errors of the LEG-derived fluxes in flight #5 (coupled STBL): standard deviation among subsegments (Std7), systematic (L94sys) and random (L94ran) sampling errors.

	Height [m]	**307**		**553**		**819**		**1079**		**2018**	
B	[10^{-4}m^2 s^{-3} ,%]	1.1		0.1		8.0		-0.1		-0.5	
	Std7	2.7	243	2.8	3055	4.4	55	0.2	170	0.4	84
	L94sys	0.1	12.1	0.02	20.9	0.5	6.2	0.001	1.2	0.01	1.6
	L94ran	0.5	46	0.2	188	2.3	28	0.2	149	0.2	40
S	[10^{-4}m^2 s^{-3} ,%]	2.7		1.6		1.7		0.9		1.0	
	Std7	5.1	272	2.0	235	1.4	110	0.6	68	1.1	124
	L94sys	0.5	17.3	0.03	1.9	0.01	0.8	0.1	8.9	0.1	5.6
	L94ran	1.9	69	1.4	87	1.5	88	0.8	86	0.4	41
Q_s	[W m^{-2} ,%]	4.0		7.2		38.0		-0.6		1.2	
	Std7	2.7	66	6.6	91	20.5	54	0.4	70	0.8	66
	L94sys	0.2	5.6	0.4	6.2	2.2	5.8	0.05	8.6	0.02	1.9
	L94ran	1.3	33	3.3	46	8.9	23	0.6	104	0.8	67
Q_l	[W m^{-2} ,%]	50.4		5.0		104.6		0.1		0.01	
	Std7	22.9	45	22.6	456	77.7	74	1.0	975	0.01	75
	L94sys	2.8	5.6	0.1	2.9	5.1	4.9	NaN	NaN	0.001	4.7
	L94ran	13.7	27	13.9	281	22.9	22	8.3	7869	0.01	81

Table A.6: Statistical errors of the LEG-derived fluxes in flight #14 (decoupled STBL): standard deviation among subsegments (Std7), systematic (L94sys) and random (L94ran) sampling errors.

Height [m]		**143**		**287**		**448**		**992**		**2021**	
B	$[10^{-4}\mathrm{m^2\,s^{-3}},\%]$	2.7		0.3		-0.3		2.6		-0.2	
	Std7	1.5	57	0.5	185	1.7	533	0.9	36	0.2	80
	L94sys	0.05	1.7	0.0003	0.1	0.1	15.4	0.1	4.4	0.002	1.2
	L94ran	0.6	24	0.5	183	0.5	138	0.9	37	0.1	53
S	$[10^{-4}\mathrm{m^2\,s^{-3}},\%]$	0.7		2.3		1.5		1.7		0.1	
	Std7	0.9	137	0.9	67	1.3	87	1.6	125	0.1	175
	L94sys	0.01	1.3	0.03	1.5	0.03	1.8	0.05	2.6	0.001	0.3
	L94ran	0.7	94	1.2	51	1.1	70	1.4	79	4.7	4830
Q_s	$[\mathrm{W\,m^{-2}},\%]$	8.9		1.6		3.6		2.5		0.4	
	Std7	3.3	37	4.1	252	2.7	75	3.8	154	0.6	177
	L94sys	0.1	0.8	0.0004	0.02	0.1	4.1	0.1	5.3	0.1	24.1
	L94ran	3.3	37	14.3	884	1.6	46	1.6	63	0.1	33
Q_l	$[\mathrm{W\,m^{-2}},\%]$	76.7		39.3		6.8		11.5		0.8	
	Std7	36.1	47	28.1	72	43.5	639	23.3	203	0.7	93
	L94sys	1.3	1.7	0.6	1.5	0.9	12.8	1.1	9.7	0.1	8.8
	L94ran	17.5	23	10.1	26	13.4	197	33.8	294	0.8	107

List of acronyms

Ac accumulation mode (of aerosol PNSD)

ACORES Azores stratoCumulus measurements Of Radiation, turbulEnce and aeroSols (field experiment)

ACTOS Airborne Cloud Turbulence Observation System

ARM Atmospheric Radiation Measurement

ARM ENA Atmospheric Radiation Measurement Eastern North Atlantic observatory

ASTEX Atlantic Stratocumulus Transition Experiment (field experiment)

At Aitken mode (of aerosol PNSD)

C_L5 cloud observation code for stratocumulus non-cumulogenitus

C_L8 cloud observation code for stratocumulus and cumulus

CAP-MBL Clouds, Aerosol, and Precipitation in the Marine Boundary Layer (field experiment)

CB cloud base height

CCN cloud condensation nuclei

COARE 3.0 Coupled Ocean-Atmosphere Response Experiment bulk algorithm version 3.0

CPC Condensation Particle Counter

CTEI cloud top entrainment instability

DAAD German Academic Exchange Service

DFG German Research Foundation

DYCOMS-II Second Dynamics and Chemistry of Marine Stratocumulus (field experiment)

ECMWF European Centre for Medium-Range Weather Forecasts

EIL entrainment interface layer

EKT energia kinetyczna turbulencji (TKE in Polish)

ENA Eastern North Atlantic

FT free troposphere

FTL free tropospheric layer

GDAS Global Data Assimilation System

GOES Geostationary Operational Environmental Satellites

HYSPLIT Hybrid Single-Particle Lagrangian Integrated Trajectory

L94ran random sampling error according to Lenschow et al. (1994)

L94sys systematic sampling error according to Lenschow et al. (1994)

LA lager accumulation mode (of aerosol PNSD)

LCL lifting condensation level

LEG horizontal leg (flight segment)

LIM Leipzig Institute for Meteorology, Leipzig University

LWC liquid water content

LWP liquid water path

miniCCNC mini CCN Counter

MODIS Moderate Resolution Imaging Spectroradiometer

NASA National Aeronautics and Space Administration

NCEP National Center for Environmental Prediction

NCN Polish National Science Center

NOAA National Oceanic and Atmospheric Administration

NOAA ARL NOAA Air Resources Laboratory

NOAA OPC NOAA Ocean Prediction Center

OMP Observatório da Montanha do Pico (Mount Pico Mountain Observatory)

OPC Optical Particle Counter

PNSD particle number size distribution

POST Physics of the Stratocumulus Top (field experiment)

PROF vertical profile (flight segment)

PSD power spectral density

PVM-100A Particle Volume Meter, airborne version

RH relative humidity

RMS root mean square

SBL subcloud layer

SCL stratocumulus cloud layer

SEMAPHORE Structure des Echanges Mer-Atmosphere, Proprietes des Heterogeneites Oceaniques: Recherche Experimental (field experiment)

SFC structure function

SMART-HELIOS Spectral Modular Airborne Radiation measurement sysTem HELIcopter-borne Observations of Spectral Radiation

SML surface mixed layer

SMPS Scanning Mobility Particle Sizer

SSA sea spray aerosol

SST sea surface temperature

STBL stratocumulus-topped boundary layer

Std7 standard deviation among the subsegments of a LEG

TKE turbulence kinetic energy

TROPOS Leibniz Institute for Tropospheric Research

TSL transition layer

UFP ultrafine particles

UFT UltraFast Thermometer

UTC Coordinated Universal Time

WGZS warstwa graniczna zwieńczona stratocumulusem (STBL in Polish)

WMO World Meteorological Organization

List of Symbols

Latin

A_ϵ	dissipation anisotropy ratio
$A_\mathcal{P}$	spectral anisotropy ratio
A_{var}	variance anisotropy ratio
B	buoyancy production/consumption of TKE
C^{psd}	power spectrum constant
C^{sfc}	structure function constant
D_p	particle diameter
F_{sol}	solar irradiance
F_{ter}	terrestrial irradiance
L_v	latent heat of vaporization for water
L	integral scale
N_d	cloud droplet number concentration
N_p	aerosol particle number concentration
N_{CCN}	CCN number concentration
Pr	pressure correlation term of the TKE budget equation
P	pressure
Q_l	latent heat flux
Q_s	sensible heat flux
R_d	gas constant for dry air
R_v	gas constant for water vapor
R	Pearson correlation coefficient
S	shear production of TKE
T_v	virtual temperature
Tr	turbulent transport term of the TKE budget equation
T	temperature

U_s	true air speed
U	magnitude of horizontal wind velocity
$\mathcal{D}$	structure function
$\mathcal{L}$	segment length
$\mathcal{P}$	power spectral density
$\mathcal{R}$	autocorrelation function
Nb	Brunt-Vaisala frequency
Ri_g	gradient Richardson number
Sh	shear rate
c_p	specific heat of dry air at constant pressure
dd	direction of horizontal wind velocity
f	frequency
g	gravitational acceleration
h	boundary layer depth
p	power spectrum scaling exponent in the inertial range
q_l	liquid water mass fraction
q_t	total water mass fraction
q_v	specific humidity (water vapor mass fraction)
r_e	cloud droplet effective radius
r_l	liquid water mixing ratio
r_t	total water mixing ratio
r_v	water vapor mixing ratio
r	distance between sampling points
s	structure function scaling exponent in the inertial range
u_e	eastward wind velocity (Earth-fixed coordinate system)
u	longitudinal wind velocity (see sec. 3.2)
v_e	northward wind velocity (Earth-fixed coordinate system)
v	lateral wind velocity (see sec. 3.2)
w_*	convective velocity scale
w_T	droplet settling velocity
w	vertical wind velocity (see sec. 3.2)
x	position along the flight path
z	altitude (above sea level)

Greek

Γ_d	dry adiabatic lapse rate
Γ_m	moist adiabatic lapse rate
Γ	temperature lapse rate
α_θ	decoupling parameter of Wood and Bretherton (2004)
α_q	decoupling parameter of Wood and Bretherton (2004)
β	ceilometer backscatter coefficient
ϵ	TKE dissipation rate
η	Kolmogorov microscale
κ	Randall-Deardorff parameter for CTEI
λ	Taylor microscale
μ	decoupling parameter of Yin and Albrecht (2000)
ν	air kinematic viscosity
ρ	air density
θ_e	equivalent potential temperature
θ_l	liquid water potential temperature
θ_v	virtual potential temperature
θ	potential temperature

Bibliography

Akinlabi, E. O., Wacławczyk, M., Mellado, J. P., and Malinowski, S. P.: Estimating turbulence kinetic energy dissipation rates in the numerically simulated stratocumulus cloud-top mixing layer: Evaluation of different methods, Journal of the Atmospheric Sciences, 76, 1471–1488, doi: 10.1175/JAS-D-18-0146.1, 2019.

Albrecht, B. A., Bretherton, C. S., Johnson, D., Schubert, W. H., and Frisch, A. S.: The Atlantic Stratocumulus Transition Experiment - ASTEX, Bulletin - American Meteorological Society, 76, 889–904, doi: 10.1175/1520-0477(1995)076<0889:TASTE>2.0.CO;2, 1995.

ARM Data Discovery: US Depertment of Energy, Office of Science, Atmopheric Radiation Measurement Program, Data Discovery, url: https://adc.arm.gov/discovery/#/.

Betts, A. K.: Non-precipitating cumulus convection and its parameterization, Quarterly Journal of the Royal Meteorological Society, 99, 178–196, doi: 10.1002/qj.49709941915, 1973.

Bolton, D.: The computation of equivalent potential temperature., Monthly Weather Review, 108, 1046–1053, doi: 10.1175/1520-0493(1980)108<1046:TCOEPT>2.0.CO;2, 1980.

Boucher, O., Randall, D., Artaxo, P., Bretherton, C., Feingold, G., Forster, P., Kerminen, V.-M., Kondo, Y., Liao, H., Lohmann, U., Rasch, P., Satheesh, S., Sherwood, S., Stevens, B., and Zhang, X.-Y.: Clouds and Aerosols, in: Climate Change 2013: The Physical Science Basis. Contribution of Working Group I to the Fifth Assessment Report of the Intergovernmental Panel on Climate Change., edited by Intergovernmental Panel on Climate Change, Cambridge University Press, Cambridge, doi: 10.1017/CBO9781107415324.016, 2013.

Bretherton, C. S. and Pincus, R.: Cloudiness and marine boundary layer dynamics in the ASTEX Lagrangian experiments. Part I: synoptic setting and vertical structure, Journal of the Atmospheric Sciences, 52, 2707–2723, doi: 10.1175/1520-0469(1995)052<2707:CAMBLD>2.0.CO;2, 1995.

Bretherton, C. S. and Wyant, M. C.: Moisture transport, lower-tropospheric stability, and decoupling of cloud-topped boundary layers, Journal of the Atmospheric Sciences, 54, 148–167, doi: 10.1175/1520-0469(1997)054<0148:MTLTSA>2.0.CO;2, 1997.

Bretherton, C. S., Austin, P., and Siems, S. T.: Cloudiness and marine boundary layer dynamics in the ASTEX Lagrangian experiments. Part II: cloudiness, drizzle, surface fluxes, and entrainment, Journal of the Atmospheric Sciences, 52, 2724–2735, doi: 10.1175/1520-0469(1995)052<2724:CAMBLD>2.0.CO;2, 1995.

Caldwell, P., Bretherton, C. S., and Wood, R.: Mixed-layer budget analysis of the diurnal cycle of entrainment in southeast Pacific stratocumulus, Journal of the Atmospheric Sciences, 62, 3775–3791, doi: 10.1175/JAS3561.1, 2005.

Carman, J. K., Rossiter, D. L., Khelif, D., Jonsson, H. H., Faloona, I. C., and Chuang, P. Y.: Observational constraints on entrainment and the entrainment interface layer in stratocumulus, Atmospheric Chemistry and Physics, 12, 11 135–11 152, doi: 10.5194/acp-12-11135-2012, 2012.

China, S., Scarnato, B., Owen, R. C., Zhang, B., Ampadu, M. T., Kumar, S., Dzepina, K., Dziobak, M. P., Fialho, P., Perlinger, J. A., Hueber, J., Helmig, D., Mazzoleni, L. R., and Mazzoleni, C.: Morphology and mixing state of aged soot particles at a remote marine free troposphere site: Implications for optical properties, Geophysical Research Letters, 42, 1243–1250, doi: 10.1002/2014GL062404, 2015.

Cruette, D., Marillier, A., Dufresne, J. L., Grandpeix, J. Y., Nacass, P., and Bellec, H.: Fast temperature and true airspeed measurements with the airborne ultrasonic anemometer-thermometer (AUSAT), Journal of Atmospheric and Oceanic Technology, 17, 1020–1039, doi: 10.1175/1520-0426(2000)017<1020:FTATAM>2.0.CO;2, 2000.

de Lozar, A. and Mellado, J. P.: Evaporative cooling amplification of the entrainment velocity in radiatively driven stratocumulus, Geophysical Research Letters, 42, 7223–7229, doi: 10.1002/2015GL065529, 2015.

de Lozar, A. and Mellado, J. P.: Reduction of the entrainment velocity by cloud droplet sedimentation in stratocumulus, Journal of the Atmospheric Sciences, 74, 751–765, doi: 10.1175/JAS-D-16-0196.1, 2017.

De Roode, S. R. and Duynkerke, P. G.: Observed lagrangian transition of stratocumulus into cumulus during ASTEX: Mean state and turbulence structure, Journal of the Atmospheric Sciences, 54, 2157–2173, doi: 10.1175/1520-0469(1997)054<2157:OLTOSI>2.0.CO;2, 1997.

De Roode, S. R. and Wang, Q.: Do stratocumulus clouds detrain? FIRE I data revisited, Boundary-Layer Meteorology, 122, 479–491, doi: 10.1007/s10546-006-9113-1, 2007.

Deardorff, J. W.: Cloud top entrainment instability., Journal of the Atmospheric Sciences, 37, 131–147, doi: 10.1175/1520-0469(1980)037<0131:CTEI>2.0.CO;2, 1980.

Dodson, D. S. and Small Griswold, J. D.: Turbulent and boundary layer characteristics during VOCALS-REx, Atmospheric Chemistry and Physics, 21, 1937–1961, doi: 10.5194/acp-21-1937-2021, 2021.

Dong, X., Schwantes, A. C., Xi, B., and Wu, P.: Investigation of the marine boundary layer cloud and CCN properties under coupled and decoupled conditions over the Azores, Journal of Geophysical Research: Atmospheres, 120, 6179–6191, doi: 10.1002/2014JD022939, 2015.

Durand, P. and Bourcy, T.: Observations of the turbulence structure within two stratocumulus-topped, marine boundary layers, Boundary-Layer Meteorology, 99, 105–125, doi: 10.1023/A:1018999221303, 2001.

Duynkerke, P. G., Heqing Zhang, and Jonker, P. J.: Microphysical and turbulent structure of nocturnal stratocumulus as observed during ASTEX, Journal of the Atmospheric Sciences, 52, 2763–2777, doi: 10.1175/1520-0469(1995)052<2763:MATSON>2.0.CO;2, 1995.

Dzepina, K., Mazzoleni, C., Fialho, P., China, S., Zhang, B., Owen, R. C., Helmig, D., Hueber, J., Kumar, S., Perlinger, J. A., Kramer, L. J., Dziobak, M. P., Ampadu, M. T., Olsen, S., Wuebbles, D. J., and Mazzoleni, L. R.: Molecular characterization of free tropospheric aerosol collected at the Pico Mountain Observatory: a case study with a long-range transported biomass burning plume, Atmospheric Chemistry and Physics, 15, 5047–5068, doi: 10.5194/acp-15-5047-2015, 2015.

Edson, J. B., Hinton, A. A., Prada, K. E., Hare, J. E., and Fairall, C. W.: Direct covariance flux estimates from mobile platforms at sea, Journal of Atmospheric and Oceanic Technology, 15, 547–562, doi: 10.1175/1520-0426(1998)015<0547:DCFEFM>2.0.CO;2, 1998.

Fairall, C. W., Bradley, E. F., Hare, J. E., Grachev, A. A., and Edson, J. B.: Bulk parameterization of air-sea fluxes: Updates and verification for the COARE algorithm, Journal of Climate, 16, 571–591, doi: 10.1175/1520-0442(2003)016<0571:BPOASF>2.0.CO;2, 2003.

Faloona, I., Lenschow, D. H., Campos, T., Stevens, B., van Zanten, M., Blomquist, B., Thornton, D., Bandy, A., and Gerber, H.: Observations of entrainment in eastern Pacific marine stratocumulus using three conserved scalars, Journal of the Atmospheric Sciences, 62, 3268–3285, doi: 10.1175/JAS3541.1, 2005.

Frehlich, R., Meillier, Y., Jensen, M. L., and Balsley, B.: A statistical description of small-scale turbulence in the low-level nocturnal jet, Journal of the Atmospheric Sciences, 61, 1079–1085, doi: 10.1175/1520-0469(2004)061<1079:ASDOST>2.0.CO;2, 2004.

Gerber, H., Arends, B. G., and Ackerman, A. S.: New microphysics sensor for aircraft use, Atmospheric Research, 31, 235–252, doi: 10.1016/0169-8095(94)90001-9, 1994.

Gerber, H., Frick, G., Malinowski, S. P., Brenguier, J. L., and Burnet, F.: Holes and entrainment in stratocumulus, Journal of the Atmospheric Sciences, 62, 443–459, doi: 10.1175/JAS-3399.1, 2005.

Gerber, H., Frick, G., Malinowski, S. P., Jonsson, H., Khelif, D., and Krueger, S. K.: Entrainment rates and microphysics in POST stratocumulus, Journal of

Geophysical Research: Atmospheres, 118, 12,094–12,109, doi: 10.1002/jgrd.50878, 2013.

Gerber, H., Malinowski, S. P., and Jonsson, H.: Evaporative and Radiative Cooling in POST Stratocumulus, Journal of the Atmospheric Sciences, 73, 3877–3884, doi: 10.1175/JAS-D-16-0023.1, 2016.

Ghate, V. P., Miller, M. A., Albrecht, B. A., and Fairall, C. W.: Thermodynamic and radiative structure of stratocumulus-topped boundary layers, Journal of the Atmospheric Sciences, 72, 430–451, doi: 10.1175/JAS-D-13-0313.1, 2015.

Goren, T., Rosenfeld, D., Sourdeval, O., and Quaas, J.: Satellite Observations of Precipitating Marine Stratocumulus Show Greater Cloud Fraction for Decoupled Clouds in Comparison to Coupled Clouds, Geophysical Research Letters, 45, 5126–5134, doi: 10.1029/2018GL078122, 2018.

Haman, K. E., Makulski, A., Malinowski, S. P., and Busen, R.: A new ultrafast thermometer for airborne measurements in clouds, Journal of Atmospheric and Oceanic Technology, 14, 217–227, doi: 10.1175/1520-0426(1997)014<0217:ANUTFA>2.0.CO;2, 1997.

Haman, K. E., Malinowski, S. P., Kurowski, M. J., Gerber, H., and Brenguier, J.-L.: Small scale mixing processes at the top of a marine stratocumulus—a case study, Quarterly Journal of the Royal Meteorological Society, 133, 213–226, doi: 10.1002/qj.5, 2007.

Hartmann, D. L., Ockert-Bell, M. E., and Michelsen, M. L.: The Effect of Cloud Type on Earth's Energy Balance: Global Analysis, Journal of Climate, 5, 1281–1304, doi: 10.1175/1520-0442(1992)005<1281:teocto>2.0.co;2, 1992.

Henrich, F., Siebert, H., Jäkel, E., Shaw, R. A., and Wendisch, M.: Collocated measurements of boundary layer cloud microphysical and radiative properties: A feasibility study, Journal of Geophysical Research: Atmospheres, 115, doi: 10.1029/2010JD013930, 2010.

Hersbach, H., Bell, B., Berrisford, P., Biavati, G., Horányi, A., Muñoz Sabater, J., Nicolas, J., Peubey, C., Radu, R., Rozum, I., Schepers, D., Simmons, A., Soci, C., Dee, D., and Thépaut, J.-N.: ERA5 hourly data on pressure levels from 1979

to present, Tech. rep., Copernicus Climate Change Service (C3S) Climate Data Store (CDS), doi: 10.24381/cds.adbb2d47, 2018a.

Hersbach, H., Bell, B., Berrisford, P., Biavati, G., Horányi, A., Muñoz Sabater, J., Nicolas, J., Peubey, C., Radu, R., Rozum, I., Schepers, D., Simmons, A., Soci, C., Dee, D., and Thépaut, J.-N.: ERA5 hourly data on single levels from 1979 to present, Tech. rep., Copernicus Climate Change Service (C3S) Climate Data Store (CDS), doi: 10.24381/cds.adbb2d47, 2018b.

Jen-La Plante, I., Ma, Y., Nurowska, K., Gerber, H., Khelif, D., Karpinska, K., Kopec, M. K., Kumala, W., and Malinowski, S. P.: Physics of Stratocumulus Top (POST): Turbulence characteristics, Atmospheric Chemistry and Physics, 16, 9711–9725, doi: 10.5194/acp-16-9711-2016, 2016.

Jones, C. R., Bretherton, C. S., and Leon, D.: Coupled vs. decoupled boundary layers in VOCALS-REx, Atmospheric Chemistry and Physics, 11, 7143–7153, doi: 10.5194/acp-11-7143-2011, 2011.

JPL MUR MEaSUREs: GHRSST Level 4 MUR Global Foundation Sea Surface Temperature Analysis. Ver. 4.1. PO.DAAC, doi: 10.5067/GHGMR-4FJ04, 2015.

Kaimal, J. C., Wyngaard, J. C., and Haugen, D. A.: Deriving Power Spectra from a Three-Component Sonic Anemometer, Journal of Applied Meteorology, 7, 827–837, doi: 10.1175/1520-0450(1968)007<0827:dpsfat>2.0.co;2, 1968.

Katzwinkel, J., Siebert, H., and Shaw, R. A.: Observation of a Self-Limiting, Shear-Induced Turbulent Inversion Layer Above Marine Stratocumulus, Boundary-Layer Meteorology, 145, 131–143, doi: 10.1007/s10546-011-9683-4, url: https://link.springer.com/article/10.1007/s10546-011-9683-4, 2012.

Kazemirad, M. and Miller, M. A.: Summertime post-cold-frontal marine stratocumulus transition processes over the eastern north atlantic, Journal of the Atmospheric Sciences, 77, 2011–2037, doi: 10.1175/JAS-D-19-0167.1, 2020.

Keeler, E., Coulter, R., Kyrouac, J., and Holdridge, D.: Balloon-Borne Sounding System (SONDEWNPN), Tech. rep., Atmospheric Radiation Measurement (ARM) user facility, doi: 10.5439/1021460, 2013.

Kleissl, J., Honrath, R. E., Dziobak, M. P., Tanner, D., Val Martín, M., Owen, R. C., and Helmig, D.: Occurrence of upslope flows at the Pico mountaintop observatory: A case study of orographic flows on a small, volcanic island, Journal of Geophysical Research: Atmospheres, 112, doi: 10.1029/2006JD007565, 2007.

Kolmogorov, A. N.: The local structure of turbulence in incompressible viscous fluid for very large Reynolds numbers, Dokl. Akad. Nauk SSSR, 30, 301–304, doi: 10.1098/rspa.1991.0075, 1941.

Kolmogorov, A. N.: A refinement of previous hypotheses concerning the local structure of turbulence in a viscous incompressible fluid at high Reynolds number, Journal of Fluid Mechanics, 13, 82–85, doi: 10.1017/S0022112062000518, 1962.

Kopec, M. K., Malinowski, S. P., and Piotrowski, Z. P.: Effects of wind shear and radiative cooling on the stratocumulus-topped boundary layer, Quarterly Journal of the Royal Meteorological Society, 142, 3222–3233, doi: 10.1002/qj.2903, 2016.

Kumala, W., Haman, K. E., Kopec, M. K., Khelif, D., and Malinowski, S. P.: Modified ultrafast thermometer UFT-M and temperature measurements during Physics of Stratocumulus Top (POST), Atmospheric Measurement Techniques, 6, 2043–2054, doi: 10.5194/amt-6-2043-2013, 2013.

Kurowski, M., Malinowski, S., and Grabowski, W.: A numerical investigation of entrainment and transport within a stratocumulus-topped boundary layer, Quarterly Journal of the Royal Meteorological Society, 135, 77–92, doi: 10.1002/qj.354, 2009.

Lambert, D. and Durand, P.: The marine atmospheric boundary layer during semaphore. I: Mean vertical structure and non-axisymmetry of turbulence, Quarterly Journal of the Royal Meteorological Society, 125, 495–512, doi: 10.1002/qj.49712555407, 1999.

Lambert, D., Durand, P., Thoumieux, F., Bénech, B., and Druilhet, A.: The marine atmospheric boundary layer during semaphore. II: Turbulence profiles in the mixed layer, Quarterly Journal of the Royal Meteorological Society, 125, 513–528, doi: 10.1002/qj.49712555408, 1999.

Lampert, A., Hartmann, J., Pätzold, F., Lobitz, L., Hecker, P., Kohnert, K., Larmanou, E., Serafimovich, A., and Sachs, T.: Comparison of Lyman-alpha and

LI-COR infrared hygrometers for airborne measurement of turbulent fluctuations of water vapour, Atmospheric Measurement Techniques, 11, 2523–2536, doi: 10.5194/amt-11-2523-2018, 2018.

Lenschow, D. H.: Aircraft Measurements in the Boundary Layer, in: Probing the Atmospheric Boundary Layer, pp. 39–55, American Meteorological Society, doi: 10.1007/978-1-944970-14-7_5, 1986.

Lenschow, D. H. and Stankov, B. B.: Length scales in the convective boundary layer., Journal of the Atmospheric Sciences, 43, 1198–1209, doi: 10.1175/1520-0469(1986)043<1198:LSITCB>2.0.CO;2, 1986.

Lenschow, D. H., Wyngaard, J. C., and Pennell, W. T.: Mean-field and second-moment budgets in a baroclinic, convective boundary layer., Journal of the Atmospheric Sciences, 37, 1313–1326, doi: 10.1175/1520-0469(1980)037<1313:MFASMB>2.0.CO;2, 1980.

Lenschow, D. H., Mann, J., and Kristensen, L.: How Long is Long Enough when Measuring Fluxes and Other Turbulence Statistics?, Tech. rep., University Corporation for Atmospheric Research, 1993.

Lenschow, D. H., Mann, J., and Kristensen, L.: How long is long enough when measuring fluxes and other turbulence statistics?, Journal of Atmospheric and Oceanic Technology, 11, 661–673, doi: 10.1175/1520-0426(1994)011<0661:HLILEW>2.0.CO;2, 1994.

Lenschow, D. H., Zhou, M., Zeng, X., Chen, L., and Xu, X.: Measurements of fine-scale structure at the top of marine stratocumulus, Boundary-Layer Meteorology, 97, 331–357, doi: 10.1023/A:1002780019748, 2000.

Lilly, D. K.: Models of cloud-topped mixed layers under a strong inversion, Quarterly Journal of the Royal Meteorological Society, 94, 292–309, doi: 10.1002/qj.49709440106, 1968.

Mahrt, L.: Stably Stratified Atmospheric Boundary Layers, Annual Review of Fluid Mechanics, 46, 23–45, doi: 10.1146/annurev-fluid-010313-141354, 2014.

Malinowski, S. P., Gerber, H., Jen-La Plante, I., Kopec, M. K., Kumala, W., Nurowska, K., Chuang, P. Y., Khelif, D., and Haman, K. E.: Physics of Stra-

tocumulus Top (POST): Turbulent mixing across capping inversion, Atmospheric Chemistry and Physics, 13, 12 171–12 186, doi: 10.5194/acp-13-12171-2013, 2013.

Markowski, P. and Richardson, Y.: Mesoscale Meteorology in Midlatitudes, John Wiley and Sons, Ltd, Chichester, UK, doi: 10.1002/9780470682104, 2010.

Mather, J. H. and Voyles, J. W.: The arm climate research facility: A review of structure and capabilities, Bulletin of the American Meteorological Society, 94, 377–392, doi: 10.1175/BAMS-D-11-00218.1, 2013.

Mellado, J. P.: Cloud-Top Entrainment in Stratocumulus Clouds, Annual Review of Fluid Mechanics, 49, 145–169, doi: 10.1146/annurev-fluid-010816-060231, 2017.

Mellado, J. P., Bretherton, C. S., Stevens, B., and Wyant, M. C.: DNS and LES for Simulating Stratocumulus: Better Together, Journal of Advances in Modeling Earth Systems, 10, 1421–1438, doi: 10.1029/2018MS001312, 2018.

Moeng, C.-H., Shen, S., and Randall, D. A.: Physical processes within the nocturnal stratus-topped boundary layer, Journal of the Atmospheric Sciences, 49, 2384–2401, doi: 10.1175/1520-0469(1992)049<2384:ppwtns>2.0.co;2, 1992.

Moeng, C. H., Stevens, B., and Sullivan, P. P.: Where is the interface of the stratocumulus-topped PBL?, Journal of the Atmospheric Sciences, 62, 2626–2631, doi: 10.1175/JAS3470.1, 2005.

Morris, V. and Ermold, B.: Ceilometer (CEIL), Tech. rep., Atmospheric Radiation Measurement (ARM) user facility, doi: 10.5439/1181954, 2013.

Muschinski, A., Frehlich, R., Jensen, M., Hugo, R., Hoff, A., Eaton, F., and Balsley, B.: Fine-scale measurements of turbulence in the lower troposphere: An intercomparison between a kit-and balloon-borne, and a helicopter-borne measurement system, Boundary-Layer Meteorology, 98, 219–250, doi: 10.1023/A:1026520618624, 2001.

Muschinski, A., Frehlich, R. G., and Balsley, B. B.: Small-scale and large-scale intermittency in the nocturnal boundary layer and the residual layer, Journal of Fluid Mechanics, 515, 319–351, doi: 10.1017/S0022112004000412, 2004.

Nicholls, S.: The dynamics of stratocumulus: Aircraft observations and comparisons with a mixed layer model, Quarterly Journal of the Royal Meteorological Society, 110, 783–820, doi: 10.1002/qj.49711046603, 1984.

Nicholls, S. and Leighton, J.: An observational study of the structure of stratiform cloud sheets: Part I. Structure, Quarterly Journal of the Royal Meteorological Society, 112, 431–460, doi: 10.1002/qj.49711247209, 1986.

NOAA Ocean Prediction Center: Atlantic Surface Analysis, url: www.opc.ncep.noaa.gov, 2017.

Nowak, J. L., Kumala, W., Kwiatkowski, J., Kwiatkowski, K., Czyzewska, D., Karpinska, K., and Malinowski, S. P.: UltraFast Thermometer 2.0-new temperature sensor for airborne applications and its performance during ACORES 2017, in: Geophysical Research Abstracts, vol. 20, p. 12492, 2018.

Nowak, J. L., Siebert, H., Szodry, K.-E., and Malinowski, S. P.: Coupled and decoupled stratocumulus-topped boundary layers: turbulence properties, Atmospheric Chemistry and Physics Discussions, 2021, 1–41, doi: 10.5194/acp-2021-214, 2021.

Pedersen, J. G., Ma, Y., Grabowski, W. W., and Malinowski, S. P.: Anisotropy of Observed and Simulated Turbulence in Marine Stratocumulus, Journal of Advances in Modeling Earth Systems, 10, 500–515, doi: 10.1002/2017MS001140, 2018.

Pfeifer, S., Birmili, W., Schladitz, A., Müller, T., Nowak, A., and Wiedensohler, A.: A fast and easy-to-implement inversion algorithm for mobility particle size spectrometers considering particle number size distribution information outside of the detection range, Atmospheric Measurement Techniques, 7, 95–105, doi: 10.5194/amt-7-95-2014, 2014.

Pope, S. B.: Turbulent flows, Cambridge University Press, Cambridge, doi: 10.1017/CBO9780511840531, 2000.

Randall, D. A.: Conditional instability of the first kind up-side down., Journal of the Atmospheric Sciences, 37, 125–130, doi: 10.1175/1520-0469(1980)037<0125:CIOTFK>2.0.CO;2, 1980.

Rémillard, J., Kollias, P., Luke, E., and Wood, R.: Marine boundary layer cloud observations in the Azores, Journal of Climate, 25, 7381–7398, doi: 10.1175/JCLI-D-11-00610.1, 2012.

Roberts, G. C. and Nenes, A.: A Continuous-Flow Streamwise Thermal-Gradient CCN Chamber for Atmospheric Measurements, Aerosol Science and Technology, 39, 206–221, doi: 10.1080/027868290913988, 2005.

Schneider, T., Kaul, C. M., and Pressel, K. G.: Possible climate transitions from breakup of stratocumulus decks under greenhouse warming, Nature Geoscience, 12, 164–168, doi: 10.1038/s41561-019-0310-1, 2019.

Schum, S. K., Zhang, B., Dzepina, K., Fialho, P., Mazzoleni, C., and Mazzoleni, L. R.: Molecular and physical characteristics of aerosol at a remote free troposphere site: Implications for atmospheric aging, Atmospheric Chemistry and Physics, 18, 14 017–14 036, doi: 10.5194/acp-18-14017-2018, 2018.

Siebert, H. and Muschinski, A.: Relevance of a tuning-fork effect for temperature measurements with the Gill solent HS ultrasonic anemometer-thermometer, Journal of Atmospheric and Oceanic Technology, 18, 1367–1376, doi: 10.1175/1520-0426(2001)018<1367:ROATFE>2.0.CO;2, 2001.

Siebert, H. and Teichmann, U.: Behaviour of an ultrasonic anemometer under cloudy conditions, Boundary-Layer Meteorology, 94, 165–169, doi: 10.1023/A:1002446723575, 2000.

Siebert, H., Franke, H., Lehmann, K., Maser, R., Saw, E. W., Schell, D., Shaw, R. A., and Wendisch, M.: Probing finescale dynamics and microphysics of clouds with helicopter-borne measurements, Bulletin of the American Meteorological Society, 87, 1727–1738, doi: 10.1175/BAMS-87-12-1727, 2006a.

Siebert, H., Lehmann, K., and Wendisch, M.: Observations of small-scale turbulence and energy dissipation rates in the cloudy boundary layer, Journal of the Atmospheric Sciences, 63, 1451–1466, doi: 10.1175/JAS3687.1, 2006b.

Siebert, H., Shaw, R. A., and Warhaft, Z.: Statistics of small-scale velocity fluctuations and internal intermittency in marine stratocumulus clouds, Journal of the Atmospheric Sciences, 67, 262–273, doi: 10.1175/2009JAS3200.1, 2010.

Siebert, H., Szodry, K.-E., Egerer, U., Wehner, B., Henning, S., Chevalier, K., Lückerath, J., Welz, O., Weinhold, K., Lauermann, F., Gottschalk, M., Ehrlich, A., Wendisch, M., Fialho, P., Roberts, G., Allwayin, N., Schum, S., Shaw, R. A., Mazzoleni, C., Mazzoleni, L., Nowak, J. L., Malinowski, S. P., Karpinska, K., Kumala, W., Czyzewska, D., Luke, E. P., Kollias, P., Wood, R., and Mellado, J. P.: Observations of Aerosol, Cloud, Turbulence, and Radiation Properties at the Top of the Marine Boundary Layer over the Eastern North Atlantic Ocean: The ACORES Campaign, Bulletin of the American Meteorological Society, 102, E123–E147, doi: 10.1175/bams-d-19-0191.1, 2021.

Stein, A. F., Draxler, R. R., Rolph, G. D., Stunder, B. J., Cohen, M. D., and Ngan, F.: Noaa's hysplit atmospheric transport and dispersion modeling system, Bulletin of the American Meteorological Society, 96, 2059–2077, doi: 10.1175/BAMS-D-14-00110.1, 2015.

Stevens, B.: Cloud transitions and decoupling in shear-free stratocumulus-topped boundary layers, Geophysical Research Letters, 27, 2557–2560, doi: 10.1029/1999GL011257, 2000.

Stevens, B.: Entrainment in stratocumulus-topped mixed layers, Quarterly Journal of the Royal Meteorological Society, 128, 2663–2690, doi: 10.1256/qj.01.202, 2002.

Stevens, B., Cotton, W. R., Feingold, G., and Moeng, C. H.: Large-eddy simulations of strongly precipitating, shallow, stratocumulus-topped boundary layers, Journal of the Atmospheric Sciences, 55, 3616–3638, doi: 10.1175/1520-0469(1998)055<3616:LESOSP>2.0.CO;2, 1998.

Stevens, B., Moeng, C. H., Ackerman, A. S., Bretherton, C. S., Chlond, A., de Roode, S., Edwards, J., Golaz, J. C., Jiang, H., Khairoutdinov, M., Kirkpatrick, M. P., Lewellen, D. C., Lock, A., Müller, F., Stevens, D. E., Whelan, E., and Zhu, P.: Evaluation of large-eddy simulations via observations of nocturnal marine stratocumulus, Monthly Weather Review, 133, 1443–1462, doi: 10.1175/MWR2930.1, 2005.

Stull, R. B.: An Introduction to Boundary Layer Meteorology, Springer Netherlands, Dordrecht, doi: 10.1007/978-94-009-3027-8, 1988.

Sutherland, W.: The viscosity of gases and molecular force, The London, Edinburgh, and Dublin Philosophical Magazine and Journal of Science, 36, 507–531, doi: 10.1080/14786449308620508, 1893.

Tjernstrom, M.: Turbulence length scales in stably stratified free shear flow analyzed from slant aircraft profiles, Journal of Applied Meteorology, 32, 948–963, doi: 10.1175/1520-0450(1993)032<0948:TLSISS>2.0.CO;2, 1993.

Tjernström, M. and Rogers, D. P.: Turbulence structure in decoupled marine stratocumulus: A case study from the ASTEX field experiment, Journal of the Atmospheric Sciences, 53, 598–619, doi: 10.1175/1520-0469(1996)053<0598:TSIDMS>2.0.CO;2, 1996.

Turton, J. D. and Nicholls, S.: A Study of the Diurnal Variation of Stratocumulus Using A Multiple Mixed Layer Model, Quarterly Journal of the Royal Meteorological Society, 113, 969–1009, doi: 10.1002/qj.49711347712, 1987.

Vassilicos, J. C.: Dissipation in Turbulent Flows, Annual Review of Fluid Mechanics, 47, 95–114, doi: 10.1146/annurev-fluid-010814-014637, 2015.

Wacławczyk, M., Ma, Y.-F., Kopeć, J. M., and Malinowski, S. P.: Novel approaches to estimating turbulent kinetic energy dissipation rate from low and moderate resolution velocity fluctuation time series, Atmos. Meas. Tech. Discuss., doi: 10.5194/amt-2016-401, 2017.

Wacławczyk, M., Gozingan, A. S., Nzotungishaka, J., Mohammadi, M., and P. Malinowski, S.: Comparison of Different Techniques to Calculate Properties of Atmospheric Turbulence from Low-Resolution Data, Atmosphere, 11, 199, doi: 10.3390/atmos11020199, 2020.

Wang, Q. and Albrecht, B. A.: Observations of Cloud-Top Entrainment in Marine Stratocumulus Clouds, Journal of the Atmospheric Sciences, 51, 1530–1547, doi: 10.1175/1520-0469(1994)051<1530:ooctei>2.0.co;2, 1994.

Wang, Y., Zheng, X., Dong, X., Xi, B., Wu, P., Logan, T., and Yung, Y. L.: Impacts of long-range transport of aerosols on marine-boundary-layer clouds in the eastern North Atlantic, Atmospheric Chemistry and Physics, 20, 14 741–14 755, doi: 10.5194/acp-20-14741-2020, 2020.

Wang, Z., Mora Ramirez, M., Dadashazar, H., MacDonald, A. B., Crosbie, E., Bates, K. H., Coggon, M. M., Craven, J. S., Lynch, P., Campbell, J. R., Azadi Aghdam, M., Woods, R. K., Jonsson, H., Flagan, R. C., Seinfeld, J. H., and Sorooshian, A.: Contrasting cloud composition between coupled and decoupled marine boundary layer clouds, Journal of Geophysical Research: Atmospheres, 121, 11,679–11,691, doi: 10.1002/2016JD025695, 2016.

Wehner, B., Siebert, H., Ansmann, A., Ditas, F., Seifert, P., Stratmann, F., Wiedensohler, A., Apituley, A., Shaw, R. A., Manninen, H. E., and Kulmala, M.: Observations of turbulence-induced new particle formation in the residual layer, Atmospheric Chemistry and Physics, 10, 4319–4330, doi: 10.5194/acp-10-4319-2010, 2010.

Wehner, B., Werner, F., Ditas, F., Shaw, R. A., Kulmala, M., and Siebert, H.: Observations of new particle formation in enhanced UV irradiance zones near cumulus clouds, Atmospheric Chemistry and Physics, 15, 11 701–11 711, doi: 10.5194/acp-15-11701-2015, 2015.

Wendisch, M. and Brenguier, J. L.: Airborne Measurements for Environmental Research, Wiley-VCH Verlag GmbH and Co. KGaA, Weinheim, Germany, doi: 10.1002/9783527653218, 2013.

Wendisch, M., Garrett, T. J., and Strapp, J. W.: Wind tunnel tests of the airborne PVM-100A response to large droplets, Journal of Atmospheric and Oceanic Technology, 19, 1577–1584, doi: 10.1175/1520-0426(2002)019<1577:WTTOTA>2.0.CO;2, 2002.

Werner, F., Siebert, H., Pilewskie, P., Schmeissner, T., Shaw, R. A., and Wendisch, M.: New airborne retrieval approach for trade wind cumulus properties under overlying cirrus, Journal of Geophysical Research: Atmospheres, 118, 3634–3649, doi: 10.1002/jgrd.50334, 2013.

Werner, F., Ditas, F., Siebert, H., Simmel, M., Wehner, B., Pilewskie, P., Schmeissner, T., Shaw, R. A., Hartmann, S., Wex, H., Roberts, G. C., and Wendisch, M.: Twomey effect observed from collocated microphysical and remote sensing measurements over shallow cumulus, Journal of Geophysical Research: Atmospheres, 119, 1534–1545, doi: 10.1002/2013JD020131, 2014.

Williamson, C. J., Kupc, A., Axisa, D., Bilsback, K. R., Bui, T. P., Campuzano-Jost, P., Dollner, M., Froyd, K. D., Hodshire, A. L., Jimenez, J. L., Kodros, J. K., Luo, G., Murphy, D. M., Nault, B. A., Ray, E. A., Weinzierl, B., Wilson, J. C., Yu, F., Yu, P., Pierce, J. R., and Brock, C. A.: A large source of cloud condensation nuclei from new particle formation in the tropics, Nature, 574, 399–403, doi: 10.1038/s41586-019-1638-9, 2019.

Wood, R.: Stratocumulus Clouds, Monthly Weather Review, 140, 2373–2423, doi: 10.1175/MWR-D-11-00121.1, 2012.

Wood, R. and Bretherton, C. S.: Boundary layer depth, entrainment, and decoupling in the cloud-capped subtropical and tropical marine boundary layer, Journal of Climate, 17, 3576–3588, doi: 10.1175/1520-0442(2004)017<3576:BLDEAD>2.0.CO;2, 2004.

Wood, R., Wyant, M., Bretherton, C. S., Rémillard, J., Kollias, P., Fletcher, J., Stemmler, J., De Szoeke, S., Yuter, S., Miller, M., Mechem, D., Tselioudis, G., Chiu, J. C., Mann, J. A., O'Connor, E. J., Hogan, R. J., Dong, X., Miller, M., Ghate, V., Jefferson, A., Min, Q., Minnis, P., Palikonda, R., Albrecht, B., Luke, E., Hannay, C., and Lin, Y.: Clouds, aerosols, and precipitation in the marine boundary layer: An arm mobile facility deployment, Bulletin of the American Meteorological Society, 96, 419–439, doi: 10.1175/BAMS-D-13-00180.1, 2015.

World Meteorological Organization: International Cloud Atlas, url: https://cloudatlas.wmo.int/.

Xiao, H., Wu, C. M., and Mechoso, C. R.: Buoyancy reversal, decoupling and the transition from stratocumulus to shallow cumulus topped marine boundary layers, Climate Dynamics, 37, 971–984, doi: 10.1007/s00382-010-0882-3, 2011.

Xiao, H., Wu, C. M., Mechoso, C. R., and Ma, H. Y.: A treatment for the stratocumulus-to-cumulus transition in GCMs, Climate Dynamics, 39, 3075–3089, doi: 10.1007/s00382-012-1342-z, 2012.

Yamaguchi, T. and Randall, D. A.: Large-eddy simulation of evaporatively driven entrainment in cloud-topped mixed layers, Journal of the Atmospheric Sciences, 65, 1481–1504, doi: 10.1175/2007JAS2438.1, 2008.

Yin, B. and Albrecht, B. A.: Spatial variability of atmospheric boundary layer structure over the eastern equatorial Pacific, Journal of Climate, 13, 1574–1592, doi: 10.1175/1520-0442(2000)013<1574:SVOABL>2.0.CO;2, 2000.

Zheng, G., Wang, Y., Aiken, A. C., Gallo, F., Jensen, M. P., Kollias, P., Kuang, C., Luke, E., Springston, S., Uin, J., Wood, R., and Wang, J.: Marine boundary layer aerosol in the eastern North Atlantic: Seasonal variations and key controlling processes, Atmospheric Chemistry and Physics, 18, 17 615–17 635, doi: 10.5194/acp-18-17615-2018, 2018a.

Zheng, G., Sedlacek, A. J., Aiken, A. C., Feng, Y., Watson, T. B., Raveh-Rubin, S., Uin, J., Lewis, E. R., and Wang, J.: Long-range transported North American wildfire aerosols observed in marine boundary layer of eastern North Atlantic, Environment International, 139, 105 680, doi: 10.1016/j.envint.2020.105680, 2020a.

Zheng, Y. and Li, Z.: Episodes of Warm-Air Advection Causing Cloud-Surface Decoupling During the MARCUS, Journal of Geophysical Research: Atmospheres, 124, 12 227–12 243, doi: 10.1029/2019JD030835, 2019.

Zheng, Y., Rosenfeld, D., and Li, Z.: The Relationships Between Cloud Top Radiative Cooling Rates, Surface Latent Heat Fluxes, and Cloud-Base Heights in Marine Stratocumulus, Journal of Geophysical Research: Atmospheres, 123, 11,678–11,690, doi: 10.1029/2018JD028579, 2018b.

Zheng, Y., Rosenfeld, D., and Li, Z.: Estimating the Decoupling Degree of Subtropical Marine Stratocumulus Decks From Satellite, Geophysical Research Letters, 45, 12,560–12,568, doi: 10.1029/2018GL078382, 2018c.

Zheng, Y., Rosenfeld, D., and Li, Z.: A More General Paradigm for Understanding the Decoupling of Stratocumulus-Topped Boundary Layers: The Importance of Horizontal Temperature Advection, Geophysical Research Letters, 47, doi: 10.1029/2020GL087697, 2020b.